Toughness Based Analysis and Design of Fiber Reinforced Concrete

by

Christopher Barsby

A Thesis Presented in Partial Fulfillment
of the Requirements for the Degree
Master of Science

Approved November 2011 by the
Graduate Supervisory Committee:

Barzin Mobasher, Chair
Narayanan Neithalath
Subramaniam Rajan

ARIZONA STATE UNIVERSITY

December 2011

ABSTRACT

Concrete design has recently seen a shift in focus from prescriptive specifications to performance based specifications with increasing demands for sustainable products. Fiber reinforced composites (FRC) provides unique properties to a material that is very weak under tensile loads. The addition of fibers to a concrete mix provides additional ductility and reduces the propagation of cracks in the concrete structure. It is the fibers that bridge the crack and dissipate the incurred strain energy in the form of a fiber-pullout mechanism. The addition of fibers plays an important role in tunnel lining systems and in reducing shrinkage cracking in high performance concretes. The interest in most design situations is the load where cracking first takes place. Typically the post crack response will exhibit either a load bearing increase as deflection continues, or a load bearing decrease as deflection continues. These behaviors are referred to as strain hardening and strain softening respectively.

A strain softening or hardening response is used to model the behavior of different types of fiber reinforced concrete and simulate the experimental flexural response. Closed form equations for moment-curvature response of rectangular beams under four and three point loading in conjunction with crack localization rules are utilized. As a result, the stress distribution that considers a shifting neutral axis can be simulated which provides a more accurate representation of the residual strength of the fiber cement composites. The use of typical residual strength parameters by standards organizations ASTM, JCI and RILEM are examined to be incorrect in their linear elastic assumption of FRC behavior.

Finite element models were implemented to study the effects and simulate the load defection response of fiber reinforced shotcrete round discrete panels (RDP's) tested in accordance with ASTM C-1550. The back-calculated material properties from the flexural tests were used as a basis for the FEM material models. Further development of FEM beams were also used to provide additional comparisons in residual strengths of early age samples. A correlation between the RDP and flexural beam test was generated based a relationship between normalized toughness with respect to the newly generated crack surfaces.

A set of design equations are proposed using a residual strength correction factor generated by the model and produce the design moment based on specified concrete slab geometry.

….. to my wife Jana and our beloved children William and Stella.

ACKNOWLEDGMENTS

I am pleased to express my deepest gratitude to my advisor and committee chair, Dr. Barzin Mobasher for his co-operation, guidance and constant help throughout my research period. Dr Mobasher provided opportunity and support that transcended traditional committee chair duties, I am humbled by his graciousness and understanding. I would also like to extend my sincere gratitude to my committee members Dr. Subramaniam D. Rajan and Dr Narayanan Neithalath for their timely co-operation, for serving on my committee and for being tremendous resources throughout my time at ASU. I would also like to thank my fellow graduate students, Dr Mehdi Bakhsi, Dr Amir Bonakdar, Geoffrey Minor, Sean Krauss, Eri Vokshi and Jon Fein for their support. I would also like to thank Ben Beard and Richard Hudson from Resolution Copper for their assistance with collation and interpretation of experimental data. Last but not least, this would not have been possible without the constant support, encouragement and love from my wife Jana and our children, William and Stella. Through the late nights, early mornings and constantly changing school schedule you have been my rock through a storm of unknowns.

TABLE OF CONTENTS

CHAPTER Page

APPENDIX

LIST OF TABLES

LIST OF FIGURES

Figure Page

Figure Page

Figure Page

Figure Page

Chapter 1

INTRODUCTION

1.1 Introduction

Resolution Copper Mine (RCM) is in the process of sinking a deep vertical shaft 9 m in diameter, and 2189 m deep at their Resolution project in Superior, AZ. The shaft utilizes a shotcrete lining system as a means of initial shaft support instead of the traditional mesh and bolts. This design change has increased the development speed of the shaft. The shotcrete system must achieve a high early strength and ductility within a short period (less than 24 hours). In order to evaluate the proposed shotcrete system several aspects must be considered, including: the quality control and reliability of the strength, adhesion, and toughness of the newly placed shotcrete materials. Material innovativeness, analysis, design methodology, and the constructability issues are also some of parameters that need to be addressed.

Determining the mechanical properties of the fiber reinforced shotcrete materials as a means of initial support in life critical systems such as shaft lining systems has been an ongoing application of the described material model. It is expected that an appropriate shotcrete mix design and the implementation of true material behaviors in the design procedures can result in significant cost savings in this project. In addition, this analysis procedure provides a quick and reliable method of implementing an ongoing shotcrete quality assurance (QA) program. Test samples can be quickly analyzed to ensure the shotcrete meets the desired specification and adjustments made to the mix as needed.

Design of fiber reinforced shotcrete linings for ground support requires the use of material properties that are obtained from an experimental program. Test results are used to obtain material property data which are incorporated in analytical, empirical, or computer simulation of design cases. The design procedures can also be developed based on models for flexural, tension, and compression behavior. The objective of this set of experiments was to document the different levels of energy absorption and residual load capacity of shotcrete panels tested in accordance to the round panel test ASTM C-1550 and flexural test ASTM C1609. It has been shown that plasticity in the post crack range can influence the load resistance associated with cracking. On presenting experimental data from both flexural and RDP tests, there is a correlation between RDP and flexural energy absorption. Through this relationship we can determine the equivalent absorbed RDP energy from a 4 point flexural test.

The post-cracking tensile strength of FRC is one of the critical safety parameters to insure a safe level of ground support in tunneling applications. The improved toughness and post-cracking strength due to addition of fibers work to especially good advantage in thin-shell applications such as mine and tunnel linings and general ground support [1], especially in areas where traditional boltmesh support techniques are not time efficient. In the application of shaft sinking, a vertical shaft is dug by subsequent blasting of the rock and removal of debris. Safety requirements dictate that the personnel working below the recently blasted rock be secured for potential falling rocks while preparation for the permanent casing and also next incremental explosions are talking place. Use of shotcrete in these instances is of primary importance for rock surface stabilization. Shotcrete is sprayed directly onto the excavated shaft while the ground is still deforming soon after excavation as an initial lining or on top of previously placed shotcrete as a permanent lining [2]. Shotcrete materials produced with short, randomly distributed fibers may be superior to other forms of reinforcement using welded wire mesh, or rebar since the small diameter of the individual fibers ensures a better and more uniform dispersion, along with far superior bond ductility. Figure 1.1.1 shows the application of fiber reinforced shotcrete for the deep shaft stabilization in the copper mine in Superior, Arizona.

Figure 1.1.1 – Shotcrete for Deep Shaft Stabilization – Resolution Copper Mine, Superior, AZ

The potential to lower the placement cost of shotcrete by eliminating wire mesh is the key to increasing application of fibrous shotcrete.

Shotcrete distributes force in the excavated ground and provides stability as the excavation advances. Therefore, early age strength development is a major consideration for design and construction processes. The effect of synthetic fibers on the development of high early strength and toughness for shotcrete applications is studied. An experimental and analytical program is performed to evaluate effects of age on flexural load-deflection and back calculated tensile stress strain responses. Standards test methods such as ASTM C 1609 [3], RILEM TC 162-TDF [4], and JCI-SF4 [5] propose calculation of residual strength based on bending tests using simple engineering bending theory for linear elastic materials and gross un-cracked section properties. However, in this study tensile stress-strain response is used as the basis for toughness calculation. Tensile properties are predicted by means of an inverse analysis procedure that addresses the cracking in the composite and using moment-curvature relationships and crack localization rules; the load deflection response is obtained. A strain softening response is used to model the behavior of different types of fiber reinforced concrete and simulate the experimental flexural response. Finally, the back-calculated post-cracking strengths are compared and correlated with the corresponding standard method parameters.

1.2 Review of Related Literature

Fiber reinforced concrete (FRC) is widely used in time critical applications such as tunnel lining and shotcrete because of its improved mechanical properties such as fracture toughness, ductility and crack-width control [6, 7]. As a primary area of application [8, 9], steel and synthetic fibers have been used over 40 years in order to reduce shrinkage and thermal cracking, reduce the required slab thickness, and increase the allowable joint spacing [10, 11, 12]. Use of fibers offers early age ductility, resisting potential early age cracking in addition to maintaining long term strength due to the composite action [13]. Moreover, due to the reduced specific spacing, fibers strengthen the composite at the micro level by bridging the micro-cracks before they reach the critical flaw size [14]. On the other hand, due to very high specific surface area, reduced labor costs, reduced potential for mistakes at the jobsite, and efficiency and time saving in placement and compaction, fibers are economically comparable to the steel mesh reinforcement and provide excellent strengthening mechanisms.

Current structural applications of FRC where strength and toughness are important to the design include but not limited to precast structural elements [15], tunnel linings [16, 17] shotcrete [18, 19, 20, 21, 22], offshore structures, structures in seismic regions, thin and thick repairs, crash barriers, footings, and hydraulic structures [13, 23]. The fibers are also added to concrete to enhance spalling resistance during exposure to high temperature [24]. The mechanical properties of FRC depend on the characteristics of the concrete matrix but also on the type and geometry of the fibers, governing the bond mechanism between them and the concrete [25, 26]. Although fibers offer increased abrasion and impact resistance [27], among all mechanical parameters, residual tensile strength and toughness are the most improved parameters due to the fiber bridging mechanisms across the crack surfaces [28, 29].

1.3 Objectives of the Thesis

The main aim of the thesis is to characterize the early age residual strength of fiber reinforced shotcrete (FRS) being used for shaft wall containment. By offering a means of comparison of FRS residual strength, quality control measures can be established. This is done through the use of flexural beams tests, round determinant panel tests and finite element models. As a result, it is suspected that current standards (ASTM, JCI and RILEM) provide inadequate methods of characterizing residual strength. This may be attributed to fact that these data reduction approaches fail to recognize the shifting neutral axis once a specimen cracks and thereby overestimating the residual tensile strength of an FRC sample. The primary goal of this thesis is to evaluate a rational approach to use the flexural and round panel tests for evaluation, quality control, analysis and also design of fiber reinforced concrete. The following topics are addressed in detail and correlated through the use of finite element method and structural mechanics tools.

1. Flexural Tests

Flexural tests represent a straight forward standardized way to determine primary material properties and tensile properties. Three point (ASTM C-1399) [2]and four point (ASTM C-1609) [3] are used in the field as a means of a repeatable quality assurance and control measure. Beam load deflection data (ASTM C-1609) were sent to ASU for modeling and analysis. A tri-linear material model was adapted using Microsoft Excel as the primary modeling tool. This produced experimental analysis and back-calculated material properties.

2. Round Determinate Panel Tests

Round determinate panel (RDP) tests were developed by Bernard (2001) [35] as a way of more accurately modeling planar fiber reinforced sections, by minimizing unevenness in the tensile surface. Samples were cast in the field at the Superior RCM facility by directly spraying fiber reinforced shotcrete into circular molds and tested according to ASTM C-1550 [5] at the Superior facility. RDP load deflection data was sent to ASU for modeling and analysis. A finite element model was adapted to simulate the experimental load deflection response and produce back-calculated FRS material properties.

3. Test Correlations

In generating toughness data for both ASTM C-1609 and ASTM C-1550 a residual strength correlation can be drawn between the two tests. Once a correlation is established, there will be no need for extensive RDP testing and a simple flexural test can be used to simulate the absorbed energy of an RDP. This correlation will be done by normalizing the flexural toughness as a basis for comparison.

Chapter 2

STRAIN SOFTENING AND HARDENING MODELS FOR FIBER REINFORCED CONCRETE

2.1 Material Model

A formulation is presented to use a recently developed modeling technique for back-calculation of material properties from experimental data [30]. The experimental data have been fitted using closed form relationships of the load deflection results of a nonlinear fiber reinforced concrete material [31, 32]. The adaptation of this method, using a tri-linear model provides a more precise prediction of the flexural response to back-calculate material parameters. This approach can also be extended to explain the different features between the tensile and flexural strength and ductility of strain softening and hardening FRC materials [33, 34].

In order to correlate tensile and flexural data for various materials, an approach is presented for closed-form solution of moment-curvature response and load deflection calculation of homogenized materials. Fig. 2.1.1 presents the constitutive model for homogenized strain softening reinforced concrete. The linear portion of an elastic-perfectly-plastic compressive stress-strain response terminates at yield point (ε_{cy}, σ_{cy}) and remains constant at compressive yield stress σ_{cy} until the ultimate compressive strain ε_{cu} as shown in Fig. 2.1.1a.

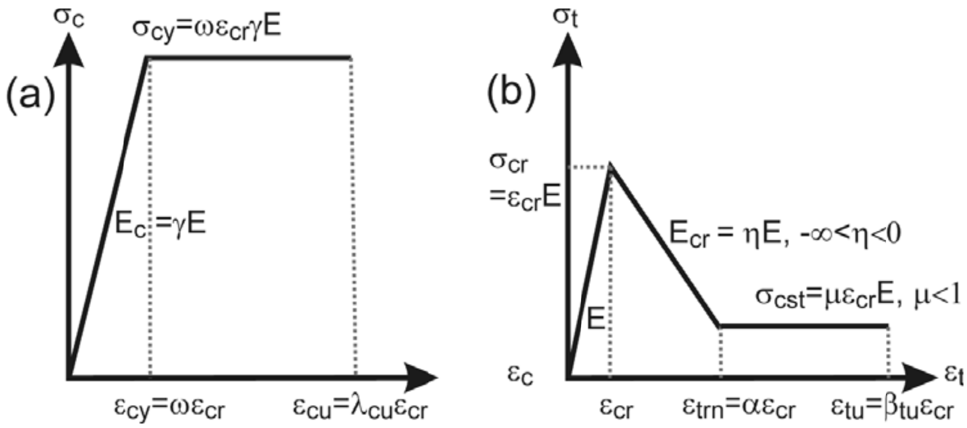

Figure 2.1.1. Strain softening material model for FRC materials: (a) compression, (b) tension.

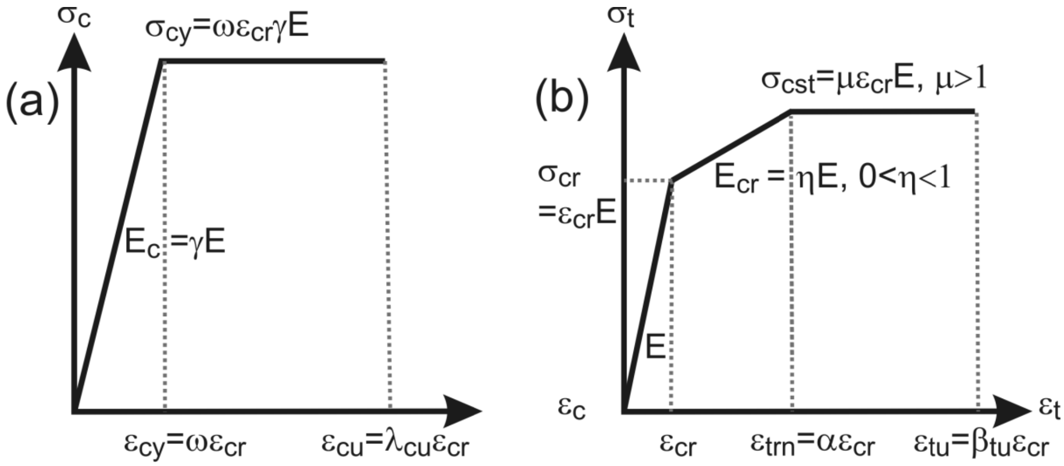

Figure 2.1.2 – Strain hardening model for FRC materials: (a) compression, (b) tension

The tension model in Fig. 2.1.1b is described by a tri-linear response with an elastic range E, and post cracking modulus E_{cr} which is assigned a negative or positive value in order to simulate both strain softening and hardening materials. The third region in the tensile response is a constant stress range defined with stress σ_{cst} in the post crack region. Two strain measures define the first cracking and transition strains (ε_{cr}, ε_{trn}). The tensile response terminates at the ultimate tensile strain level of ε_{tu}. Two intrinsic material parameters are defined: first cracking tensile strain ε_{cr} and tensile modulus E . Using these two parameters seven normalized parameters with respect to E and ε_{cr} as shown in Eqs. (2.1).

$$\omega=\frac{\varepsilon_{cy}}{\varepsilon_{cr}};\quad \alpha=\frac{\varepsilon_{trn}}{\varepsilon_{cr}};\quad \beta_{tu}=\frac{\varepsilon_{tu}}{\varepsilon_{cr}};\quad \lambda_{cu}=\frac{\varepsilon_{cu}}{\varepsilon_{cr}};\quad \gamma=\frac{E_c}{E};\quad \eta=\frac{E_{cr}}{E};\quad \mu=\frac{\sigma_{cst}}{E\varepsilon_{cr}} \tag{2.1}$$

In a flexural test the derivation of moment-curvature relationship for a rectangular cross section with a width "b" and depth "d", the Kirchhoff hypothesis is applied and the maximum tensile strain β and maximum compressive strain λ are linearly related through the normalized neutral axis parameter, k. as in Eqs. (2.2)

$$\beta=\frac{\varepsilon_{tbot}}{\varepsilon_{cr}};\quad \lambda=\frac{\varepsilon_{ctop}}{\varepsilon_{cr}};\quad \frac{\lambda\varepsilon_{cr}}{kd}=\frac{\beta\varepsilon_{cr}}{d-kd}\quad \text{or}\quad \lambda=\frac{k}{1-k}\beta \tag{2.2}$$

Using the normalized parameters defined in Eqs. (2.1) and (2.2), normalized stress strain responses and toughness G_f are expressed as:

$$\frac{\sigma_c(\lambda)}{E\varepsilon_{cr}}=\begin{cases}\gamma\lambda & 0\le\lambda\le\omega\\ \gamma\omega & \omega<\lambda\le\lambda_{cu}\\ 0 & \lambda_{cu}<\lambda\end{cases}\qquad \frac{\sigma_t(\beta)}{E\varepsilon_{cr}}=\begin{cases}\beta & 0\le\beta\le1\\ 1+\eta(\beta-1) & 1<\beta\le\alpha\\ \mu & \alpha<\beta\le\beta_{tu}\\ 0 & \beta_{tu}\le\beta\end{cases} \tag{2.3}$$

$$G_f=E\varepsilon_{cr}^2\left[\left(\frac{\alpha-\mu-\mu\alpha}{2}\right)+\mu\beta_{tu}\right] \tag{2.4}$$

By assuming linear strain distribution across the depth and ignoring shear deformations, stress distribution across the cross section at three stages of imposed tensile strain: $0 \le \beta \le 1$, $1 < \beta \le \alpha$ and $\alpha < \beta \le \beta_{tu}$ is obtained in closed form [33]. Internal moment is obtained using the force components and their distance from the neutral axis and the curvature is determined as the ratio of compressive strain at top fiber ($\varepsilon_{ctop}=\lambda\varepsilon_{cr}$) to the depth of neutral axis *kd*. The moment M_i and curvature ϕ_i at each stage *i* (which corresponds to an input tensile fiber strain, β) are then normalized with respect to the values at cracking M_{cr} and ϕ_{cr} and are presented in equations (2.5) and (2.6). The transition from deflection softening to deflection hardening is defined by critical normalized post-peak tensile strength (μ_{crit}) as defined in Eq. (2.7).

$$M_i = M' M_{cr}; \quad M_{cr} = \frac{1}{6} b d^2 E \varepsilon_{cr} \tag{2.5}$$

$$\phi_i = \phi_i' \phi_{cr}; \quad \phi_{cr} = \frac{2\varepsilon_{cr}}{d} \tag{2.6}$$

$$\mu_{crit} = \frac{\omega}{3\omega - 1} \tag{2.7}$$

The calculation of *k*, *M'* and ϕ' for the five stages of governing strain is presented in Table 2.1.1 During stage 1 the tensile and compressive zones are both elastic and are represented as a straight line on a moment-curvature plot (stiffness $K = \frac{1}{12} b d^3 E$). During this stage the neutral axis remains at the centroid of the test sample. This case continues until the point of first cracking. As the elastic Stage 1 ends by the initiation of tensile cracking, the neutral axis moves toward the compression zone which remains elastic during early stages. As the straining continues, the compression side may or may not enter the plastic zone, resulting in two possible outcomes. As long as the compression zone is elastic zone we define the behavior as Stage 2.1 (tension cracking-elastic compression). If the compression side enters the plastic range, Stage 2.2 (cracking tension-plastic compression) is defined. However if the tension response dominates and the condition in Stage 2.1 ends under two potential alternatives of entering from the tensile softening into either region 2.2, or region 3.1 depending on the compression zone remaining in the elastic range or not. If the compression zone is already in the elastic range we define as Stage 3.1, however if the compression zone has already entered the plastic range (2.2) then the next step would be tension softening-plastic compression or Stage 3.2. It is important to note that depending on the relationship among material parameters, any of the stages 2.1, and 2.2, or 3.1, and 3.2 are potentially possible in succession.

Stage	Parameters	k	M' = M/M$_{cr}$	$\phi' = \phi/\phi_{cr}$
1	$0 < \beta \leq 1$	$k_1 = \begin{cases} \dfrac{1}{2} & \text{for } \gamma = 1 \\ \dfrac{-1+\sqrt{\gamma}}{-1+\gamma} & \text{for } \gamma \neq 1 \end{cases}$	$M'_1 = \dfrac{2\beta\left[(\gamma-1)k_1^3 + 3k_1^2 - 3k_1 + 1\right]}{1-k_1}$	$\phi'_1 = \dfrac{\beta}{2(1-k_1)}$
2.1	$1 < \beta \leq \alpha$ $0 < \lambda \leq \omega$	$k_{21} = \dfrac{D_{21} - \sqrt{D_{21}\gamma\beta^2}}{D_{21} - \gamma\beta^2}$ $D_{21} = \eta\left(\beta^2 - 2\beta + 1\right) + 2\beta - 1$	$M'_{21} = \dfrac{\left(2\gamma\beta^3 - C_{21}\right)k_{21}^3 + 3C_{21}k_{21}^2 - 3C_{21}k_{21} + C_{21}}{1-k_{21}}$ $C_{21} = \dfrac{(2\beta^3 - 3\beta^2 + 1)\eta + 3\beta^2 - 1}{\beta^2}$	$\phi'_{21} = \dfrac{\beta}{2(1-k_{21})}$
2.2	$1 < \beta \leq \alpha$ $\omega < \lambda \leq \lambda_{cu}$	$k_{22} = \dfrac{D_{22}}{D_{22} + 2\omega\gamma\beta}$, $D_{22} = D_{21} + \gamma\omega^2$	$M'_{22} = \left(3\gamma\omega\beta^2 + C_{22}\right)k_{22}^2 - 2C_{22}k_{22} + C_{22}$, $C_{22} = C_{21} - \dfrac{\gamma\omega^3}{\beta^2}$	$\phi'_{22} = \dfrac{\beta}{2(1-k_{22})}$
3.1	$\alpha < \beta \leq \beta_{tu}$ $0 < \lambda \leq \omega$	$k_{31} = \dfrac{D_{31} - \sqrt{D_{31}\gamma\beta^2}}{D_{31} - \gamma\beta^2}$ $D_{31} = \eta\left(\alpha^2 - 2\alpha + 1\right) + 2\mu(\beta - \alpha) + 2\alpha - 1$	$M'_{31} = \dfrac{\left(2\gamma\beta^3 - C_{31}\right)k_{31}^3 + 3C_{31}k_{31}^2 - 3C_{31}k_{31} + C_{31}}{1-k_{31}}$ $C_{31} = \dfrac{(2\alpha^3 - 3\alpha^2 + 1)\eta - 3\mu\left(\alpha^2 - \beta^2\right) + 3\alpha^2 - 1}{\beta^2}$	$\phi'_{31} = \dfrac{\beta}{2(1-k_{31})}$
3.2	$\alpha < \beta \leq \beta_{tu}$ $\omega < \lambda \leq \lambda_{cu}$	$k_{32} = \dfrac{D_{32}}{D_{32} + 2\omega\gamma\beta}$, $D_{32} = D_{31} + \gamma\omega^2$	$M'_{32} = \left(3\gamma\omega\beta^2 + C_{32}\right)k_{32}^2 - 2C_{32}k_{32} + C_{32}$, $C_{32} = C_{31} - \dfrac{\gamma\omega^3}{\beta^2}$	$\phi'_{32} = \dfrac{\beta}{2(1-k_{32})}$

Table 2.1.1 Governing equations for the calculation of k, M' and φ' for each stage specified by strains at top and bottom fibers.

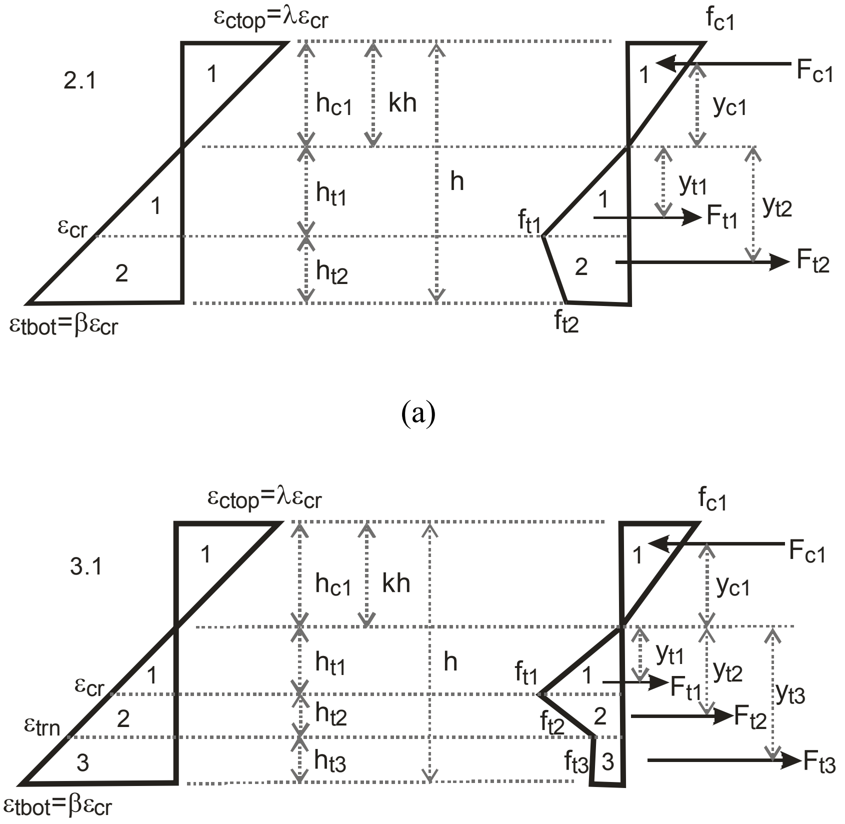

(a)

(b)

Figure 2.1.2 – Strain and stress diagrams at the post crack stage (Stages 2.1 and 3.1, Table 2.1.1), (a) strain and stress stage 2.1; and (b) strain and stress stage 3.1.

By applying the moment-area method to the bilinear moment curvature diagram, mid-span deflection of three-point bending tests can be derived explicitly [30]. After cracking, the curvature distribution depends on the normalized post-peak tensile strain. The maximum deflection during the elastic stage of loading is determined from the curvature at cracking (ϕ_{cr}) and Eq. (2.8). If $\mu > \mu_{crit}$, as the post-crack curvature increases, the moment continues to increase with the deflection determined by Eq. (2.9). On the other hand, if $\mu<\mu_{\mathrm{crit}}$, as the post-crack curvature increases, the moment either increases or decreases at the levels below the bilinear cracking moment M_{cr}, the deflection during this stage is determined by Eq. (2.10). The term L_p used in Eq. (2.10) represents the length of localization zone.

$$\delta_{cr}=\frac{1}{12}L^2\phi_{cr} \tag{2.8}$$

$$\delta_u=\frac{L^2}{24M_u^2}\left[\left(2M_u^2-M_uM_{cr}-M_{cr}^2\right)\phi_u+\left(M_u^2+M_uM_{cr}\right)\phi_{cr}\right] \tag{2.9}$$

$$\delta_u=\frac{\phi_uL_p}{8}\left(2L-L_p\right)+\frac{M_u\phi_{cr}L}{12M_{cr}}\left(L-2L_p\right) \tag{2.10}$$

The same set of equations can be expressed for mid-point deflection for four-point bending tests. The maximum deflection during the elastic stage of loading is determined from Eq. (2.11). If $\mu>\mu_{\mathrm{crit}}$, the deflection determined by Eq. (2.12) and if $\mu<\mu_{\mathrm{crit}}$, as the post-crack curvature increases, the moment either increases or decreases at the levels below the bilinear cracking moment M_{cr}, the deflection during this stage is determined by Eq. (2.13).

$$\delta_{cr}=\frac{23}{216}L^2\varphi_{cr} \tag{2.11}$$

$$\delta_u=\frac{L^2}{216M_u^2}\left[\left(23M_u^2-4M_uM_{cr}-4M_{cr}^2\right)\varphi_u+\left(4M_u^2+4M_uM_{cr}\right)\varphi_{cr}\right] \tag{2.12}$$

$$\delta_u=\frac{5L^2\varphi_u}{72}+\frac{M_uL^2\varphi_{cr}}{27M_{cr}} \tag{2.13}$$

From the approximate bilinear moment-curvature diagram, the total load P_i at a given stage of loading i can be calculated by Eq. (2.14) for ϕ_1 through ϕ_u, where $S = L/2$ for three point bending and tests, respectively.

$$P_i = \frac{2M_i}{S} \tag{2.14}$$

When a flexural specimen is loaded beyond the peak strength, the load decreases and two distinct zones develop as the deformation localizes in the cracking region while the remainder of the specimen undergoes general unloading. To correlate the stress-crack width relationship into the stress–strain approach, localization of major cracks is simulated as an average response over the strain softening region L_p [35]. The load deformation behavior is obtained using the smeared crack in conjunction with the moment–curvature response as presented by Soranakom and Mobasher [33].

2.2 Model Implementation

The implementation of the tri-linear strain hardening and softening model in a format that was user friendly and intuitive was key to its development. Using Microsoft Excel as the platform opens the field to who can drive the software and perform the analysis. The spreadsheet is driven by a handful of user defined inputs to fit a simulated load deflection curve to an experimental one. The user inputs are material properties and model parameters, with experimental and back-calculation going on in the background. A laboratory technician or graduate student can run a flexural beam test (4 or 3 point), collect load deflection data, input it into the spreadsheet, perform a curve fit and copy the results to a final document for further analysis. Curve fitting is done in real time. As material inputs are changed, the simulated curve immediately updates, providing a fast and reliable way of data reduction. Figure 2.2.1 shows the user inputs to the back-calculation spreadsheet, including type of test, beam dimensions, material properties (E and εcr) and compressive and tensile model parameters (ω, λcu and α, γ, η, μ, βtu). These parameters are normalized with respect to εcr so units must be consistent as noted (in, lbs, psi or mm, N, MPa). Figure 2.2.2 show the experimental and simulated load deflection curves that are produced in real time as the parameters are manipulated to fit the simulation. A copy of this program is available from the Computational and Experimental Mechanics Laboratory at ASU. For a copy contact the author or Dr. Barzin Mobasher [57]

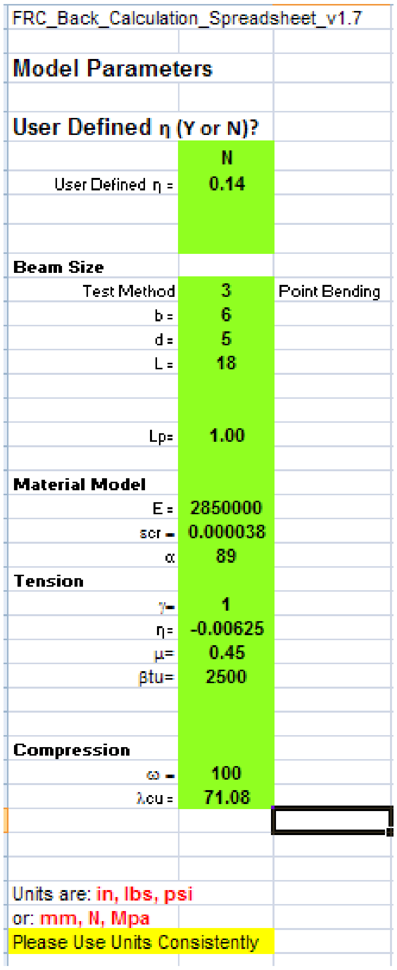

FRC_Back_Calculation_Spreadsheet_v1.7		
Model Parameters		
User Defined η (Y or N)?		
	N	
User Defined η =	0.14	
Beam Size		
Test Method	3	Point Bending
b =	6	
d =	5	
L =	18	
Lp=	1.00	
Material Model		
E =	2850000	
scr =	0.000038	
α	89	
Tension		
γ=	1	
η =	-0.00625	
μ=	0.45	
βtu=	2500	
Compression		
ω =	100	
λcu =	71.08	
Units are: in, lbs, psi		
or: mm, N, Mpa		
Please Use Units Consistently		

Figure 2.2.1. User inputs to back-calculation spreadsheet

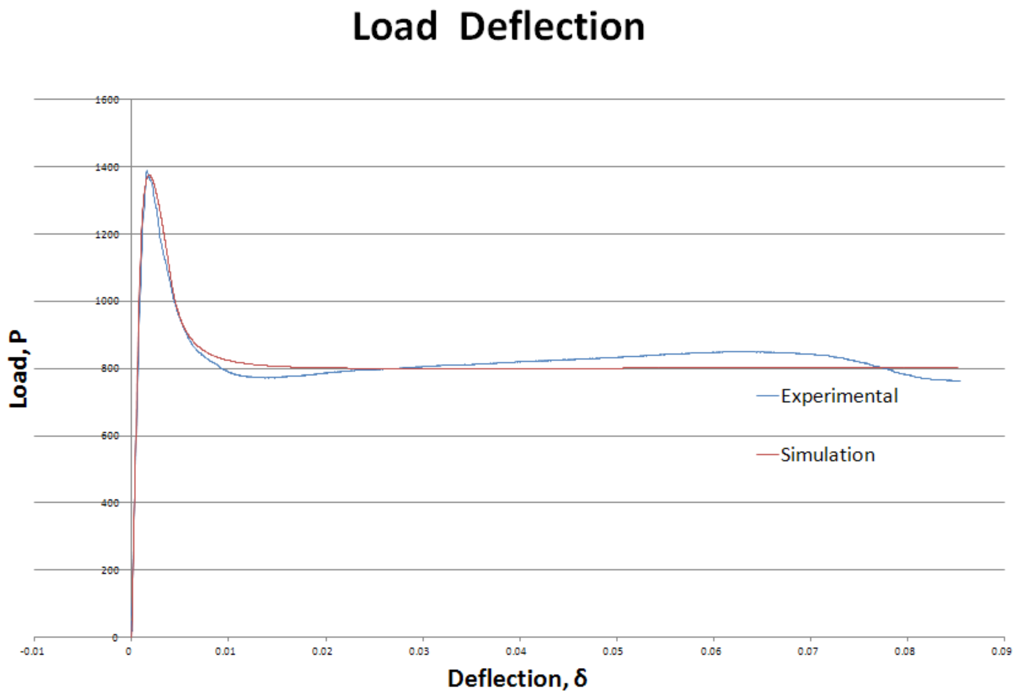

Figure 2.2.2. Experimental and simulated load deflection curves

The results are posted to a tab which contains the experimental and back-calculation data necessary for reporting or additional analysis. Figure 2.2.3 show the type of data included. While the spreadsheet does calculations using constant units, the reporting tab generates units based on the dimensions used for span length, L (L>150 use SI) as typical beam samples rarely exceed 150 inches.

The model was implemented based on an incrementally imposed tensile strain (β), with the ultimate tensile strain being represented by βtu. Parametric studies show the effect of each of the tensile parameters (α, η and μ), as FRC rarely fails in compression during flexural tests, which serve as a starting point when fitting unfamiliar curves.

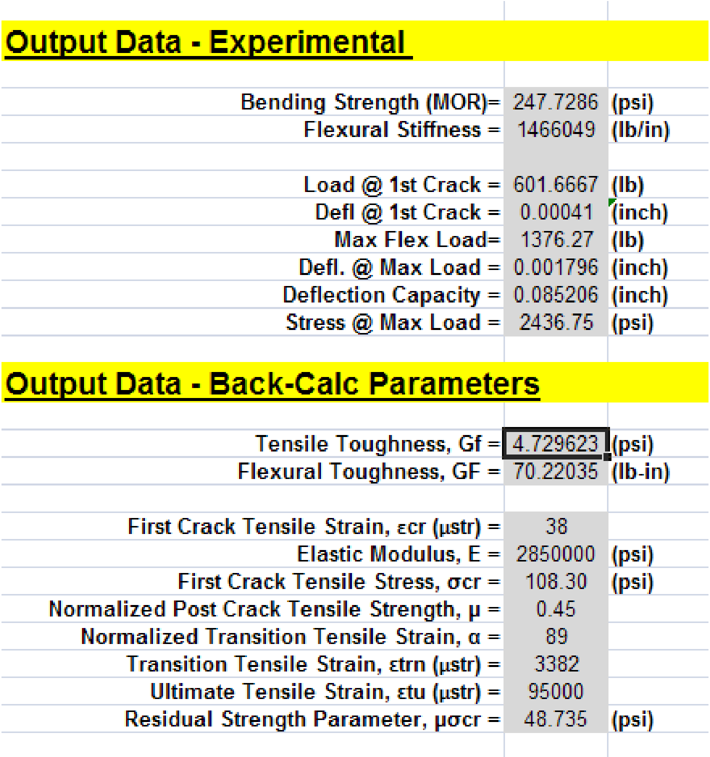

Output Data - Experimental

Bending Strength (MOR)=	247.7286	(psi)
Flexural Stiffness =	1466049	(lb/in)
Load @ 1st Crack =	601.6667	(lb)
Defl @ 1st Crack =	0.00041	(inch)
Max Flex Load=	1376.27	(lb)
Defl. @ Max Load =	0.001796	(inch)
Deflection Capacity =	0.085206	(inch)
Stress @ Max Load =	2436.75	(psi)

Output Data - Back-Calc Parameters

Tensile Toughness, Gf =	4.729623	(psi)
Flexural Toughness, GF =	70.22035	(lb-in)
First Crack Tensile Strain, εcr (μstr) =	38	
Elastic Modulus, E =	2850000	(psi)
First Crack Tensile Stress, σcr =	108.30	(psi)
Normalized Post Crack Tensile Strength, μ =	0.45	
Normalized Transition Tensile Strain, α =	89	
Transition Tensile Strain, εtrn (μstr) =	3382	
Ultimate Tensile Strain, εtu (μstr) =	95000	
Residual Strength Parameter, μσcr =	48.735	(psi)

Figure 2.2.3. Output tab results showing experimental and back-calculation parameters

Figures 2.2.4, 2.2.5 and 2.2.6 show the effect of these tensile parameters for a strain softening response, while figures 2.2.7, 2.2.8 and 2.2.9 show the parameters for a strain hardening response. A step by step user guide for the back-calculation spreadsheet is shown in Appendix A. This spreadsheet was used to provide all of the experimental and back-calculation analysis for all of the flexural tests.

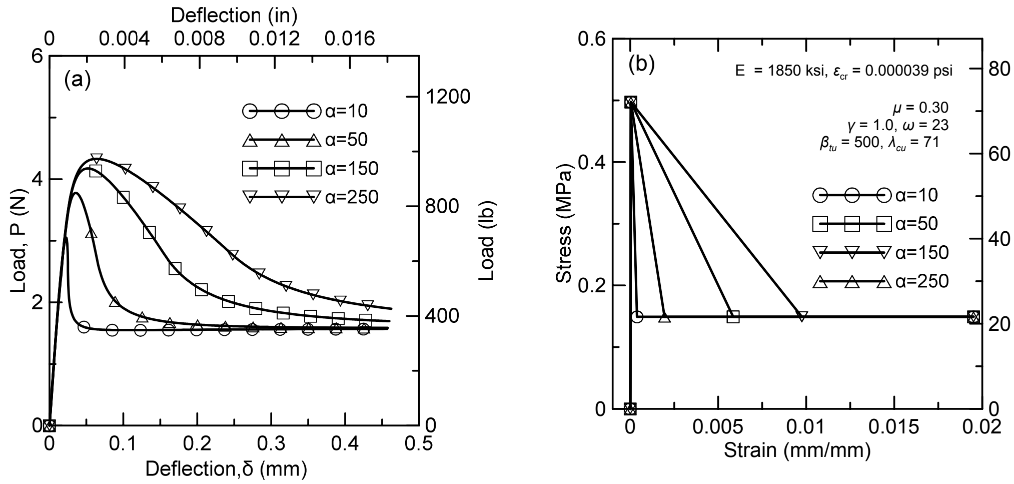

Figure 2.2.4. Parametric study of parameter alpha (α) with (a) load deflection response and (b) stress strain simulations (softening).

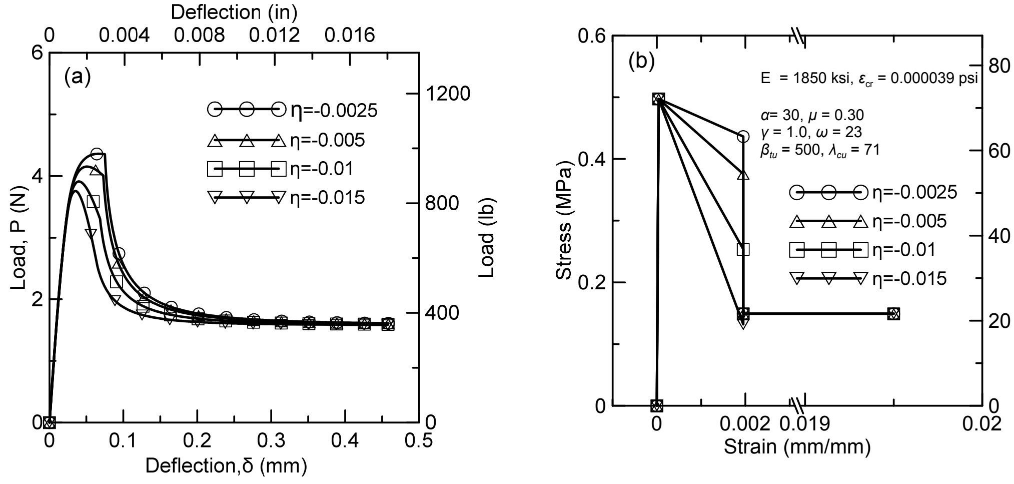

Figure 2.2.5. Parametric study of parameter eta (η) with (a) load deflection and (b) stress strain simulations (softening).

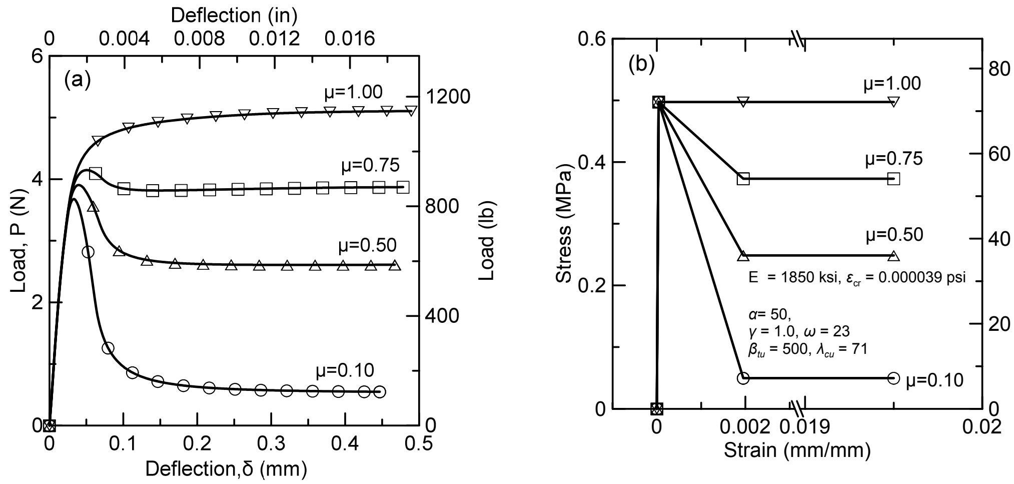

Figure 2.2.6. Parametric study of parameter mu (μ) with (a) load deflection and (b) stress strain simulations (softening).

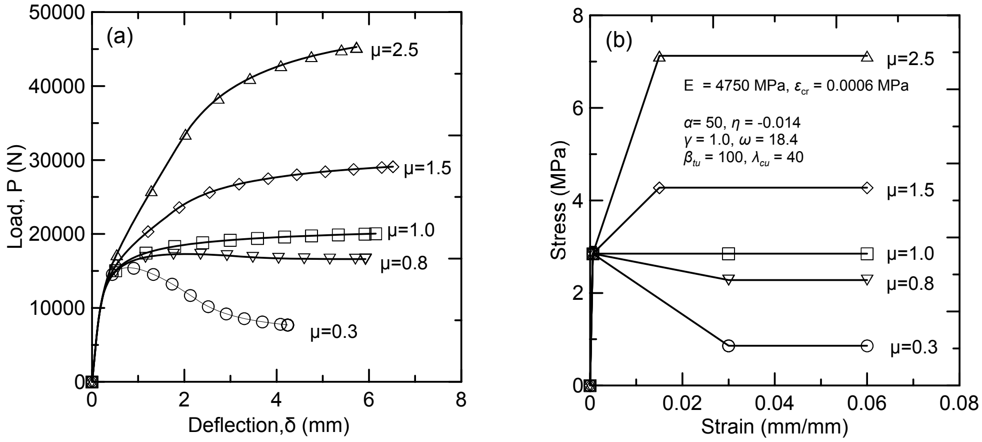

Figure 2.2.7. Parametric study of parameter μ as changes in (a) load deflection and (b) stress strain (hardening).

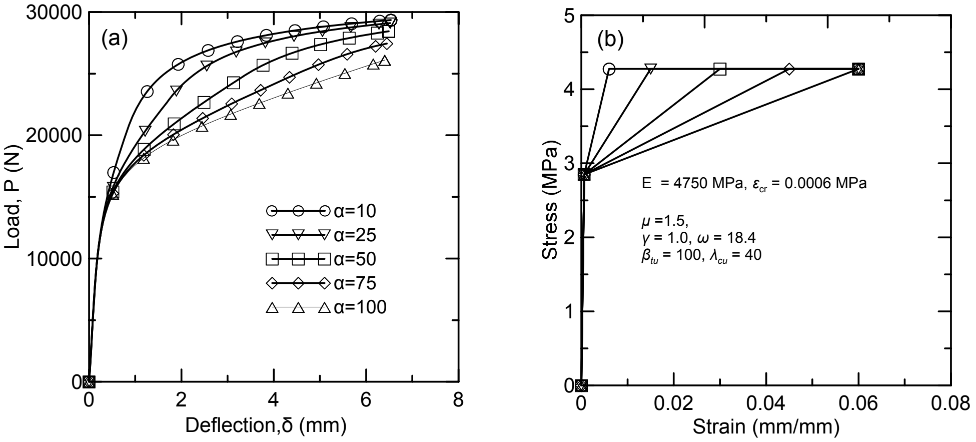

Figure 2.2.8. Parametric study of parameter α *as changes in (a) load deflection and (b) stress strain (hardening).*

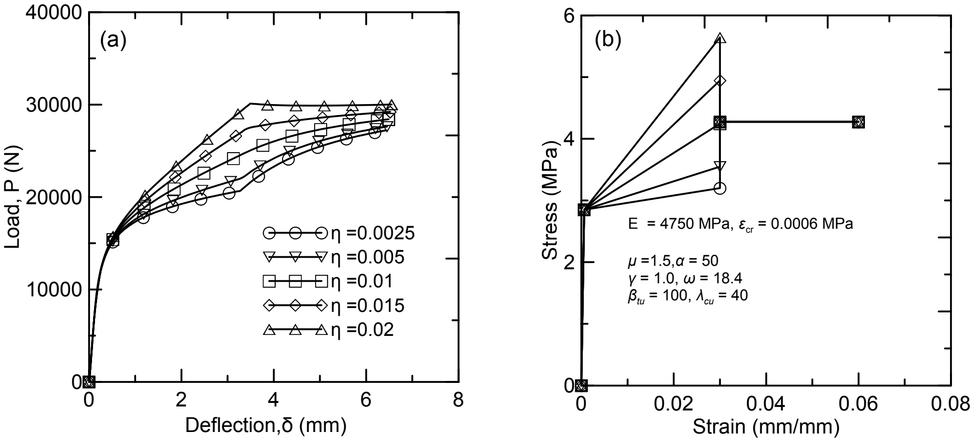

Figure 2.2.9. Parametric study of parameter η *as changes in (a) load deflection and (b) stress strain (hardening).*

Size of the crack localization zone, L_p, affects the general softening behavior in the post peak zone in the load deflection curve and as shown by Fig. 2.2.10

However it is important to note that the simulated residual load capacity is not sensitive to the crack localization length at deflections in excess of 0.5 mm.

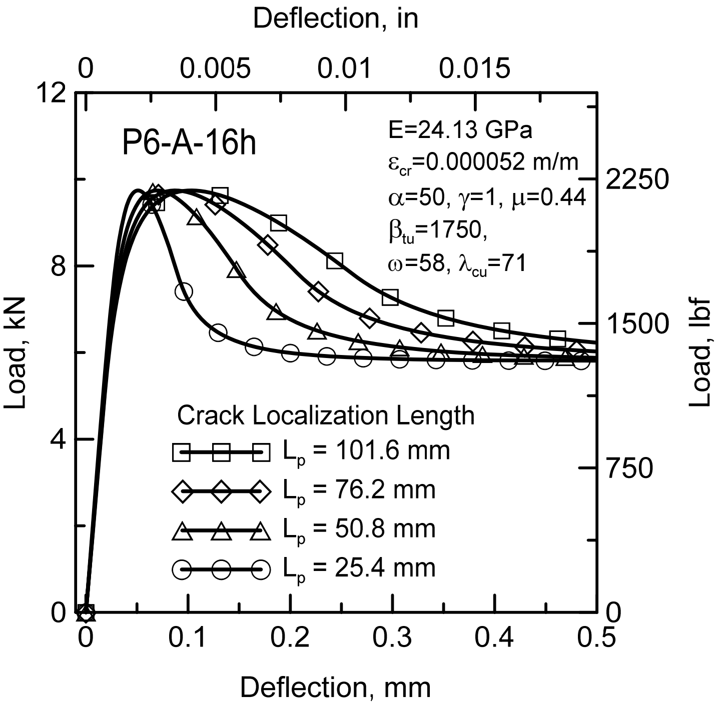

Figure 2.2.10 Parametric studies on the effects of crack localization zone (Lp) on the load deflection curves.

2.3 Representation of Residual Strength by Various Code Organizations

Residual strength proposed by standard test methods are not a true stress measure but an engineering stress computed using simple engineering bending theory for linear elastic materials and gross (un-cracked) section properties [3, 4, 5]. However, these values may be commonly used for the design of structural members which may lead to overestimation of the residual strength and inattentive consequences. Fig. 2.3.1a-d shows the stress distribution during the loading across the depth of the section using the present model. In the post-peak region due to the crack propagation, the neutral axis moves up toward the compression zone, a uniform tensile stress distribution is distributed over the tensile zone. The three stages of A, B, and C correlate with the stress distribution during the elastic, cracking and softening stages as they correspond to the load deflection results. The normalization of the post peak load with respect to the elastic section modulus is thus not appropriate and would lead to erroneous estimations. Fig. 2.3.1d implies that the stress distribution using standard residual flexural strengths proposed by JCI, RILEM and ASTM is un-conservative as it overestimates the post-peak tensile strength. This figure shows the degree of error with the assumption that the neutral axis remains constant during loading. Different standard methods for calculation of residual strength are discussed in the following sections and a proposed scale factor for equivalent residual strength is derived for each toughness measure. The early aged toughness data comes from a previous study where early aged FRC were compared at ages 8 to 36 hours [36].

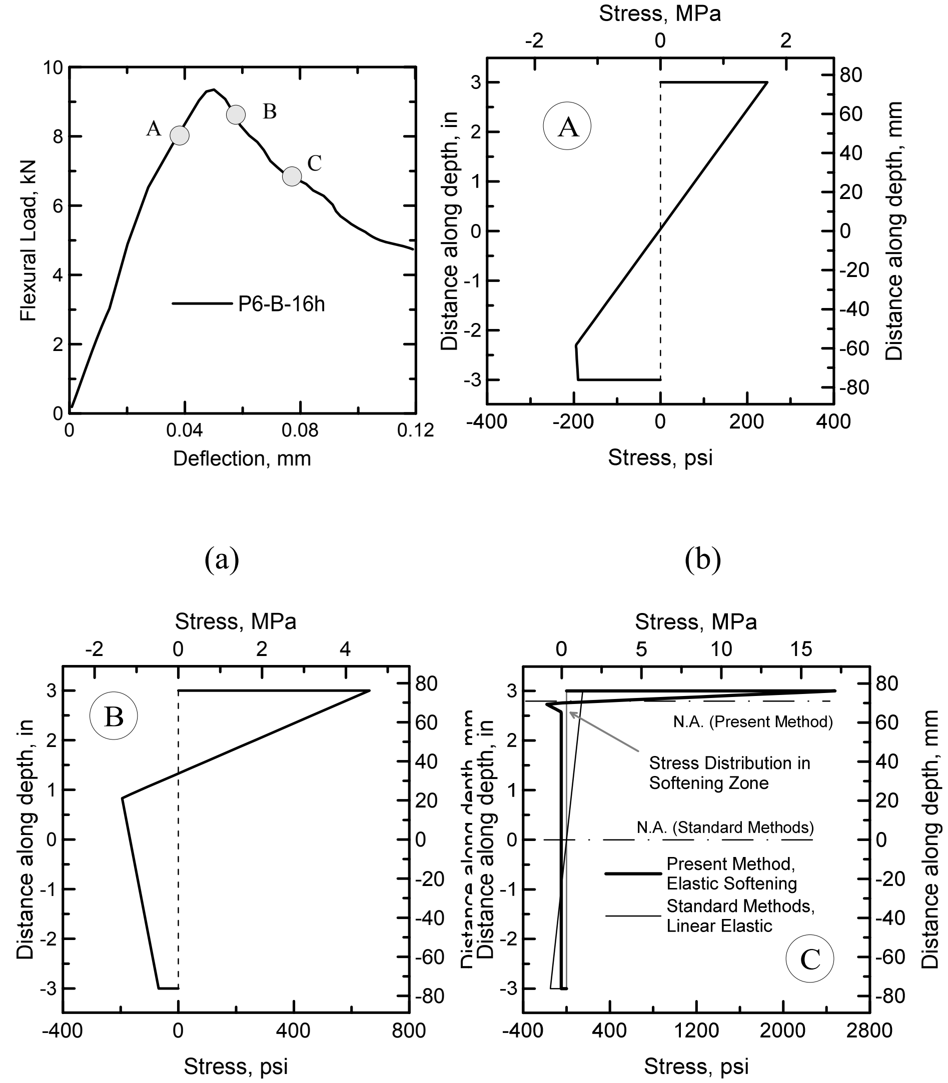

(a) (b)

(c) (d)

Figure 2.3.1. Development of stress profile over sample cross section during bending test: a) a typical flexural response, b) stress profile at point A, c) stress profile at point B, d) stress profile at point C.

2.3.1. Residual Strength by ASTM C 1609 ($\boldsymbol{f_{150}^{D}}$)

In this method, beam specimens having a square cross-section of fiber-reinforced concrete are tested in flexure using a third-point loading arrangement under a closed-loop, servo-controlled testing system. Load and net deflection are monitored and recorded to an end-point deflection of at least L/150. According to ASTM C 1609 [3], the residual strengths (f_{150}^{D}) is calculated using the residual load determined at net deflection values of 1/150 of the span length and Eq. (2.25).

$$f_{150}^{D} = \frac{P_{150}^{D}\, L}{bd^{2}} \tag{2.25}$$

where, L is the span length (mm), P_{150}^{D} is the residual load at net deflection of L/150 (N), b is the average width of the specimen (mm), and d is the average depth of the specimen (mm).

2.3.2 Residual Strength by JCI-SF4 ($\boldsymbol{\sigma_b}$)

Similar to ASTM C 1609, JCI-SF recommends testing fiber reinforced concrete by third-point loading and measuring the net deflection by Linear Variable Differential Transformers (LVDTs). Equivalent flexural strength (σ_b) is calculated by Eq. (2.26) [5].

$$\sigma_b = \frac{T_b}{\delta_{tb}} \cdot \frac{L}{bd^2} \qquad (2.26)$$

where, σ_b is the equivalent flexural strength (N/mm^2), T_b is the flexural toughness (N.mm), L is the span length (mm), δ_{tb} is the deflection of 1/150 of span (mm), b is the width of failed cross-section (mm) and d is the height of failed cross-section (mm).

2.3.3. Residual Strength by RILEM TC 162-TDF ($f_{eq,3}$)

According to RILEM TC 162-TDF [4] bending test method can be used for the determination of residual flexural tensile strength. In the RILEM method, the tensile behavior of fiber reinforced concrete is obtained by the load-deflection curve when a simply supported notched beam of 150 x 150 mm cross section and 500 mm is loaded under three-point bending arrangement and the test is executed by means of CMOD (Crack Mouth Opening Displacement) control. The residual flexural tensile strength ($f_{eq,3}$) is defined with respect to δ_3, when this specific deflection is:

$$\delta_3 = \delta_L + 2.65 \text{ mm (mm)} \qquad (2.27)$$

where, δ_L is the deflection at the limit of proportionality (mm).

As shown in Fig. 2.3.2, the energy absorption capacity, $D_{Bz,3}$ which is equal to the area under the load-deflection curve up to a deflection δ_3 consists of two parts. The part that includes the influence of steel fibers ($D^f_{BZ,3}$) is used for calculation of the equivalent flexural tensile strength, $f_{eq,3}$, by means of the following equation.

$$f_{eq,3} = \frac{3}{2}\left(\frac{D^{f}_{BZ,3}}{2.5}\right) \cdot \frac{L}{b{h_{sp}}^{2}} \tag{2.28}$$

where, L is the span length (mm), b is the width of the specimen (mm), and h_{sp} is the distance between tip of the notch and top of cross section (mm).

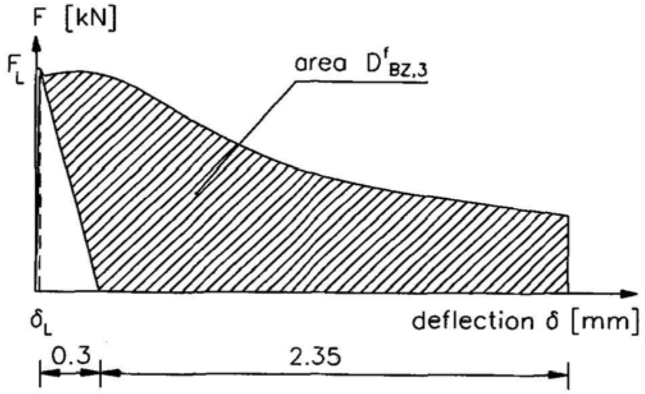

Fig. 2.3.2. The area under load-deflection curve which is used for calculation of residual flexural strength of FRCs by the RILEM method.

2.4 Model Extension for Hybrid Section with Continuous Reinforcement and Fibers

The solutions provided for a FRC beam can be extended to a reinforced concrete section containing reinforcement. Geometrical parameters are defined as a combination of normalized parameters and beam dimensions: width b and full depth *h*. Figure 2.4.1 (a) shows a beam cross section that contains an area of steel $A_s = \rho_g bh$ at the reinforced depth $d = \alpha h$. Note that the reinforcement ratio ρ_g is defined per gross sectional area *bh,* as opposed to effective area *bd* normally used for reinforced concrete. Figure 2.4.1(b) presents the elastic-perfectly plastic steel model, which is similar to the compression model using yield strain $\varepsilon_{\mathrm{sy}} = \kappa\varepsilon_{cr}$ and yield stress $f_{sy} = \kappa n\varepsilon_{cr}E$ as defined by normalized parameters: κ and n. There is no termination level specified for steel strain as it is assumed infinite plastic material. The material models for tension and compression of FRC are as before for the special case of elastic softening response (μ =0, and μ=1) discussed in Equation 8-11, the model for FRC and steel rebar are presented as:

$$\frac{\sigma_t(\beta)}{E\varepsilon_{cr}} = \begin{cases} \beta & 0 \le \beta \le 1 \\ \mu & 1 < \beta \le \beta_{tu} \\ 0 & \beta > \beta_{tu} \end{cases} \quad ; \quad \frac{\sigma_c(\lambda)}{E\varepsilon_{cr}} = \begin{cases} \gamma\lambda & 0 \le \lambda \le \omega \\ \gamma\omega & \omega < \lambda \le \lambda_{cu} \\ 0 & \lambda > \lambda_{cu} \end{cases} \qquad (2.4.1)$$

$$f_s(\varepsilon_s) = \begin{cases} E_s\varepsilon_s & 0 \le \varepsilon_s \le \varepsilon_{sy} \\ E_s\varepsilon_{sy} & \varepsilon_s > \varepsilon_{sy} \end{cases} \quad ; \quad \frac{f_s(\chi)}{E\varepsilon_{cr}} = \begin{cases} n\chi & 0 \le \chi \le \kappa \\ n\kappa & \chi > \kappa \end{cases} \qquad (2.4.2)$$

where normalized strains are defined as $\beta = \varepsilon_{tt}/\varepsilon_{cr}$, $\lambda = \varepsilon_c/\varepsilon_{cr}$ and $\chi = \varepsilon_s/\varepsilon_{cr}$. In derivation of moment curvature equations, the Kirchhoff hypothesis of plane section remaining plane is assumed. A normalized compressive strain at the top concrete fiber λ is used as the independent variable to incrementally impose flexural deformation, which is defined in three stages. The first stage or the elastic range ($0 < \lambda \le \lambda_{R1}$) corresponds to the compressive strain ranging from zero to the point where the tensile strain at the bottom fiber reaches the first cracking tensile strain. Stage 2 ($\lambda_{R1} < \lambda \le \omega$) corresponds to the compressive strain in the elastic range and the tensile strain is in post crack region. Finally, stage 3 ($\omega < \lambda \le \lambda_{cu}$)

corresponds to the compressive strain in plastic range while the tensile strain is in post crack range. For stage 2 and 3 two possible scenarios exist: the steel is either elastic ($\varepsilon_s \leq \varepsilon_{sy}$) or yielding. ($\varepsilon_s > \varepsilon_{sy}$).

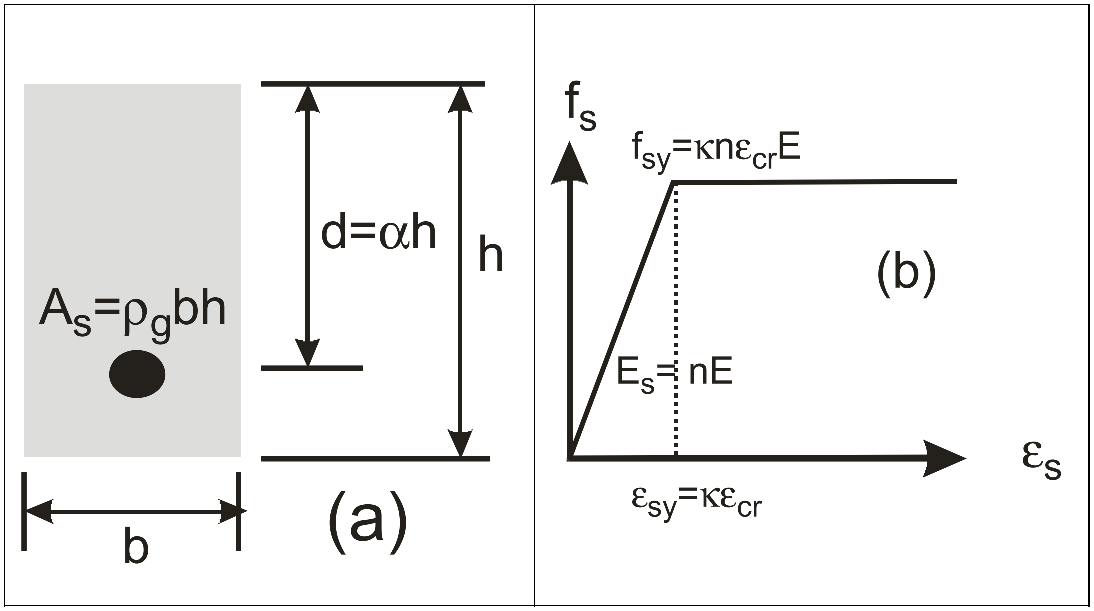

Figure 2.4.1-Material model for single reinforced concrete design (a) steel model; (b) beam cross section.

Steps in the determination of net section force, moment, and curvature at each stage of normalized compressive strain, λ are similar to the previous cases and complete derivation can be found in [36]. When steel is elastic in stages 1, 2.1 and 3.1, the expressions for net force are in the quadratic forms and result in two possible solutions for k. With a large scale of numerical tests covering a practical range of material parameters, only one solution yields the valid value in the range $0 < k < 1$. During stage 1, the singularity of k_1 is found when $\gamma = 1$, thus additional expression for k_1 is derived by taking the limit as $\gamma \rightarrow 1$. On the other hand, when steel yields in stage 2.2 or 2.3, there is only one valid solution for k. The moment M_i, curvature ϕ_i and effective flexural stiffness K_i for each stage i, are normalized with respect to their values at cracking of plain fiber reinforced concrete M_{cr}, ϕ_{cr} and K_{cr} respectively and their closed form solutions M_i', ϕ_i' and K_i' are presented in Table 2.4.1.

$$M_i = M_i' M_{cr}; \qquad M_{cr} = \frac{1}{6} bh^2 E \varepsilon_{cr} \tag{2.4.3}$$

$$\phi_i = \phi_i' \phi_{cr}; \qquad \phi_{cr} = \frac{2\varepsilon_{cr}}{h} \tag{2.4.4}$$

$$K_i = K_i' K_{cr}; \qquad K_{cr} = \frac{1}{12} bh^3 \tag{2.4.5}$$

Since the compressive modulus E_c may not be equal to the tensile modulus E, the normalized compressive strain corresponding to end of elastic region 1 (λ_{R1}) must be determined from the strain gradient diagram.

$$\frac{\lambda_{R1}\varepsilon_{cr}}{kh} = \frac{\varepsilon_{cr}}{(1-k)h} \tag{2.4.6}$$

Table 2.4.1: Normalized neutral axis, moment, curvature and stiffness for each stage of normalized compressive strain at top fiber (λ)

Stage		***k***	***M'***	***ϕ'***	***K'***
1	$0 < \lambda \le \lambda_{R1}$	$k_1 = k_{1\gamma}$	$M_1' = \frac{2\lambda}{k_1}\left[C_1k_1^3 + C_2k_1^2 + C_3k_1 + C_4\right]$	$\phi_1' = \frac{\lambda}{2k_1}$	$K_1' = \frac{M_1'}{\phi_1'}$
2.1	$\lambda_{R1} < \lambda \le \omega$ $\varepsilon_s \le \varepsilon_{sy}$	$k_{21} = \frac{\lambda}{B_1}\left(B_2 + \sqrt{B_3 + 2\alpha\rho_g nB_1}\right)$	$M_{21}' = \frac{1}{\lambda^2 k_{21}}\left[C_5k_{21}^3 + C_6k_{21}^2 + C_7k_{21} + C_8\right]$	$\phi_{21}' = \frac{\lambda}{2k_{21}}$	$K_{21}' = \frac{M_{21}'}{\phi_{21}'}$
2.2	$\lambda_{R1} < \lambda \le \omega$ $\varepsilon_s > \varepsilon_{sy}$	$k_{22} = \frac{B_4}{B_1}$	$M_{22}' = \frac{1}{\lambda^2}\left[C_5k_{22}^2 + C_9k_{22} + C_{10}\right]$	$\phi_{22}' = \frac{\lambda}{2k_{22}}$	$K_{22}' = \frac{M_{22}'}{\phi_{22}'}$
3.1	$\omega < \lambda \le \lambda_{cu}$ $\varepsilon_s \le \varepsilon_{sy}$	$k_{31} = \frac{\lambda}{B_5}\left(B_2 + \sqrt{B_3 + 2\alpha\rho_g nB_5}\right)$	$M_{31}' = \frac{1}{\lambda^2 k_{31}}\left[C_{11}k_{31}^3 + C_6k_{31}^2 + C_7k_{31} + C_8\right]$	$\phi_{31}' = \frac{\lambda}{2k_{31}}$	$K_{31}' = \frac{M_{31}'}{\phi_{31}'}$
3.2	$\omega < \lambda \le \lambda_{cu}$ $\varepsilon_s > \varepsilon_{sy}$	$k_{32} = \frac{B_4}{B_5}$	$M_{32}' = \frac{1}{\lambda^2}\left[C_{11}k_{32}^2 + C_9k_{32} + C_{10}\right]$	$\phi_{32}' = \frac{\lambda}{2k_{32}}$	$K_{32}' = \frac{M_{32}'}{\phi_{32}'}$

where, the coefficients are:

$B_1 = \gamma\lambda^2 + 2\mu(\lambda+1) - 1$; $B_2 = \mu - \rho_g n\lambda$; $B_3 = \rho_g n\left(\rho_g n\lambda^2 - 2\mu\lambda\right) + \mu^2$; $B_4 = 2\lambda\left(\rho_g n\kappa + \mu\right)$; $B_5 = 2\gamma\omega\lambda - \gamma\omega^2 + 2\mu(\lambda+1) - 1$

$C_1 = \gamma - 1$; $C_2 = 3\left(\rho_g n + 1\right)$; $C_3 = -3\left(2\rho_g n\alpha + 1\right)$; $C_4 = 3\rho_g n\alpha^2 + 1$; $C_5 = 2\gamma\lambda^3 + 3\mu\left(\lambda^2 - 1\right) + 2$; $C_6 = 6\lambda^2\left(\rho_g n\lambda - \mu\right)$

$C_7 = 3\lambda^2\left(\mu - 4\rho_g n\alpha\lambda\right)$; $C_8 = 6\rho_g n\alpha^2\lambda^3$; $C_9 = -6\lambda^2\left(\rho_g n\kappa + \mu\right)$; $C_{10} = 3\lambda^2\left(2\rho_g n\alpha\kappa + \mu\right)$; $C_{11} = 3\gamma\omega\lambda^2 - \gamma\omega^3 + 3\mu\left(\lambda^2 - 1\right) + 2$

$$k_{1\gamma} = \begin{cases} \dfrac{1+\rho_g n-\sqrt{{\rho_g}^2 n^2+2\rho_g n\left(1-\alpha+\alpha\gamma\right)+\gamma}}{1-\gamma} & \gamma \neq 1 \\ \dfrac{2\rho_g n\alpha+1}{2\left(\rho_g n+1\right)} & \gamma = 1 \end{cases}$$

By substituting k_1 from Table 2.4.1 for k in Eq. (2.4.6) and solving for λ_{R1}, one obtains:

$$\lambda_{R1}=\begin{cases}-\dfrac{1+\rho_g n-\sqrt{\rho_g{}^2n^2+2\rho_g n(1-\alpha+\alpha\gamma)+\gamma}}{\gamma+\rho_g n-\sqrt{\rho_g{}^2n^2+2\rho_g n(1-\alpha+\alpha\gamma)+\gamma}} & when\ \gamma\neq 1\\ -\dfrac{2\rho_g n\alpha+1}{2\rho_g n(\alpha-1)-1} & when\ \gamma=1\end{cases} \tag{2.4.7}$$

The yield condition for tensile steel can be checked by first assuming that it yields and then using k_{22} or k_{32} in Table 2.4.1 for k in Eq. (2.4.8) to calculate the steel strain ε_s:

$$\varepsilon_s=\frac{\alpha-k}{k}\lambda\varepsilon_{cr} \tag{2.4.8}$$

If ε_s is greater than ε_{sy}, the assumption is correct, otherwise steel has not yielded and one has to use k_{21} or k_{31}. Once, the neutral axis parameter k and the applicable case are determined, the appropriate expressions for moment, curvature and stiffness in Table 2.4.1 and Equations 2.4.1-2.4.6 are then used to generate moment curvature response and its flexural stiffness.

To avoid compression failure occurring in ultimate stage, the steel used in flexural members must be less than the balanced reinforcement ratio $\rho_{g,bal}$, representing the simultaneous achievement of concrete compressive strain at failure ($\varepsilon_c = \varepsilon_{cu}$) with the steel reaching its yield limit ($\varepsilon_s = \varepsilon_{sy}$). The strain gradient in stage 3.2 represents the compressive strain in plastic range and tensile strain in the post crack region, is used to derive the balance reinforcement ratio.

$$\frac{\lambda_{cu}\varepsilon_{cr}}{kh} = \frac{\kappa\varepsilon_{cr}}{(\alpha - k)h} \tag{2.4.9}$$

By substituting λ_{cu} in the expression for k_{32} in Table 2.4.1 and then use it for k in Eq. (2.4.9), one can solve for the balance reinforcement ratio as:

$$\rho_{g,bal} = \frac{2\mu\left(\lambda_{cu}(\alpha - 1) + \alpha - \kappa\right) + \alpha\gamma\omega\left(2\lambda_{cu} - \omega\right) - \alpha}{2n\kappa\left(\lambda_{cu} + \kappa\right)} \tag{2.4.10}$$

Parametric studies of post crack tensile strength and reinforcement ratio as two main reinforcing parameters were conducted. Variations in the location of neutral axis, moment curvature response, and stiffness degradation of a beam section as flexural deformation increases are presented as normalized quantities with respect to first cracking parameters of plain FRC. Figure 2.4.2 shows typical material models for SFRC and steel rebar used in the parametric studies. Two material parameters: tensile modulus E of 24 GPa and the first cracking tensile strain ε_{cr} of 125 μstr were used. Other normalized parameters for tension and compression models of SFRC were: $\beta_{tu} = 160$, $\gamma = 1$, $\omega = 8.5$ and $\lambda_{cu} = 28$. The normalized parameters for steel rebar were: $n = 8.33$, $\kappa = 16$ and $\alpha = d/h = 0.8$. Post crack tensile strength parameter μ was varied from 0.00 to 1.00 and reinforcement ratio ρ_g was varied from 0.0 to 0.03.

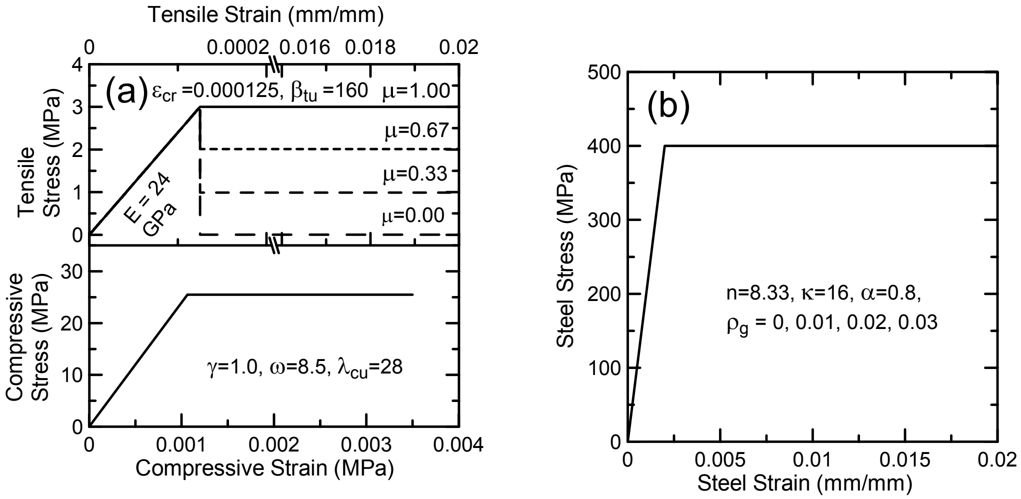

Figure 2.4.2-Material model for typical fiber reinforced concrete and rebar used in parametric studies; (a) concrete model; (b) steel model

Figure 2.4.3 shows the change of neutral axis depth ratio k as the compressive strain at top fiber λ increases. For plain FRC system ($\mu \geq 0, \rho_g = 0$), Figure 2.4.3(a) shows the neutral axis starts at 0.5 as expected for a material with equal compressive and tensile modulus ($\gamma = 1$), and then drops, at different rates, depending on the level of post crack tensile strength parameter μ. For brittle material represented by $\mu = 0.00$, k instantaneously drops to zero after initiation of cracking. As μ increases from 0.00 to 1.00, the rate of decrease in neutral axis k becomes slower. A very ductile FRC with elastic–plastic tensile behavior defined as $\mu = 1.00$ yields the maximum value of $k = 0.12$ at the ultimate compressive strain $\lambda_{cu} = 28$. For conventional reinforced concrete system ($\mu = 0, \rho_g \geq 0$), Figure 2.4.3(b) shows the effect of reinforcement ratio to the change of neutral axis. With reinforcement present in plain concrete ($\mu = 0$), the initial value of k is slightly higher than 0.5 because of the equivalent section criteria, however as ρ_g

increases, the descending rate is at a much slower rate. With a small amount of ρ_g = 0.01, the k reduces to 0.19 at λ_{cu} = 28, which is higher than k = 0.12 for ductile FRC (μ = 1.00). At higher levels of ρ_g between 0.02 and 0.03, k initially decreases, then increases to a relatively high value compared to the starting value. Figure 2.4.3(c) shows the effect of increasing post crack tensile strength for a fixed reinforcement ratio ρ_g = 0.01 the response is closer to those of plain FRC. The last Figure 2.4.3(d) shows the effect of increasing reinforcement ratio for a fixed level of post crack tensile strength μ = 0.33.

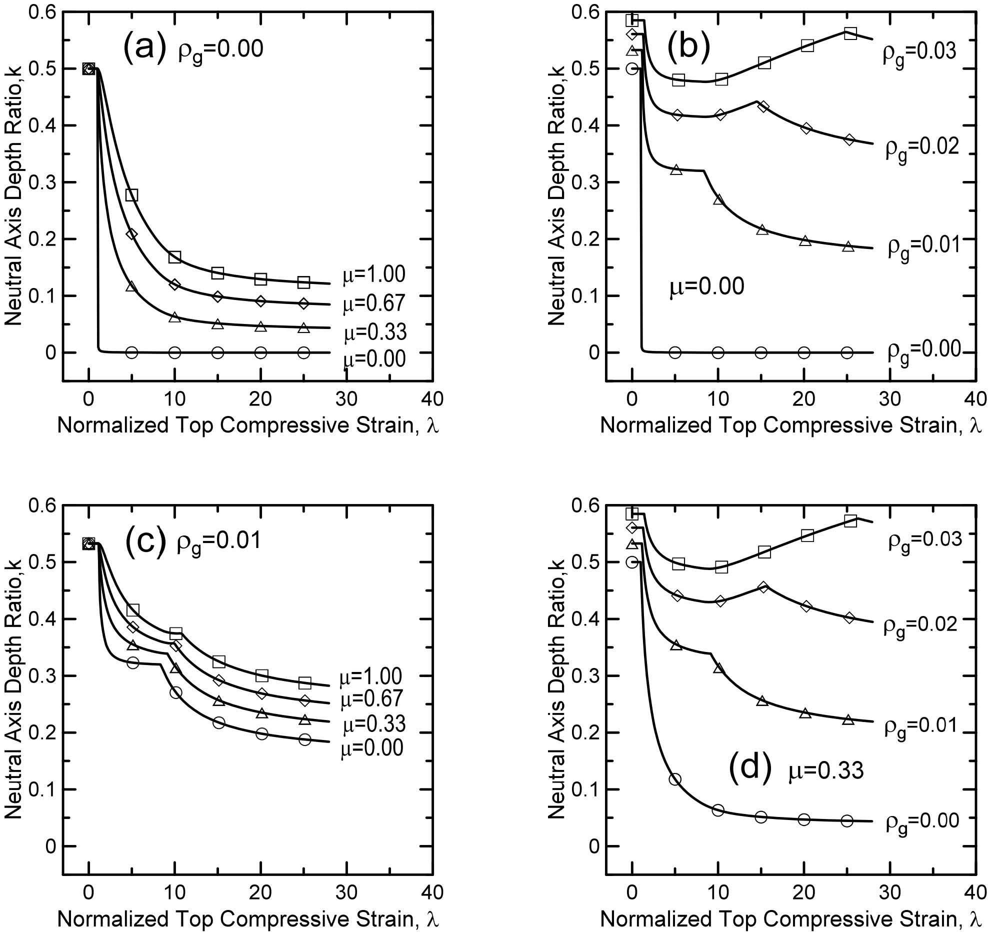

Figure 2.4.3-Parametric studies of neutral axis depth ratio for different levels of post crack tensile strength parameter μ and reinforcement ratio ρ_g.

Figure 2.4.4 shows the effect of parameters μ and ρ_g to the normalized moment-curvature response. Figure 2.4.4(a) shows that the moment curvature response of plain FRC system when post crack tensile strength increases from brittle ($\mu = 0$) to ductile ($\mu = 1$). At a value of $\mu = 0.33$, close to $\mu_{crit} = 0.35$ as defined in earlier sections, the flexural response is almost perfectly plastic, in which deflection softening starts to shift to deflection hardening. The elastic-plastic tensile response of FRC ($\mu = 1$) yields an upper bound normalized moment capacity of 2.7. In a more efficient reinforced concrete system that utilizes steel reinforcing bars as the main flexural reinforcement [Figure 2.4.4(b)], the maximum normalized moment capacity of 5.8 can be achieved by using ρ_g of only 0.01. Note that as ρ_g increases, the response changes from ductile under-reinforced to brittle over-reinforced section. Figure 2.4.4(c) reveals the response when varying post crack tensile strength for a fixed amount of reinforcement ratio ($\rho_g = 0.01$). The responses are similar to the curve using $\rho_g = 0.01$ in Figure 2.4.4(b) plus additional strength from post crack tensile strength ($\mu = 0.00 – 1.00$) as demonstrated in Figure 2.4.4(a). This system provides intermediate strength between the weaker plain FRC and the stronger conventional reinforced concrete. Figure 2.4.4(d) reveals that there is little benefit to use post crack tensile strength μ of 0.33 or less to the reinforced concrete system as the moment capacity slightly increases from the reinforced concrete without any fibers [Figure 2.4.4(b)]. It is noted that the ductility of each curve shown in Figure 2.4.4(d) is less than that of Figure 2.4.4(b). This is due to the fact that the tension capacity increases for an ultimate compressive strain capacity of 0.0035. In actual concrete mixtures, discrete fibers increase both the post crack tensile strength and ultimate compressive strain and may thus yield more ductile responses.

The ultimate moment capacity as a function of post crack tensile strength and reinforcement ratio can be presented as a convenient design chart for any combination of concrete and steel properties used in a beam section. The yielding condition of steel reinforcement can be identified by comparing ρ_g with the reinforcement ratio at balance failure as defined by Eq. 24. Once steel condition is determined, appropriate expressions for neutral axis k_{31} or k_{32} are then used to calculate the ultimate moment capacity M'_{31} or M'_{32}.

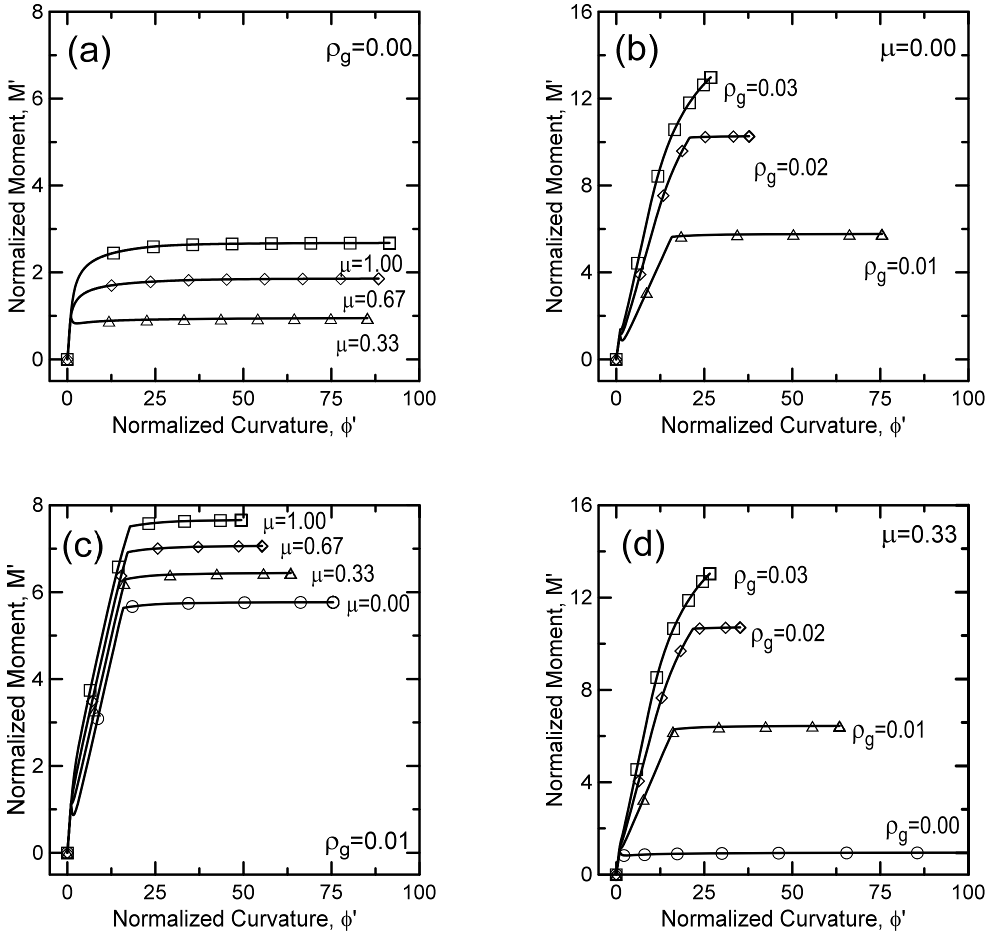

Figure 2.4.4- Parametric studies of normalized moment curvature diagram for different levels of post crack tensile strength parameter μ and reinforcement ratio ρ_g

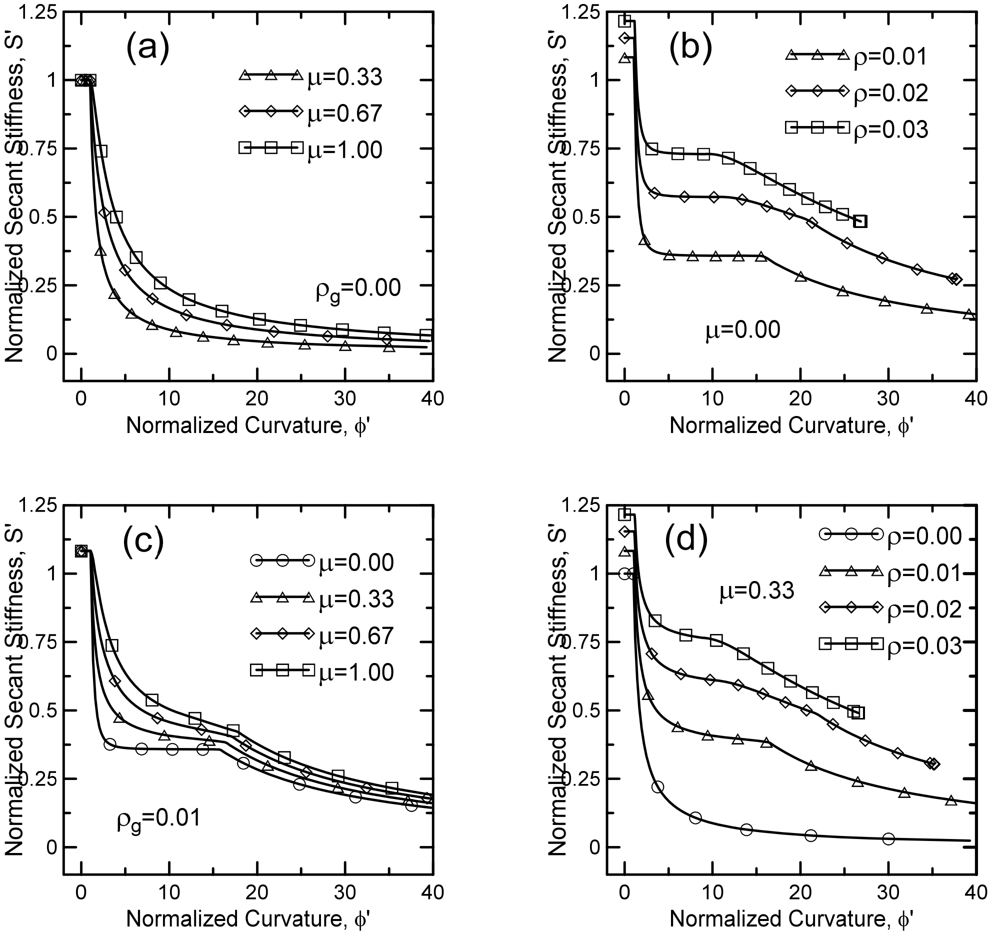

Figure 2.4.5 – Normalized secant stiffness and a function of normalized curvature.

Figure 2.4.6 shows a design chart for the concrete and steel previously used in the parametric studies. The material parameters are also provided in the chart. The normalized moment capacity strongly depends on the reinforcement ratio whereas extra capacity is provided by the post crack tensile strength. Under-reinforced sections are below the balance failure points ($\rho_g \leq \rho_{g,bal}$), and the moment capacity increases proportional to the reinforcement ratio. As ρ_g exceeds $\rho_{g,bal}$, the strength of all curves marginally increase as the added steel fails to yield. To design flexural members with this design chart, the ultimate moment M_u due to factored load is determined initially and then normalized with the M_{cr} cracking moment of the plain FRC to obtain required ultimate moment capacity M_u'. The chart is then used to select any combination of normalized post crack tensile strength μ and reinforcement ratio ρ_g that provides sufficient strength with reasonable safety factor for M_u'.

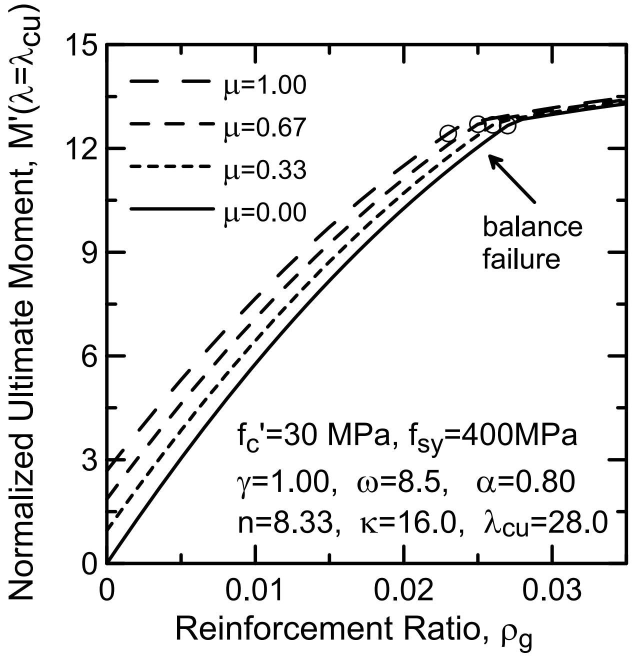

Figure 2.4.6-Design chart of normalized ultimate moment capacity for different levels of post crack tensile strength μ and reinforcement ratio ρg

Chapter 3

COMPARATIVE EVALUATION OF EARLY AGE TOUGHNESS PARAMETERS IN FIBER REINFORCED SHOTCRETE

3.1 Introduction

Design of fiber reinforced shotcrete linings for ground support requires the use of material properties that are obtained from an experimental program. The material property data is incorporated in analytical and empirical computer simulations of shotcrete curing.

This study includes two separate sets of data. The first is the presentation of the flexural test data that was conducted at the Resolution Copper Mine (RCM) testing lab to investigate quality control measures for fiber reinforced shotcrete being used for a shaft lining system. The experimental analysis and the back-calculated material properties are tabulated and discussed. The second data set is presented from an early aged study of polymeric and glass fibers as fiber reinforced concrete (FRC) conducted at Arizona State University. The effects of age at 8, 16 and 36 hours on residual strength, maximum load capacity and deflection capacity are investigated. This early age study of polymeric and glass fibers in addition to the shaft lining shotcrete provide a more complete picture of the residual strength characterization in early age fiber reinforced composites.

Methods by which the ASTM, JCI and RILEM standards determine residual strength are brought into question. Comparisons are made with a previous study where early age strength gain was a primary focus. The fact that these standards assume a non-cracked section presents an over-estimation in their residual strengths, applying the need for caution when using them. The ASTM residual strength parameter will be checked against the model output for the FRS in this study.

3.2 Fiber Types

Fibers are added to shotcrete to increase the post cracking load capabilities. Properties of a single type of Modified Olefin fiber manufactured by Barchip (formerly Shogun) are shown in Table 3.2.1. As shown in the table, the base, specific gravity, modulus of elasticity, tensile strength and length of used fibers cover a specific range as required. These fibers are used for both flexural and RDP samples.

Table 3.2.1 – Physical properties of the Barchip polymeric fibers used in the shotcrete mix design.

Property	**Value**
Base	Modified Olefin
Length	54mm
Tensile Strength	640 Mpa
Surface Texture	Continuously Embossed
Specific Gravity	0.90 - 0.92
Elastic Modulus	10 Gpa

Addition of synthetic structural fiber to plain concrete beams has shown similar equivalent flexural strength values to steel fiber reinforced concrete [37]. In addition, the scatter of experimental results of concrete beams in the post-peak region is much smaller for synthetic fibers than steel fibers due to the higher number and the more homogeneous distribution of the synthetic fibers over the fracture surface [28]. Therefore, synthetic fibers including different types of polymeric fibers and one type of AR-glass fiber are used to study post-peak response of early-age FRC. Physical and mechanical properties of the fibers used in the early age study are presented in Table 3.2.2.

Table 3.2.2. Properties of fibers used in early age study.

Fiber Type	P-Type A	P-Type B	P-Type C	P-Type D	ARG
Base	Modified Olefin	Monofilament Polypropylene/ Polyethylene Blend	Modified Polypropylene Blend	Fibrillated Polypropylene	Alkali Resistant Glass
Specific Gravity	0.9-0.92	0.92	0.91	0.91	2.68
Modulus of Elasticity (MPa)	10,000	5,000	6,500	5516	69,000
Tensile Strength (MPa)	552	600-650	655	414	1724
Length of Fiber (mm)	50	50	38	50	25

3.3 Mix Design

The shotcrete mix used for both flexural and RDP samples is shown in Table 3.3.1 A critical design parameter for the shotcrete mix design is high early age strength. The addition of both water reducer and super plasticizer contribute to 24 hour window for maximum strength gain. A water/cement ratio of 0.41 and fiber dosage of 6.5 kg/m^{3}was maintained for all samples. The fly ash and silica fume were added to some of mixtures as supplementary cementitious materials with the dosage of 60kg/m^3 and 24kg/m^3 respectively.

Table 3.3.1 – Shotcrete mix proportions for both flexural and RDP tests.

Portland Cement (kg/m3)	Fly Ash (kg/m3)	Silica Fume (kg/m3)	Fine Aggre-gate (kg/m3)	Coarse Aggre-gate (kg/m3)	Water (kg/m3)	Fiber Type /dosage (kg/m3)	Water Reducer (ml)	S.P. (ml)	w/cm
463	59	24	1091	418	151	6.5	7453	7689	0.41

Mixture proportions of eight different mixtures prepared and tested under three-point bending configuration for the early age study are shown in the Table 3.3.2. The first letter on the samples' labels refers to the general type of fiber used, i.e. P in case of polymeric and G in case of glass fiber. The following number is the dosage of the fiber presented in kg/m^3 and for polymeric fiber another letter follows this number referring to the type of polymeric fibers shown in Table 3.2.2. The final number in the labels shows the age of samples. As shown in Table 3.3.2, the w/cm ratio for polymeric fiber samples are 0.42 and for glass fiber samples is 0.55. The cement content is 475 and 650 kg/m^3 for polymeric and glass fiber samples, respectively. The fly ash and silica fume were added to the polymeric fiber mixtures as supplementary cementitious materials at two different dosages of 60 kg/m^3 and 15 kg/m^3, respectively. The sand-to-cement (s/cm) ratio is 2 for all mixtures and accelerator admixtures with the dosage of 4% and 8% were added to the polymeric fiber mixtures leading to high early strength. Since the primary objective was strength development, the criteria to gain compressive strength of minimum 25 MPa at 24 h was used to adjust the level of accelerating admixture which was mixed at the nozzle. Development of tensile properties during the first 36 hours was one of the main objectives, and therefore, samples were tested at 8, 16, and 36 h respectively.

Table 3.3.2. Mixture proportions and compressive strength of all mixes used in early age study

Mix ID	Portland Cement (kg/m3)	Fly Ash (kg/m3)	Silica Fume (kg/m3)	Fine Aggre-gate (kg/m3)	Coarse Aggre-gate (kg/m3)	Water (kg/m3)	Fiber Type /dosage (kg/m3)	Acce-lerator (%)	w/cm	s/cm	Compress-ive Strength, MPa
P6-A	475	60	15	1100	450	230	P-B/6	4	0.42	2	34[a]
P7-A	475	60	15	1100	450	230	P-B/7	4	0.42	2	32[a]
P9-A	475	60	15	1100	450	230	P-B/9	8	0.42	2	40[a]
P6-B	475	60	15	1100	450	230	P-A/6	4	0.42	2	29[a]
P6-C	475	60	15	1100	450	230	P-C/6	4	0.42	2	29[a]
P6-A&D	475	60	15	1100	450	230	P-B&D/5,1	4	0.42	2	29[a]
P6-C&D	475	60	15	1100	450	230	P-C&D/5,1	4	0.42	2	26[a]
G3	650	0	0	1310	0	360	ARG/3	0	0.55	2	32[b]

a Results are for the age of 24 hours
b Results are for the age of 28 days

3.4 Four Point Bending Flexural Test (ASTM C-1609)

This test method evaluates the flexural performance of fiber-reinforced concrete using parameters derived from the load-deflection curve obtained by testing a simply supported beam under third-point loading using a closed-loop, servo-controlled testing system.

The flexural samples cross sectional dimensions were 150mm x 150mm with an effective span of 450mm, with the load applied at third points on the span. A similar test setup is shown in Fig 3.4.1. This test procedure was used exclusively for the shotcrete testing.

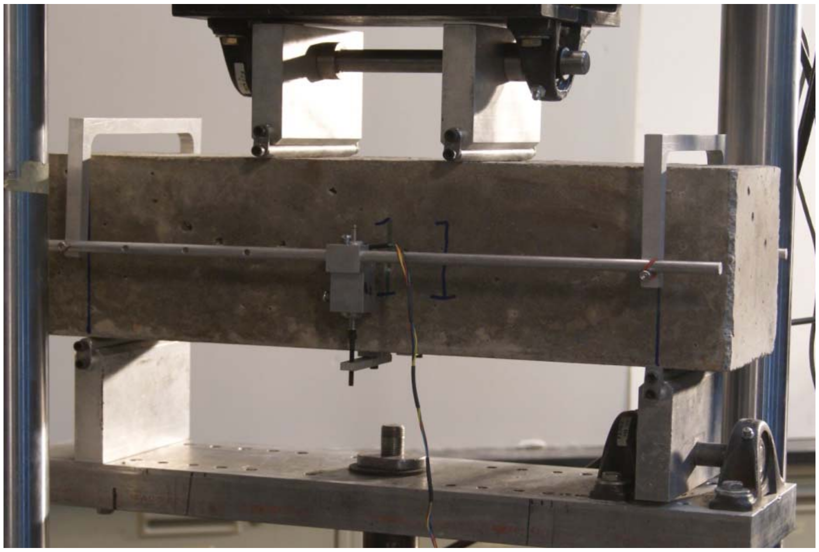

Figure 3.4.1 – Typical four-point bend test setup.

In order to monitor post-peak flexural response of samples in the early age study using closed loop testing, samples were pre-notched and load was applied along the notch. Similar to RILEM TC 162-TDF recommendation [4], beams were loaded at a single point in the mid-span also known as the three-point bending test (see figure 3.4.2). Polymeric-FRC sample dimensions were 0.53m x 0.15m x 0.15m with an initial notch length of 25 mm, and test span of 0.45 m. Dimensions of AR glass-FRC samples were 0.45m x 0.1m x 0.1m with an initial notch length of 12 mm and test span of 0.40 m, respectively. Tests were performed under closed loop control with Crack Mouth Opening Deformation (CMOD) as the controlled variable. Fig. 3.4.2 shows a typical concrete beam under a closed-loop three-point bending test setup. The CMOD was measured across the face of notch using a Linear Variable Differential Transformer (LVDT) with a working range of 2.5 mm. Closed loop control tests were conducted with a CMOD rate of 0.12 mm/min up to a CMOD level of 3 mm. The deflection of the beam at the mid-span was measured using another LVDT. It is observed that cracks initiate from the notch and extend up to the upper side of the beam; however, the crack is bridged by the fibers which are being pulled under this loading. The presence of fiber significantly increases the ductility of the material and makes the crack opening and deflection exceed 1.2 mm. The load deflection curve is characterized by the maximum load and its associated deflection, elastic stiffness, maximum flexural strength and flexural toughness, and residual strengths by ASTM C 1609 (f_{150}^{D}), JCI-SF4 (σ_b) and RILEM TC 162-TDF ($f_{eq,3}$).

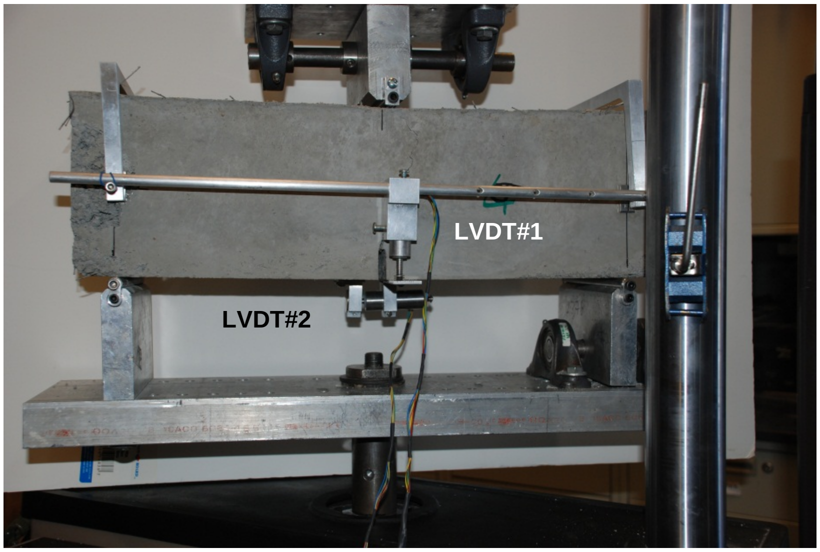

Figure 3.4.2. Test setup for three-point bend flexural test.

3.5 Results and Discussion for Shotcrete Analysis

Results of four-point bending test for Barchip Polymeric fibers are summarized in Table 3.5.1. These results are representative for the outlined mixture and include all replicates forwarded from RCM.

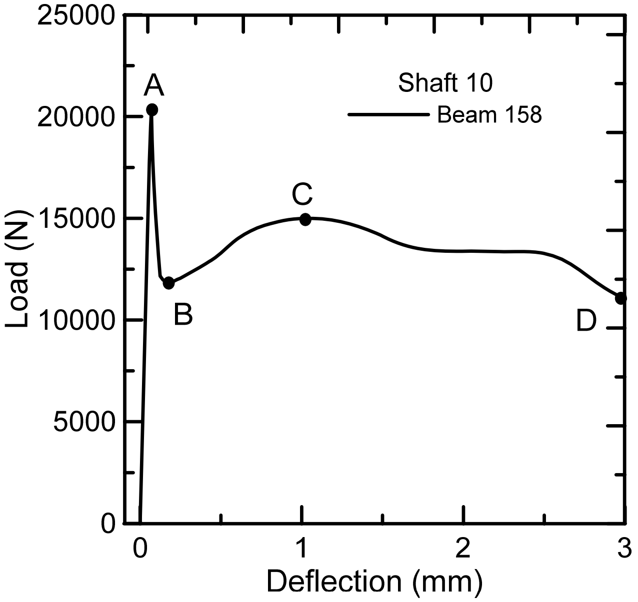

Figure 3.5.1. Smoothed load-deflection curve with key points of analysis; A - Point of 1st cracking, B – Post crack transition point, C – Post cracking maximum load, D – Maximum deflection.

Table 3.5.1 – Summary of experimental four-point bending flexural data for shotcrete.

Beam ID	Bending Strength, (MOR) MPa	Flexural Stiffness, kN/mm	Load @ 1st Crack, kN	Defl @ 1st Crack, mm	Max Flex Load, kN	Defl. @ Max Load, mm	Deflection Capacity, mm	Flexural Toughness, (GF) kN-mm
155	1.904	313	9.72	0.031	14.28	0.0602	2.997	30.85
156	2.019	313	10.35	0.033	15.14	0.064	3.019	31.41
157	2.319	391	11.81	0.03	17.40	0.0586	3.019	38.71
158	2.759	391	15.19	0.039	20.69	0.0643	3.012	41.32
160	2.485	339	14.14	0.042	18.64	0.0681	3.038	43.67
161	2.606	339	15.11	0.045	19.55	0.0722	3.092	38.85
162	2.024	339	9.95	0.029	15.18	0.0642	2.993	35.55
164	3.123	391	19.13	0.049	23.42	0.0662	3.043	46.49
168	2.923	365	17.85	0.049	21.92	0.0663	3.05	46.35
169	3.867	443	23.59	0.053	29.01	0.0722	2.965	61.25

170	3.401	417	18.60	0.045	25.51	0.0741	3.02	55.81
171	3.541	417	19.44	0.047	26.56	0.0773	2.994	54.75
192	1.53	287	8.50	0.03	11.48	0.0489	2.931	19.53
194	2.146	287	13.20	0.046	16.10	0.0622	3.009	28.58
195	2.146	287	13.20	0.046	16.10	0.0622	3.009	28.58
196	2.489	287	15.26	0.053	18.67	0.072	2.952	34.74
198	3.931	483	25.67	0.053	29.48	0.0699	3.051	66.20
199	3.805	483	24.98	0.052	28.54	0.0679	2.962	58.64
200	4.079	548	26.78	0.049	30.60	0.0641	2.961	62.93
201	1.462	261	7.13	0.027	10.96	0.06	2.98	27.07
202	1.649	261	9.00	0.035	12.37	0.0574	2.979	27.45
203	1.751	261	9.53	0.037	13.14	0.0609	2.999	30.73
204	2.472	391	14.06	0.036	18.54	0.0587	2.994	42.93
205	2.878	391	16.88	0.043	21.59	0.0695	3.037	37.16
207	2.432	365	12.81	0.035	18.24	0.0671	2.992	26.22
208	2.347	365	13.02	0.036	17.60	0.0589	2.994	31.07
209	2.425	365	13.44	0.037	18.19	0.0608	2.994	32.61
210	2.154	339	10.63	0.031	16.15	0.0685	2.906	28.80
211	2.301	352	12.66	0.036	17.26	0.0596	3.031	35.20
212	1.267	261	6.15	0.024	9.51	0.0518	2.916	20.09
213	2.274	365	12.39	0.034	17.06	0.0565	2.989	38.92
214	2.094	339	9.46	0.028	15.70	0.075	2.917	26.94
216	1.797	287	9.65	0.034	13.48	0.0639	3.037	35.46
217	2.313	339	12.87	0.038	17.35	0.0626	2.993	29.15
218	1.82	261	9.90	0.038	13.65	0.0633	3.027	32.22
219	2.289	326	13.59	0.042	17.17	0.0669	3.024	36.30
220	2.173	326	12.66	0.039	16.29	0.0628	2.962	39.08
221	3.04	352	18.23	0.052	22.80	0.0708	3.011	42.54
222	2.615	313	15.93	0.051	19.62	0.0691	3.011	43.31
225	2.032	287	12.38	0.043	15.24	0.0586	2.986	33.48
226	2.102	261	12.75	0.049	15.76	0.0665	3	37.55
227	1.761	287	10.73	0.037	13.21	0.0508	3.002	29.25
228	2.334	313	13.23	0.042	17.50	0.0692	2.989	32.96
230	1.878	261	10.50	0.04	14.09	0.0663	2.998	31.25
231	2.049	261	11.63	0.045	15.36	0.0729	3.026	36.63
232	1.337	261	6.53	0.025	10.03	0.0549	2.978	23.79
233	2.119	287	10.73	0.037	15.89	0.0727	2.913	24.95
234	2.845	365	16.28	0.045	21.34	0.0726	3.017	47.28
235	3.42	391	16.88	0.043	25.65	0.0942	2.915	45.94
236	2.981	417	16.32	0.039	22.36	0.065	3.024	40.07
262	2.897	365	16.17	0.044	21.73	0.0729	2.992	44.18

263	1.594	261	8.10	0.031	11.96	0.0603	2.986	23.08
264	1.376	248	6.77	0.027	10.32	0.0597	3.073	26.51
265	1.94	261	10.65	0.041	14.55	0.0678	3.035	30.47
267	2.174	300	13.02	0.043	16.30	0.0594	2.936	35.71
269	2.033	261	12.30	0.047	15.25	0.0643	2.995	38.12
270	2.235	287	13.53	0.047	16.76	0.0642	2.974	34.31
271	1.69	261	8.55	0.033	12.68	0.0638	3.021	32.72
272	1.792	287	8.66	0.03	13.44	0.0665	2.995	35.05
273	4.053	509	24.57	0.048	30.40	0.0658	3.011	61.12
274	4.359	509	26.33	0.052	32.70	0.0706	2.955	58.17
275	3.734	517	18.56	0.036	28.01	0.0783	3.023	47.88
276	2.059	287	11.72	0.041	15.44	0.0667	3.017	35.94
277	2.781	378	15.12	0.04	20.85	0.0666	2.942	40.81
278	3.024	417	16.68	0.04	22.68	0.0662	2.967	56.89
301	1.955	365	9.98	0.027	14.67	0.053	2.896	26.03
302	2.587	391	14.06	0.036	19.40	0.0599	3.023	35.69
304	3.306	443	16.07	0.036	24.80	0.0796	2.91	32.86
306	2.53	365	14.70	0.04	18.97	2.9584	2.958	54.27
308	1.985	287	11.96	0.042	14.89	0.0569	3.05	40.77
309	3.303	678	16.38	0.024	24.77	0.0527	2.882	41.44
310	3.789	678	23.40	0.035	28.42	0.0466	0.742	11.24
Average =	2.482	353	14.00	0.039	18.62	0.105	2.96	37.69

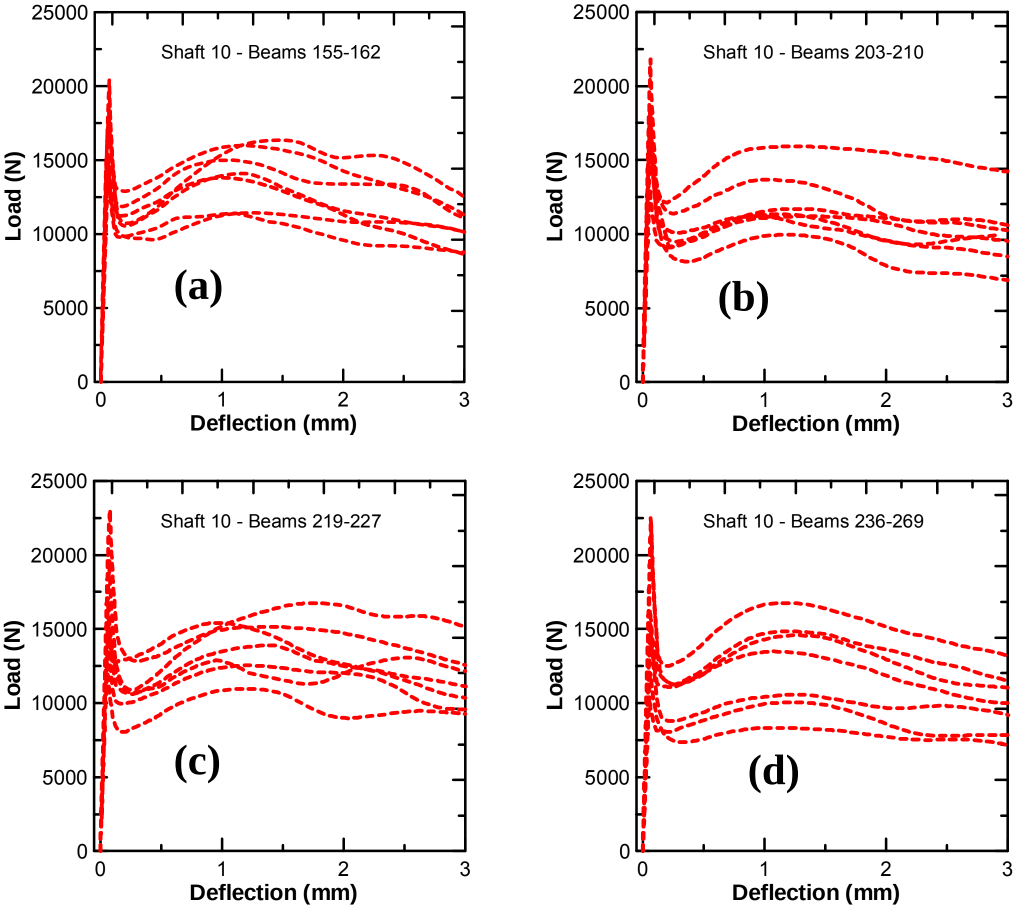

Figure 3.5.2 – Selected experimental load-deflection flexural response under four point bending condition for shotcrete.

This analysis provides a large number of key material parameters including; elastic flexural stiffness, deflection at maximum load, LVDT displacement at maximum load, maximum load, modulus of rupture (MOR), maximum deflection, maximum LVDT displacement and total flexural toughness. While these key parameters are extremely useful in providing elements for QA processes, the indirect calculation of the flexural toughness at the point of first cracking, post cracking transition point and point of maximum post crack loading provides a more complete picture of the sample’s behavior under loading conditions (see Table 3.5.1).

The point of first cracking is determined by the point at which the load-deflection curve deviates from its proportional elastic behavior. At this point tension cracks begin to form on the bottom of the sample, but the sample can still tolerate additional loading. Once failure occurs, the sample can no long take any further loading, as evidenced by the decreasing load-deflection curve in the post crack region defined by point A in Fig 3.5.1.

The transition point from post crack to a regeneration of load carrying capabilities is described as the post crack transition point and is shown by point B in Fig 3.5.1. At this point the sample exhibits renewed load bearing capabilities and an increase in loading is observed, while deflection continues. This regeneration of load bearing capability comes from the fibers bridging the crack in the failed cement matrix. The strain energy that would be going into propagating the failure cracks in the concrete is now channeled into pulling the fibers out of the concrete matrix, thus preventing a catastrophic failure. The load-deflection curve shows that there is a post crack maximum load when loading continues see point C in Fig 3.5.1. This post crack maximum provides information on how much loading a sample can withstand, even though there has been an initial failure of the sample. In some samples it has been observed that the post crack maximum load has been higher than the load at first cracking, and that establishes the fact that optimal fiber reinforcement has been achieved. Point D in Fig 3.5.1 shows the ultimate failure of the sample or the termination of the flexural test.

3.6 Results and Discussion for Early-Age Study

The development of early age properties is a dynamic process and due to activation and rapid strength gain of the samples, many parameters change quite rapidly, especially during the first 24 hours. For this purpose, the initial tests were conducted at 8 h, followed by 16 h and 36 h test results. Results of experimental analysis on three-point bending tests on different macro synthetic fibers are summarized in Table 3.6.1.

Table 3.6.1 – Summary of average experimental analysis for early age polymeric fibers

Sample ID	Age	Elastic Flexural Stiffness (kN/mm)	Deflection at Max Flexural Load (mm)	Maximum Flexural Load (kN)	Bending Strength (MPa)	Flexural Toughness (kN.mm)
P6-A-8h	8 h	151.6	0.048	5.10	1.42	8.08
P6-A-16h	16 h	264.7	0.043	9.69	2.70	12.58
P6-A-36h	36 h	260.8	0.053	11.38	3.17	15.09
P7-A-8h	8 h	221.1	0.048	7.32	2.04	10.65
P7-A-16h	16 h	279.2	0.053	10.06	2.81	13.16
P7-A-36h	36 h	349.8	0.038	11.13	3.10	13.63
P6-B-16h	16 h	250.4	0.043	8.00	2.23	9.43
P6-C-16h	16 h	270.9	0.043	10.01	2.79	7.73
P6-A&D-16h	16 h	210.9	0.046	8.71	2.43	8.84
P6-C&D-16h	16 h	245.1	0.056	8.45	2.36	10.74
P9-A-8h	8 h	267.5	0.033	6.80	1.90	10.93
P9-A-16h	16 h	271.1	0.051	9.89	2.76	12.07
P9-A-36h	36 h	319.8	0.053	11.69	3.26	14.29
G5-1d	1 d	104.0	0.041	3.70	2.81	1.45
G5-3d	3 d	125.2	0.041	4.42	3.36	1.45
G5-7d	7 d	135.5	0.041	4.55	3.45	1.37

Effect of age on flexural response of polymeric fiber type A is shown in Fig. 3.6.1a and 3.6.1b. Results show that the average elastic flexural stiffness of P6-A samples increases by 45% due to the strength gain and early hydration of the sample from 8 to 16 h, while there is no significant change in flexural stiffness of this mixture from 16 to 36 h. The deflection at maximum load for P6-A samples increases by 11 to 17% due to aging from 8 to 16 and 36 h. The toughness of P6-A samples increases by 80% from 8 to 16 h. However, from 16 to 36 h, the toughness increases only by 18%. The increases in maximum flexural load thus bending strength parameters from 8 to 16 h is from 1.42 to 2.70 MPa (+95%), while from 16 to 36 h only 0.47 MPa (+8%) increase is observed. In P9-A samples with 9 kg/m^3 of type A polymeric fibers, no significant change in elastic flexural stiffness is observed from 8 to 16 and 36 h. The deflection at maximum load increases by 50% from 8 to 16 h, but no significant change is observed from 16 to 36 h for P9-A samples. The total toughness from 8 to 16 h increases from 10.93 to 12.07 kN.mm (+28%) for P9-A samples; however, the toughness is slightly reduced by 3% from 16 to 36 h. While the increase in maximum flexural load and flexural strength parameters from 8 to 16 h is from 1.90 to 2.76 MPa (+55%) for P9-A samples, the increase is much lower from 16 to 36 h when only 7% increase were observed from the age of 16 h to 36 h. These results indicate that due to addition of accelerator admixtures, the early strength is mainly achieved during the first 16 h and then the gain in strength slows down significantly. It is concluded by comparing P6-A and P9-A samples that the gain in strength after 8 h in P-6 mixtures is much higher than P-9 mixtures. This is due to a very high dosage of accelerators resulting in an early high strength (before 8h) and gaining less strength afterward.

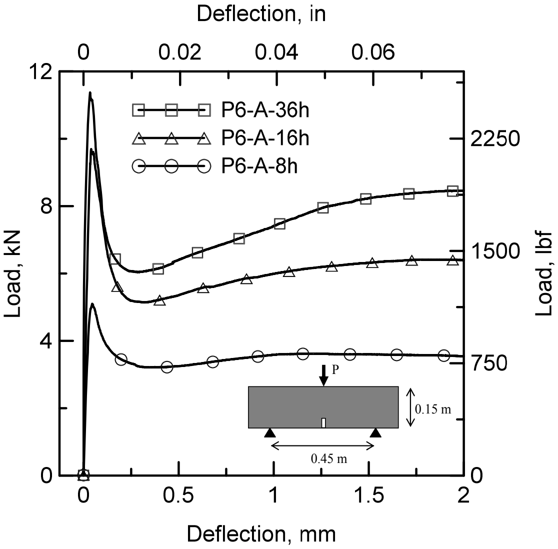

Fig. 3.6.1a. Effect of age on load deflection response for polymeric fiber type A with fiber content of 6 kg/m3

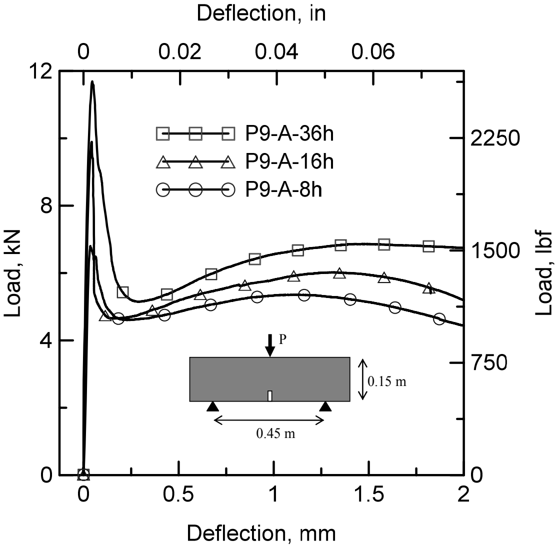

Fig 3.6.1b – Effect of age on load deflection response for polymeric fiber type A with fiber content of 8 kg/m3

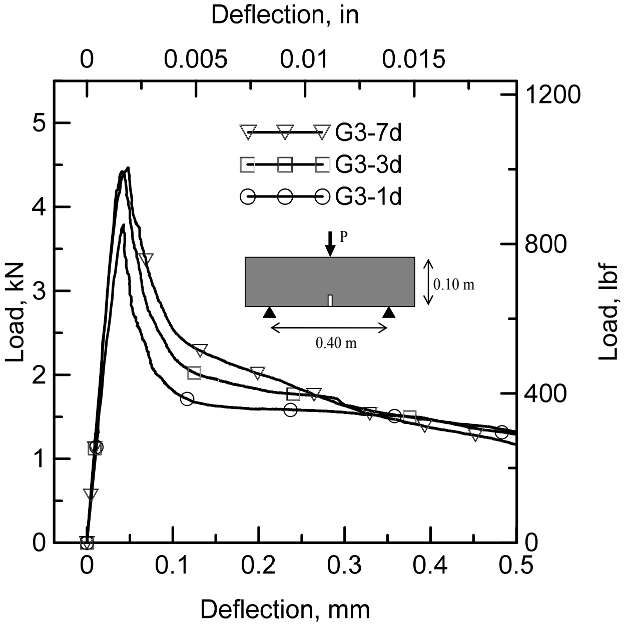

Fig. 3.6.1c – Load deflection responses of glass fibers at different ages.

Effect of age on flexural response of AR-glass fibers are shown in Fig. 3.6.1c. Results show that the age or duration of curing does not affect the deflections at maximum flexural load; however, maximum flexural load and thus flexural strength increases from 2.81 MPa to 3.36 MPa (+20%) from 1 to 3 days and from 3.36 to 3.45 MPa (+3%) from 3 to 7 days. The flexural toughness remains roughly constant at 3 and 7 days comparing to 1-day results due to higher residual strengths at the descending part of load-deflection curves.

Effect of polymeric fiber types at the age of 16 h are compared in Fig. 3.6.2. Results show that average flexural stiffness of P6-A-16h is 264.7 kN/m which is 5%, 20% and 7% higher than P6-B-16h, P6-A&D-16h and P6-C&D-16h, respectively and slightly lower than P6-C (%2). P6-A-16h along with P6-C-16 mixtures have the highest maximum flexural strength (~2.7 MPa) among all different fibers at 16 h. The flexural toughness of P6-A is 12.58 kN.mm which is

25%, 38%, 30% and 14% higher than P6-B, P6-C, P6-A&D and P6-C&D, respectively. It is clear that a one to one comparison of flexural toughness requires the development of a large scale database and scalar comparison of different samples on a relative basis. This type of comparison while quantitative in nature does not extend itself to development of design for various composites and needs to be developed for each fiber type, specimen size, and characteristic.

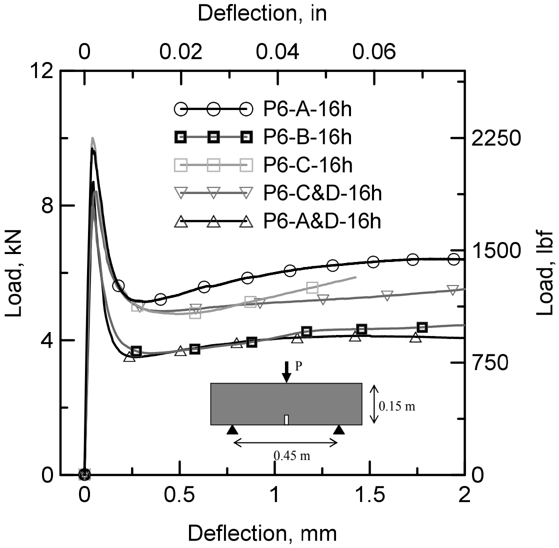

Fig. 3.6.2 – Load deflection responses for different polymeric fiber types.

A better way to correlate the toughness values is to establish a basis for the determination of load-deflection results which are inherently affected by the fiber type, loading and volume content and offer a rational way to correlate the measured flexural data with parameters that can directly be used in the design.

3.7 Inverse Analysis of Shotcrete Load-Deflection Response

Representative back-calculations of stress-strain responses by the described plasticity model for the Barchip fiber reinforced beams and simulated load deflection responses. Back-calculated tensile parameters of flexural samples using plasticity model are shown in Table 3.7.1

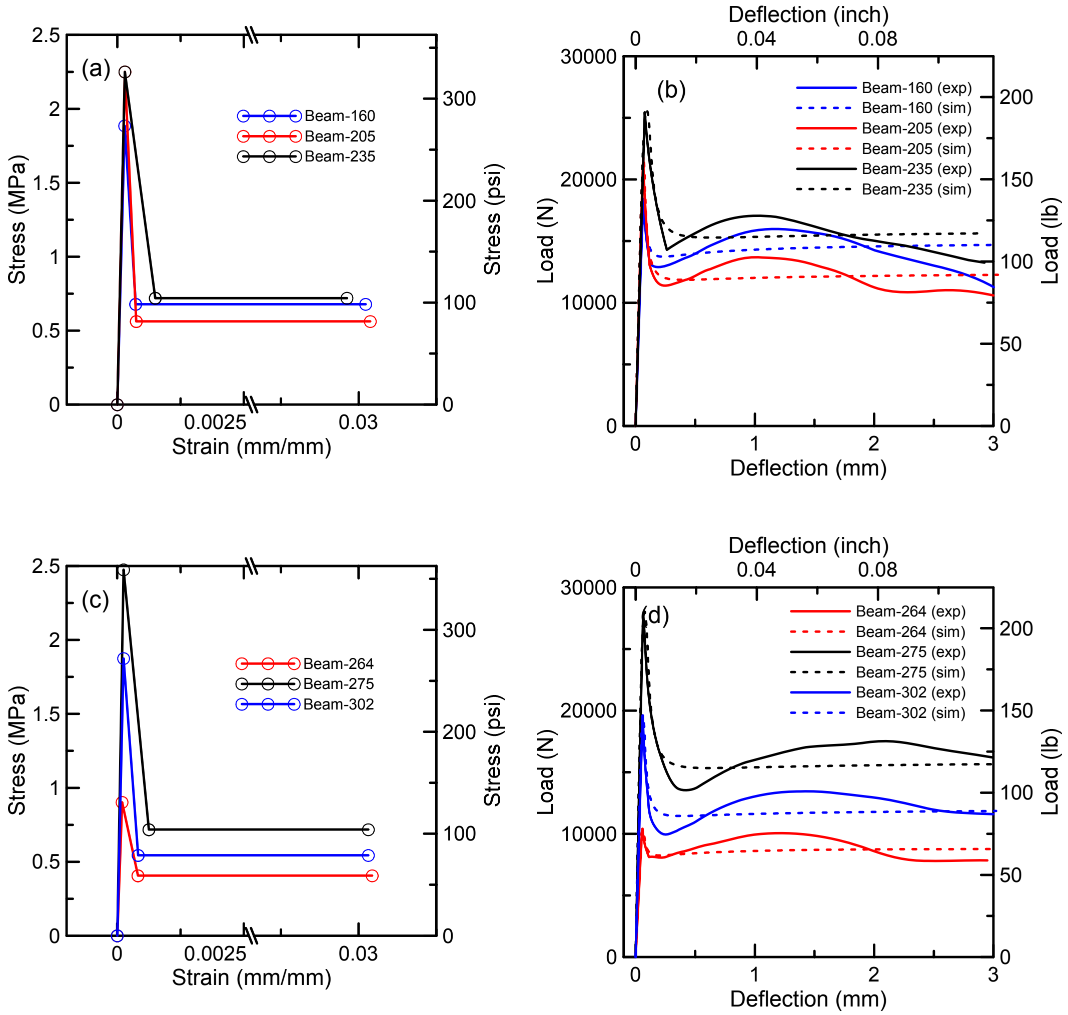

Figure 3.7.1 – Simulation and experimental flexural load deflection response and back calculated stress strain relationship for selected beam samples.

Table 3.7.1 – Back-calculated tensile parameters of flexural samples using Soranakom-Mobasher Model [33].

Beam ID	Tensile Toughness, (Gf) MPa	First Crack Tensile Stress, (σcr) Mpa	Normalized Post Crack Tensile Strength, (μ)	Normalized Transition Tensile Strain, (α)	Transition Tensile Strain, (εtrn) μstr	Ultimate Tensile Strain, (εtu) μstr	Residual Strength Parameter, (μσcr) MPa
155	0.0147	1.30	0.370	4	432	30240	0.480
156	0.0149	1.38	0.350	4	460	30475	0.483
157	0.0184	1.58	0.380	4	420	30450	0.599
158	0.0196	2.03	0.315	3	405	30375	0.638
160	0.0208	1.89	0.360	2.5	362.5	30450	0.679
161	0.0184	2.02	0.290	2.5	387.5	31155	0.584
162	0.0169	1.33	0.420	4.5	459	30090	0.557
164	0.0221	2.55	0.280	2	340	30600	0.714
168	0.0221	2.38	0.300	2	340	30600	0.714
169	0.0292	3.15	0.310	2	370	29600	0.975
170	0.0265	2.48	0.350	3	465	30225	0.868
171	0.0260	2.59	0.330	3	486	29970	0.855
192	0.0092	1.13	0.270	3	309	29870	0.306
194	0.0136	1.76	0.250	2	320	30400	0.440
195	0.0136	1.76	0.250	2	320	30400	0.440
196	0.0165	2.04	0.270	2	370	29600	0.549
198	0.0316	3.42	0.300	1.6	296	30525	1.027
199	0.0280	3.33	0.280	1.6	288	29700	0.932
200	0.0300	3.57	0.280	1.6	272	29750	1.000
201	0.0129	0.95	0.450	4.5	427.5	29925	0.428
202	0.0131	1.20	0.360	3	360	30000	0.432
203	0.0146	1.27	0.380	3	381	30099	0.483
204	0.0205	1.88	0.360	2.5	312.5	30125	0.675
205	0.0176	2.25	0.250	2.5	375	30750	0.563
207	0.0123	1.71	0.230	4	488	30500	0.393
208	0.0147	1.74	0.275	3	372	30380	0.477
209	0.0154	1.79	0.280	3	384	30336	0.502
210	0.0136	1.42	0.320	5	545	29430	0.453
211	0.0167	1.69	0.320	3	375	30625	0.540
212	0.0095	0.82	0.390	5	410	29520	0.320
213	0.0185	1.65	0.370	3	354	30090	0.611

214	0.0126	1.26	0.330	8	776	29585	0.416
216	0.0169	1.29	0.430	3	351	30420	0.553
217	0.0138	1.72	0.260	3	396	30360	0.446
218	0.0154	1.32	0.380	3	396	30360	0.502
219	0.0173	1.81	0.310	2.3	333.5	30450	0.562
220	0.0187	1.69	0.370	2.3	310.5	29700	0.624
221	0.0201	2.43	0.270	2.3	414	30240	0.656
222	0.0206	2.12	0.320	2	354	30090	0.680
225	0.0160	1.65	0.320	2	300	30000	0.528
226	0.0179	1.70	0.350	2	340	29920	0.595
227	0.0140	1.43	0.320	2	260	30290	0.458
228	0.0156	1.76	0.290	2.7	396.9	30135	0.512
230	0.0149	1.40	0.350	2.7	378	30100	0.490
231	0.0175	1.55	0.370	2.5	387.5	30225	0.574
232	0.0113	0.87	0.430	4.6	400.2	30015	0.374
233	0.0117	1.43	0.270	4.7	611	29510	0.386
234	0.0225	2.17	0.340	2.5	387.5	30225	0.738
235	0.0216	2.25	0.320	5	750	29250	0.720
236	0.0189	2.18	0.280	3.2	435.2	30600	0.609
262	0.0210	2.16	0.320	2.8	431.2	30030	0.690
263	0.0109	1.08	0.330	4.3	464.4	30240	0.356
264	0.0126	0.90	0.450	4.3	408.5	30875	0.406
265	0.0145	1.42	0.330	3	426	30530	0.469
267	0.0170	1.74	0.330	2.2	332.2	29445	0.573
269	0.0182	1.64	0.370	2	328	29848	0.607
270	0.0163	1.80	0.300	2.1	344.4	29848	0.541
271	0.0156	1.14	0.450	3.8	433.2	30210	0.513
272	0.0167	1.16	0.480	4.5	472.5	29925	0.554
273	0.0291	3.28	0.290	2.1	352.8	30240	0.950
274	0.0275	3.51	0.260	2.2	396	29700	0.913
275	0.0225	2.48	0.290	5	625	30625	0.718
276	0.0171	1.56	0.360	2.5	355	30246	0.562
277	0.0194	2.02	0.320	3.2	444.8	29607	0.645
278	0.0272	2.22	0.410	2.7	375.3	29607	0.912
301	0.0123	1.33	0.310	4.3	408.5	29450	0.412
302	0.0169	1.88	0.290	3.3	412.5	30625	0.544
304	0.0152	2.14	0.230	6	756	29610	0.493
306	0.0260	1.96	0.450	2	280	29400	0.882
308	0.0195	1.60	0.400	2	290	30450	0.638
309	0.0196	2.18	0.300	5	420	29400	0.655

310	0.0052	3.12	0.220	2	240	7200	0.686
Average =	0.0179	1.87	0.330	3.1	401	29789	0.595
Std Dev =	0.0053	0.64	0.059	1.20	103	2730	0.170

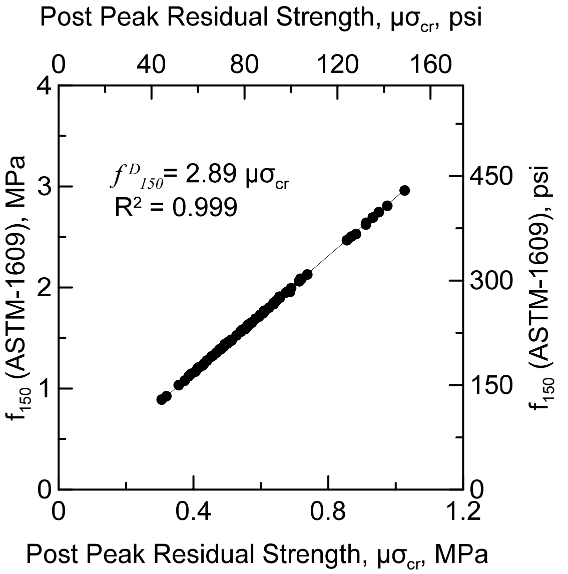

Figure 3.7.2 – Relationship of ASTM-C1609 residual strength parameter and model residual strength parameter $\mu\sigma_{cr}$.

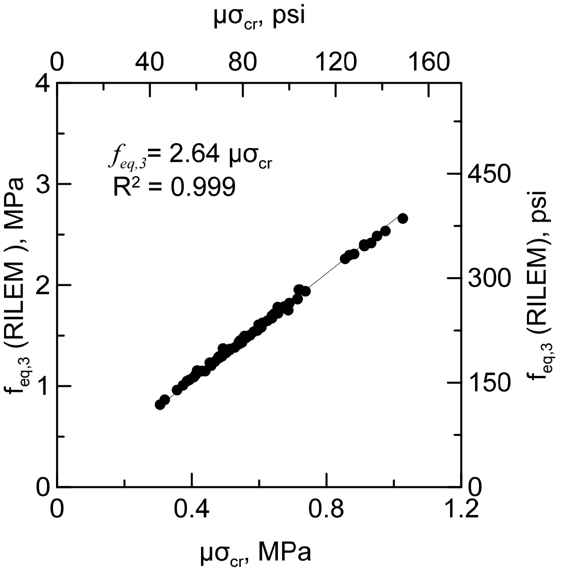

Figure 3.7.3 Relationship of RILEM residual strength parameter and model residual strength parameter $\mu\sigma_{cr}$.

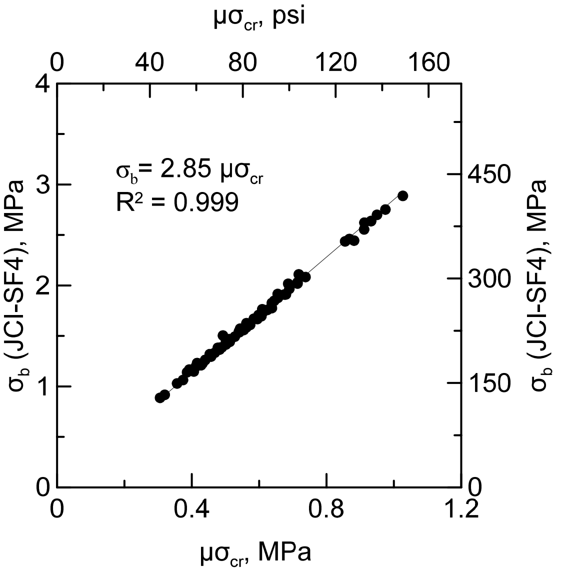

Figure 3.7.4 Relationship of JCI-SF4 residual strength parameter and model residual strength parameter $\mu\sigma_{cr}$

The development of the average residual strength (ARS) test is governed by the conditions from ASTM-C1609 to provide a practical method, both functionally and economically, for evaluating the performance of fiber-reinforced concrete (FRC) of any mixture design. In this case the ARS versus post peak residual strength is a useful parameter in design and quality control testing.

The results in Figure 3.7.2 show a correlation R^2 value of 0.960 which is conclusive for experimentally captured data. This indicates that post peak residual strength is a good predictor for ARS by applying the factor of 1/(2.89). The development of correction factors when compared with RILEM and JCI-SF4 residual parameters show factors of 1/(2.64) and 1/(2.85) respectively. A summary of the residual parameter relationship for the shotcrete analysis is shown in Table 3.7.2. Equation 3.7.1 shows the general form of the residual strength relationship, where k_{bt} is the linear parameter between the standards. Equations 3.7.2, 3.7.3 and 3.7.4 give the numerical equivalent using the correlated values for k_{bt} in each case.

$$\text{Residual Strength Parameter} = k_{bt}\mu\sigma_{cr} \tag{3.7.1}$$

Table 3.7.2 Residual strength parameter summary for shotcrete.

	Residual Parameter	k_{bt}
ASTM C1609	f^D_{150}	2.89
RILEM TC 162-TDF	$f_{eq,3}$	2.64
JCI-SF4	σ_b	2.85

$$f^D_{150} = 2.89\mu\sigma_{cr} \tag{3.7.2}$$

$$f_{eq,3} = 2.64\mu\sigma_{cr} \tag{3.7.3}$$

$$\sigma_b = 2.85\mu\sigma_{cr} \tag{3.7.4}$$

3.8 Inverse Analysis of Early-Age Load Deflection Response

The tensile response of a fiber reinforced concrete dominates the performance under many loading conditions and applications. To understand this response, a back-calculation process where the material properties can be determined is employed. This procedure is performed by model fitting of the experimental three-point bending load deflection data on four types of macro synthetic polymeric fibers and one type of Alkali Resistant (AR) glass fiber conducted in an earlier section. Results of back-calculation of stress-strain responses by tri-linear tensile model for all mixtures are shown in Table 3.8.1.

Table 3.8.1. Average back calculated tensile parameters for early age FRC.

Sample ID	Age	Young's Modulus (E), GPa	First Crack Tensile Strength (σ_{cr}), MPa	Normalized Post Crack Tensile Strength (μ)	Normalized Transition Tesnile Strain (α)	Transitional Tensile Strain (ε_{trn}), μstr	Ultimate Tensile Strain (ε_{tu}), mm/mm
P6-A-8h	8 h	19.65	0.63	0.52	89	2848	0.099
P6-A-16h	16 h	24.13	1.25	0.44	50	2600	0.092
P6-A-36h	36 h	32.41	1.46	0.46	50	2250	0.090
P7-A-8h	8 h	22.06	0.93	0.47	58	2436	0.101
P7-A-16h	16 h	33.10	1.29	0.41	58	2262	0.994
P7-A-36h	36 h	37.23	1.45	0.39	42	1638	0.975
P6-A-16h	16 h	24.13	1.25	0.32	45	2340	0.038
P6-B-16h	16 h	20.68	1.05	0.36	45	2295	0.097
P6-C-16h	16 h	22.75	1.31	0.37	47	2703	0.063
P6-AD-16h	16 h	20.68	1.16	0.32	45	2520	0.095
P6-CD-16h	16 h	20.68	1.08	0.46	62	3224	0.104
P9-A-8h	8 h	22.06	0.84	0.56	60	2280	0.095
P9-A-16h	16 h	31.03	1.30	0.39	38	1596	0.097
P9-A-36h	36 h	29.30	1.55	0.38	42	2226	0.095
G3-1d	1 d	27.23	1.50	0.29	20	1100	0.041

G3-3d	3 d	32.75	1.67	0.27	27	1377	0.016
G3-7d	7 d	32.75	1.70	0.25	35	1820	0.026

3.8.1 Effect of age on back-calculated tensile stress-strain response

Fig. 3.8.1 represents effect of age on the back calculated tensile stress-stain response and flexural load-deflection response of the type A macro synthetic fibers. As shown in Fig. 3.8.1a, the initial response is linear elastic up to about 0.6, 1.2 and 1.6 MPa for 8, 16 and 36 h samples as the first crack stage. After cracking, the load is transferred to the fibers bridging the cracks resulting in the significant drop in the stiffness of samples by increasing the crack width. Back-calculated tensile stress-strain responses show that after an average strain level of about 0.0025 mm/mm, the residual strength of the macro synthetic fiber composites reaches a constant value. The post-crack residual strength at this plateau zone increases from about 0.35 to 0.55 and 0.7 MPa due to aging from 8 to 16 and 36 h. A typical maximum curvature-deflection relationship is also demonstrated in Fig. 3.8.1a and represents a linear response. As shown in Fig. 3.8.1b, the simulation for load-deflection response shows a very good correlation with the experimental data.

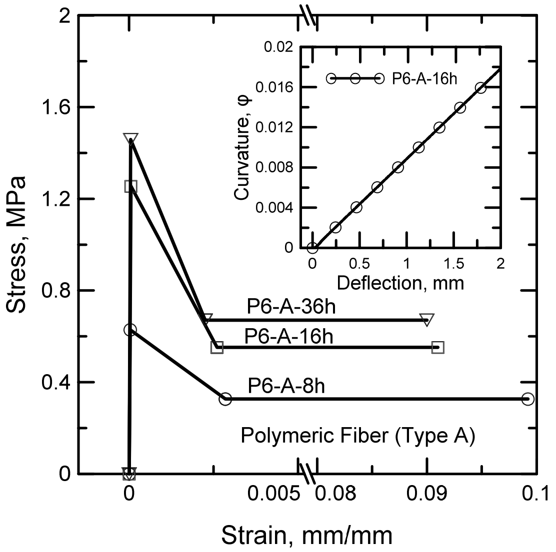

Fig 3.8.1a. Effect of age on back calculated tensile stress strain response, and a representative curvature-deflection relationship.

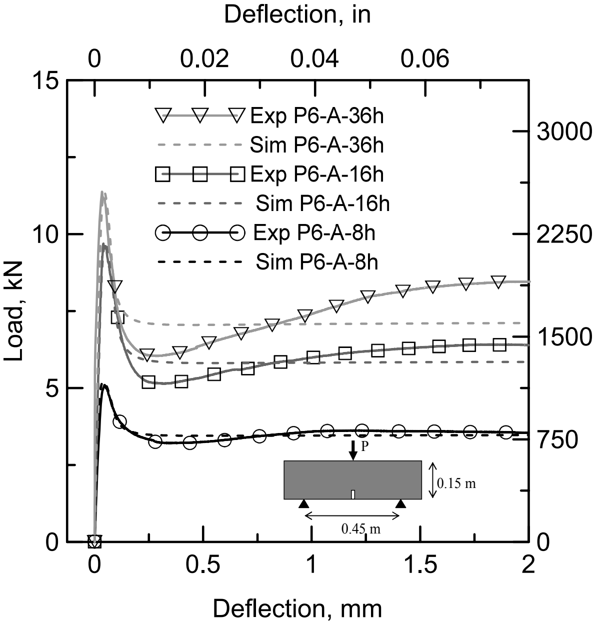

Figure 3.8.1b. Effect of age on experimental and simulated load deflection response for polymeric fibers.

Effect of age on back calculated tensile stress-strain response and experimental and simulated load-deflection response for FRC with AR-Glass fibers are shown in Fig. 3.8.2. The tensile strength of the glass fiber campsites are not affected significantly by the age, as the tensile strength increases from about 1.5 to 1.7 MPa by increasing the age from 1 to 3 days. The back-calculated tensile strength at 7 days is the same as its value in 3 days. Furthermore, the residual tensile strength at the plateau zone for all different ages of glass fibers are the same and about 0.4 MPa. The only difference among AR-glass samples at different ages are the slope of descending part which decreases with age. This also indicates that the glass fibers are able to generate the bond quite efficiently during the first 24 h and maintain it during the first initial 7 days. The simulated load-deflection responses show good agreements with the experimental data; however, the advanced part of load-deflection response is not fitted well with the assumed plateau response. This may be attributed to fracture of the glass fibers in this range and reduction of the bridging fiber contents at large scale crack opening.

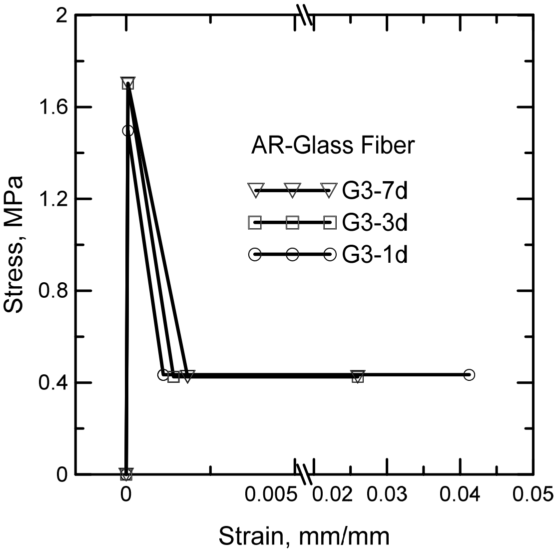

Figure 3.8.2a. Effect of age on back calculated tensile stress strain response.

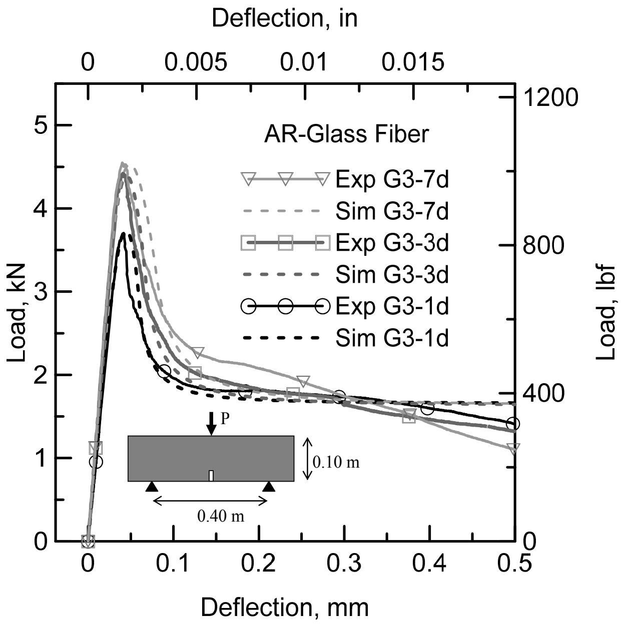

Figure 3.8.2b Effect of age on experimental and simulated load deflection response for glass fibers.

3.8.2 Effect of fiber type on back-calculated tensile stress-strain response

Effect of macro synthetic fiber types on back calculated tensile stress-strain response and experimental and simulated load-deflection responses are shown in Fig. 3.2.3. The tensile strength of the macro synthetic reinforced campsites is within 1.1-1.4 MPa at the age of 16 h. The post- cracking modulus, E_{cr} for simulation of descending part in strain softening composites is virtually the same for all different fiber types. However, the residual tensile strengths at the plateau zone are different, as P6-B mixture has the residual strength of about 0.55 MPa compared to 0.5 MPa and 0.4 MPa for P6-C and P6-A mixtures. As shown in Fig. 3.8.3b, the simulated load-deflection response shows a good correlation with the experimental data. The effect of fiber types on the load-curvature relationship is shown in Fig. 3.8.4 and indicates a major perspective that the curvature of the beam at the moment of peak strength and even at displacement corresponding to two to three times the deflection at peak is quite low. The curvatures at these points correspond to magnitudes as high as 0.0009, 00.0017 and 0.0026. The consequences of this observation is that when the size of the beam increases to structural levels used for design, such curvature levels are still dominant and therefore the measurements of deflection, and hence toughness using load deflection responses that extend into crack opening of 1-2 mm are inconsequential to the performance of the composite in real scale structures.

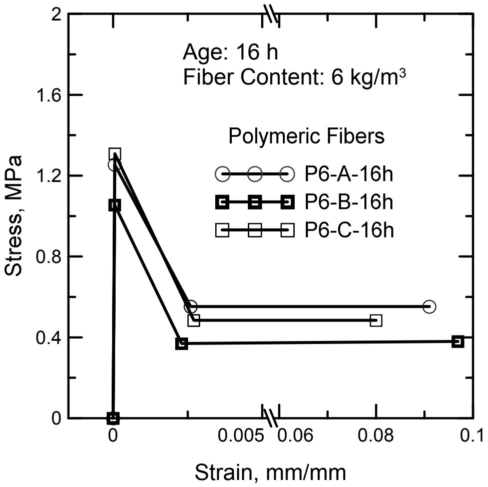

Figure 3.8.3a. Effect of fiber type back calculated tensile stress strain response

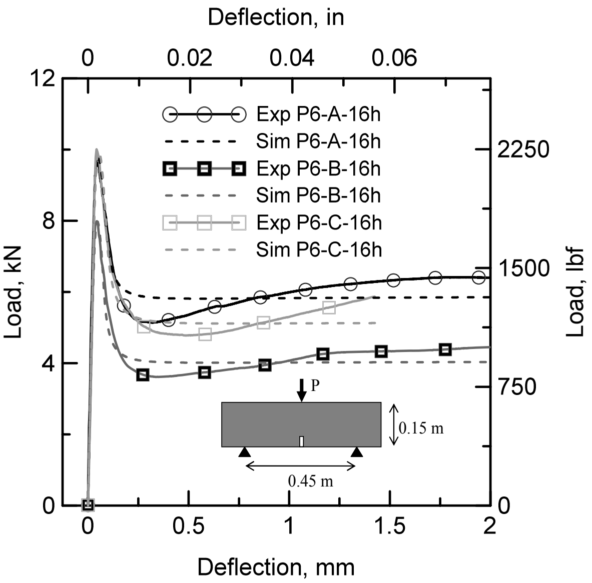

Figure 3.8.3b. Effect of fiber type on experimental and simulated load deflection response for polymeric fibers.

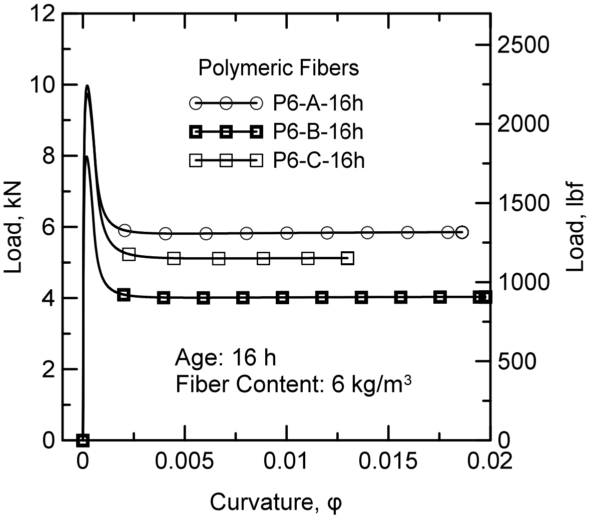

Figure 3.8.4. Relationship between load and curvature for samples with different macro synthetic fibers.

3.9 Residual Strength in Comparison with Back-Calculated Residual Strength

The comparison of residual strength and presentation of correction factors to current ASTM, JCI and RILEM residual strength parameters are presented from an early age FRC study [36] as a means of correlation and validation of the current data analysis.

3.9.1. Residual Strength by ASTM C 1609 ($\boldsymbol{f_{150}^{D}}$)

Under the assumption that the results of these experiments which contain a notch and are conducted in three point bending can be similar to results obtained from un-notched specimens under four point bending, one can apply the same equations for reducing of the data in accordance to ASTM approach. As shown in Fig. 3.9.1, ASTM C 1609 method overestimates the residual uniaxial tensile strength defined under the present approach as $\mu E \varepsilon_{cr}$. A plot of corresponding values from two tests reflects a factor of almost three times. Therefore, it is imperative to note that the f_{150}^{D} parameter can be used as a tensile stress measure associated with the post crack tensile strength parameter σ_{cst} in Fig. 2.1.1b, so long as the Average Residual Strength (ARS) values are corrected by a scale factor of 1/(2.95).

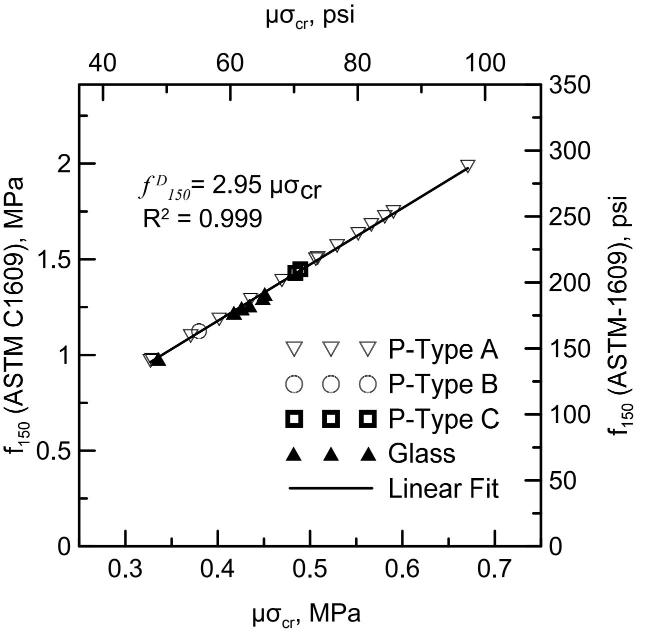

Figure 3.9.1 Comparison of residual strength ($\mu\sigma_{cr}$) with ASTM-1609 residual parameter

3.9.2 Residual Strength by JCI-SF4 ($\boldsymbol{\sigma_b}$)

As shown in Fig. 3.9.2, direct correlation of JCI residual strength and the present method indicate JCI-SF4 method overestimates the residual uniaxial tensile strength $\mu E \varepsilon_{cr}$ by as much as three times as well. The correction factor for the JCA method is 1/(3.08).

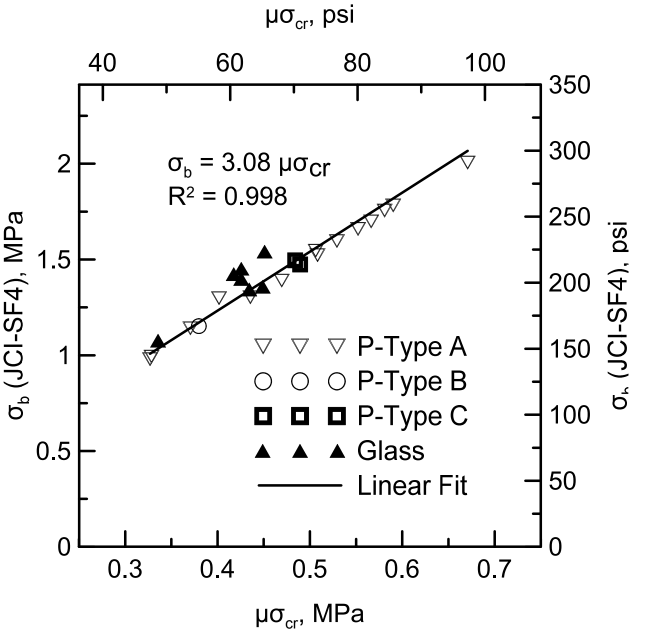

Figure 3.9.2.Comparison of residual strength ($\mu\sigma_{cr}$) with JCI-SF4 residual parameter

3.9.3. Residual Strength by RILEM TC 162-TDF ($f_{eq,3}$)

Similar to other test methods, direct correlation of RILEM residual strength and the present method indicates that RILEM method overestimates the residual uniaxial tensile strength $\mu E\varepsilon_{cr}$ by as much as three times. These results show that the standard residual flexural strength parameters can be correlated to the tensile strength by a coefficient factor of 1/(3.11). This value is in accordance with the draft of ACI 544.3R report based on the stress coefficients values adopted by Barros 2004 [38] who presented a linear relationship between tensile stress at very advanced levels of strains and flexural strength using a coefficient factor of 0.27.

$$\sigma_3 = 0.27 f_{R\_4} \qquad (3.9.1)$$

It is noted that in the proposed methods for design by fib [39], a correction factor of 1/3 is used for scaling the parameter f_{R3} from flexural tests to obtain f_{Ftu} which represents the ultimate residual strength. This correction factor was obtained by calibration of various specimen sizes, and various fiber types and dosages. The proposed value and the present calculation therefore correlate quite well. The present approach can be used as theoretical justification for the empirical values obtained and used in the FIB model code.

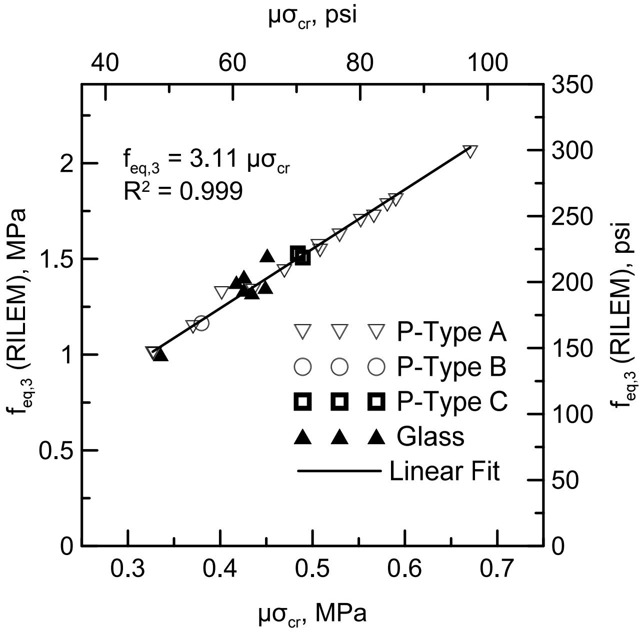

Figure 3.9.3 Comparison of residual strength (μσcr) with RILEM residual parameter for macro synthetic fibers.

Table 3.9.1 Residual strength parameter summary for early age study.

	Residual Parameter	k_{bt}
ASTM C1609	f^D_{150}	2.95
RILEM TC 162-TDF	$f_{eq,3}$	3.11
JCI-SF4	σ_b	3.08

$$f^D_{150} = 2.95\mu\sigma_{cr} \tag{3.9.2}$$

$$f_{eq,3} = 3.11\mu\sigma_{cr} \tag{3.9.3}$$

$$\sigma_b = 3.08\mu\sigma_{cr} \tag{3.9.4}$$

Table 3.9.1 and equations 3.9.2, 3.9.3 and 3.9.4 summarize the residual strength relationship for the early age study with the linear coefficient k_{bt} for each case.

3.8 Conclusions

Characterization of tensile-flexural strain softening and strain hardening of fiber cement composites in early age shows that the presence of fiber significantly increases the ductility of the material. By applying the load deflection back-calculation technique one can generate strength data with a higher degree of accuracy than the current standard methods. Using a closed form set of governing parameters and variables applied through each stage of material response, the stress distribution that considers a shifting neutral axis can be simulated which provides a more accurate representation of the residual strength and toughness of FRS.

Since the inherent assumption of the available standard method assumes that the neutral axis is still at the centroid of the specimen, and the stress distribution is linear throughout. This leads to very high nominal flexural stress levels in tension fiber which are far more than tensile strength. Extreme caution must be exercised in application of the ASTM 1609, JCI-SF4 and RILEM TC 162-TDF methods in design and analysis of fiber reinforced concrete sections, as the results show overestimation of the residual parameter by as much as 2.95-3.11 times. While these experiments were primarily addressing early age toughness parameters, it is expected that the same approach is also applicable to FRC materials that undergo ordinary curing processes and the same correlation parameters can be obtained for specimens prepared under lower levels of accelerating admixtures.

Chapter 4

POST-CRACKING CHARACTERIZATION OF STEEL AND SYNTHETIC FIBER REINFORCED CONCRETE USING THE STRAIN SOFTENING MODEL

4.1 Testing Program

Addition of synthetic structural fiber to plain concrete beams has shown similar equivalent flexural strength values to steel fiber reinforced concrete [40]. In addition, the scatter of experimental results of concrete beams in the post-peak region is much smaller for synthetic fibers than steel fibers due to the higher number and the more homogeneous distribution of the synthetic fibers over the fracture surface [28]. Therefore two types of steel fibers, three types of synthetic fibers including two different types of polymeric fibers and one type of AR-glass fiber are used to study post-peak response of 28 day standard curing FRC. Physical and mechanical properties of the fibers used in the test program are presented in Table 4.1.1.

Table 4.1.1. Properties of fibers used in study.

Fiber Type	Steel (S)	Steel (S)	P – Type A	P-Type B	Glass (G)
Base	Hooked (H)	Twisted (T)	Monofilament Polypropylene/ Polyethylene blend	Modified Olefin	Alkalai Resistant Glass
Length (mm)	30	30	50	50	6, 12, 24
Density (g/cc)	7.9	7.9	0.92	0.92	2.7
Tensile Strength (Mpa)	2300	2760	600-650	552	1724
Elastic Modulus (Mpa)	200	200	5	10	69

Polymeric fibers have two different polymeric bases including modified Polypropylene, Polyethylene and Olefin blends. Mixture proportions of twelve different mixtures prepared and tested under three-point bending configuration are shown in the Table 4.1.2. The first letter on the samples' labels refers to the general type of fiber used, i.e. P in case of polymeric, G in case of glass fiber and S in case of steel fiber. The following number is the dosage of the fiber presented in kg/m^3 and for polymeric fiber another letter follows this number referring to the type of polymeric fibers shown in Table 4.1.1. The final number in the labels shows the age of samples. Steel fibers have either hooked ends or are longitudinally twisted, the designation of H and T are given respectively

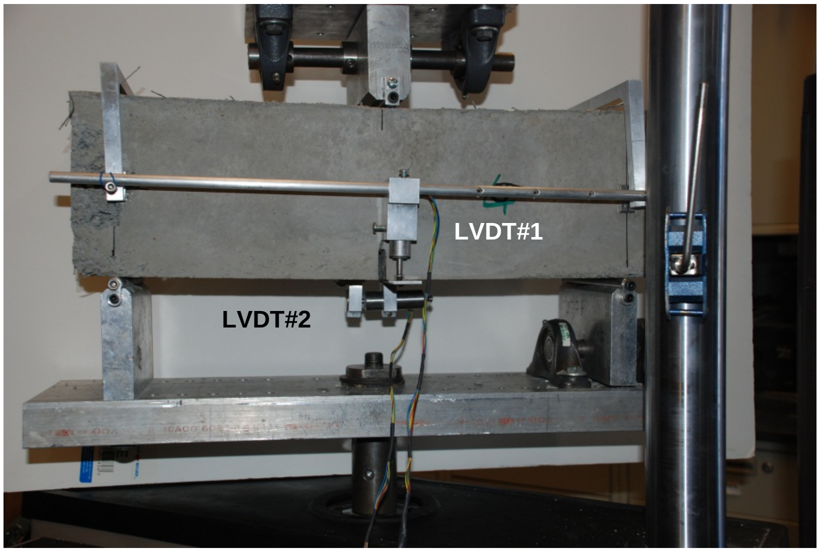

Figure 4.1.1. Test setup for three-point bend flexural test (ASTM C-1399).

In order to monitor post-peak flexural response of concrete samples using closed loop testing, samples were pre-notched and load was applied along the notch. Similar to RILEM TC 162-TDF recommendation [4], beams were loaded at a single point in the mid-span also known as the three-point bending test. Polymeric-FRC sample dimensions were 0.53m x 0.15m x 0.15m with an initial notch length of 25 mm, and test span of 0.45 m. Dimensions of AR glass-FRC samples were 0.45m x 0.1m x 0.1m with an initial notch length of 12 mm and test span of 0.40 m, respectively. Steel-FRC samples were tested under ASTM C-1609 (Four-Point Bend tests), sample sizes were either 0.30m x 0.10m x 0.10m or 0.45m x 0.15m x 0.15m and indicated my M (medium) or L (large) size samples respectively. A notch is not required for C1609 tests. Tests were performed under closed loop control with Crack Mouth Opening Deformation (CMOD) as the controlled variable. Fig. 4.1.1 shows a typical concrete beam under a closed-loop three-point bending test setup. The CMOD was measured across the face of notch using a Linear Variable Differential Transformer (LVDT) with a working range of 2.5 mm. Closed loop control tests were conducted with a CMOD rate of 0.12 mm/min up to a CMOD level of 3 mm. The deflection of the beam at the mid-span was measured using another LVDT. It is observed that cracks initiate from the notch and extend up to the upper side of the beam; however, the crack is bridged by the fibers which are being pulled under this loading. The presence of fiber significantly increases the ductility of the material and makes the crack opening and deflection exceed 1.2 mm. The load deflection curve is characterized by the maximum load and its associated deflection, elastic stiffness, maximum flexural strength and flexural toughness, and residual strengths by ASTM C 1609 (f_{150}^{D}), JCI-SF4 (σ_b) and RILEM TC 162-TDF ($f_{eq,3}$).

4.1.2 Effect of Curing and Fiber Types on Strength and Flexural Toughness

The development of extended age properties is a dynamic process and due to activation and strength gain of the samples, many parameters change quite rapidly, but the 28 day strength is when the industry typically takes concrete strength. For this purpose, the initial tests were conducted at 14 days, followed by 28 day results. Results of experimental analysis on three-point and four-point bending tests on different macro synthetic and steel fibers are summarized in Table 4.1.3.

Table 4.1.3 – Summary of average experimental analysis for early age polymeric fibers

Sample ID	Age, days	b (mm)	d (mm)	L (mm)	Elastic Flexural Stiffness (kN/mm)	Defl @ Max Flex Load (mm)	Max Flex Load (kN)	Bending Strength (MPa)	Flexural Toughness (kN.mm)
P3-A-14d	14	152	127	450	149	0.067	5.63	1.57	2.06
P3-A-28d	28	152	127	450	180	0.069	6.89	1.92	4.35
P3-B-14d	14	152	127	450	149	0.068	5.17	1.44	2.19
P3-B-28d	28	152	127	450	189	0.059	6.08	1.7	4.28
G6-6-28d	28	102	89	400	249	0.05	7.73	5.87	1.33
G6-12-28d	28	102	89	400	249	0.048	7.63	5.79	1.05
G6-25-28d	28	102	89	400	249	0.05	8.56	6.5	0.95
S22-HL-28d	28	152	152	450	822	0.043	23.34	3.01	32.27
S22-HL-56d	56	152	152	450	822	0.042	21.18	2.74	31.36
S44-HL-28d	28	152	152	450	822	0.054	26.07	3.1	46.21
S44-HL-56d	56	152	152	450	731	0.052	24.93	3.22	77.98
S66-HL-28d	28	152	152	450	548	0.082	25.07	3.24	122.60
S66-HL-56d	56	152	152	450	548	0.08	22.23	2.87	109.37
S133-HM-28d	28	102	102	300	348	0.538	39.92	11.98	103.64
S133-TM-28d	28	102	102	300	348	0.689	57.16	17.15	175.41
S133-HL-28d	28	152	152	450	522	0.65	86.98	11.6	300.70
S133-TL-28d	28	152	152	450	522	0.773	97.82	13.04	378.60

Effect of curing time on flexural response of polymeric fiber type A and B is shown in Fig. 4.1.2a Results show that the average elastic flexural stiffness of P3-A samples increases by 30% due to the strength gain and cement hydration of the sample from 14 to 28 days. The deflection at maximum load for P3-A samples increases by 11 to 17% due to aging from 14 days to 28days. The toughness of P3-A samples increased by over 100% from 14 to 28 days. The increases in maximum flexural load thus bending strength parameters from 14 to 28 days is from 1.57 to 1.92 MPa (+22%),. In P3-B samples with 3 kg/m^3 of type B polymeric fibers, no significant change in elastic flexural stiffness is observed from when compared to samples with fiber type A. The deflection at maximum load increases by 17% from 14 to 28 days. The total toughness from 14 to 28 days increases from 2.2 to 4.3 kN.mm (+95%) for P3-B samples. While the increase in maximum flexural load and flexural strength parameters from 14 to 28 days is from 1.44 to 1.70 MPa (+18%) for P3-B samples. Both mixes for P3-A and P3-B contained 4% accelerator and the effects between fiber types is minimal. But strength gain and toughness increases greatly from 14 to 28 days.

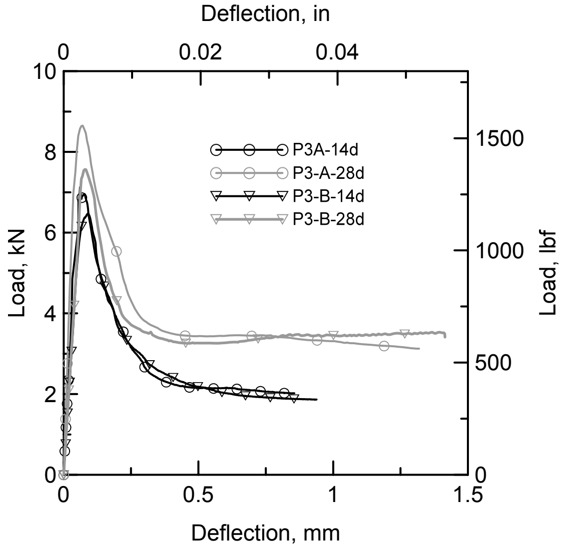

Figure 4.1.2a – Effect of curing time on load deflection response for polymeric fiber type A and B with fiber content of 3 kg/m^3

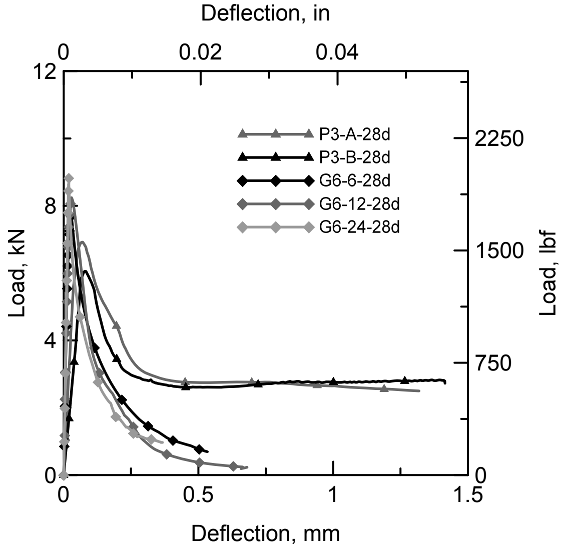

Figure 4.1.2b – Effect of fiber type on load deflection response for glass and polymeric fibers at an age of 28 days.

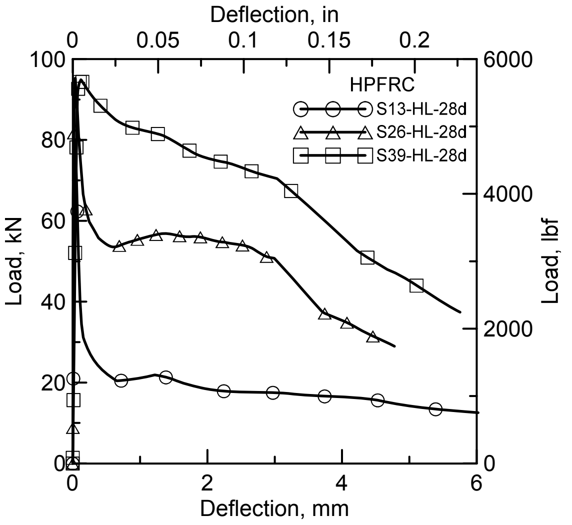

Figure 4.1.2c – Effect of fiber dosage on load deflection response for hooked steel fibers with large (150x150x450mm) sample size at 28 days.

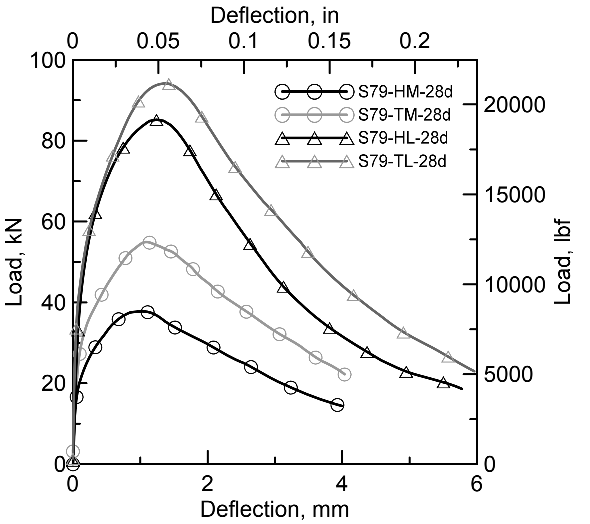

Figure 4.1.2d- Effect of sample size and fiber geometry on load deflection response for samples at 28 days.

Effect of fiber length at 28 days on flexural response of AR-glass fibers are shown in Fig. 4.1.2b. Results show that the fiber length does not affect the deflections at maximum flexural load; however, maximum flexural load and thus flexural strength increases from 5.79 MPa to 6.50 MPa (+12%) from 12mm to 25mm at 28 days. The flexural toughness is showing a decreasing trend with increasing fiber length.

4.2 Analysis – Prediction of Load-Deflection Response of Fiber Cement Composites

The tensile response of a fiber reinforced concrete dominates the performance under many loading conditions and applications. To understand this response, a back-calculation process where the material properties can be determined is employed. This procedure is performed by model fitting of the experimental three-point and four-point bending load deflection data on two types of macro synthetic polymeric fibers, two types of steel fibers and one type of Alkali Resistant (AR) glass fiber. Results of back-calculation of stress-strain responses by tri-linear tensile model for all mixtures are shown in Table 4.2.1.

Table 4.2.1. Average back calculated tensile parameters for FRC.

Sample ID	Age, days	Young's Modulus (E) Mpa	First Crack Tensile Strength (σcr) Mpa	Normalized Post Crack Tensile Strength (μ)	Normalized Transition Tesnile Strain (α)	Transitional Tensile Strain (εtrn), μstr	Ultimate Tensile Strain (εtu), mm/mm	Tensile Toughness, (Gf) Mpa
P3-A-14d	14	11376	0.71	0.22	92	5704	0.037	0.607
P3-A-28d	28	13790	0.85	0.3	92	5704	0.058	1.290
P3-B-14d	14	11376	0.63	0.23	135	7425	0.041	0.646
P3-B-28d	28	14479	0.75	0.34	90	4680	0.061	1.263
G6-6-28d	28	58605	2.81	0.11	55	2640	0.018	0.836
G6-12-28d	28	58605	2.81	0.05	52	2496	0.021	0.772
G6-25-28d	28	58605	3.28	0.06	37	2072	0.012	0.588
S13-HL-28d	28	31026	1.89	0.12	8	488	0.061	7.931
S13-HL-56d	56	31026	1.68	0.15	9	486	0.054	7.708
S26-HL-28d	28	31026	1.95	0.33	10	630	0.032	11.351
S26-HL-56d	56	27579	1.99	0.22	8	576	0.079	19.171
S39-HL-28d	28	20684	1.84	0.42	10	890	0.071	30.140
S39-HL-56d	56	20684	1.57	0.41	13	988	0.076	36.001
S79-HM-28d	28	20000	5.2	0.2	140	36400	0.061	0.0532
S79-TM-28d	28	20000	7.6	0.2	110	41800	0.062	0.0916
S79-HL-28d	28	20000	5.2	0.13	105	27300	0.061	0.0378
S79-TL-28d	28	20000	5.8	0.13	115	33350	0.062	0.0439

4.2.1 Effect of Curing Time on Back-Calculated Tensile Stress-Strain Response

Fig. 4.2.1 represents effect of curing time on the back calculated tensile stress-stain response and flexural load-deflection response of the type A and B macro synthetic fibers. As shown in Fig. 4.2.1a, the initial response is linear elastic up to about 1.4 MPa for 14 day samples as the first crack stage. After cracking, the load is transferred to the fibers bridging the cracks resulting in the significant drop in the stiffness of samples by increasing the crack width. Back-calculated tensile stress-strain responses show that after an average strain level of about 0.0025 mm/mm, the residual strength of the macro synthetic fiber composites reaches a constant value. The post-crack residual strength at this plateau zone increases from about 0.35 to 0.55 MPa due to aging from 14 to 28 days. As shown in Fig. 4.2.1b, the simulation for load-deflection response shows a very good correlation with the experimental data.

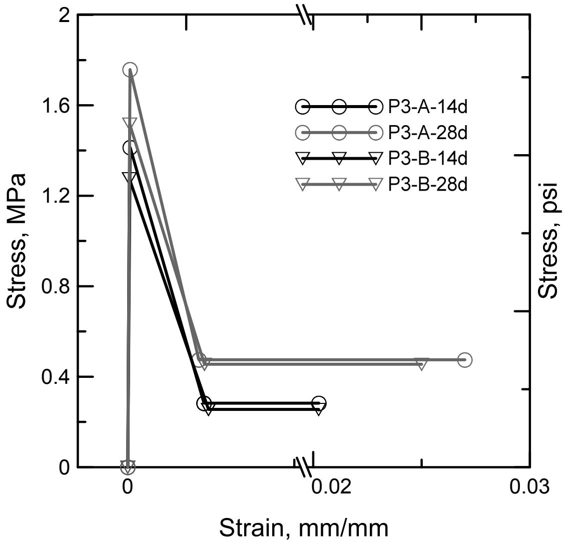

Fig 4.2.1a. Effect of curing time on back calculated tensile stress strain response

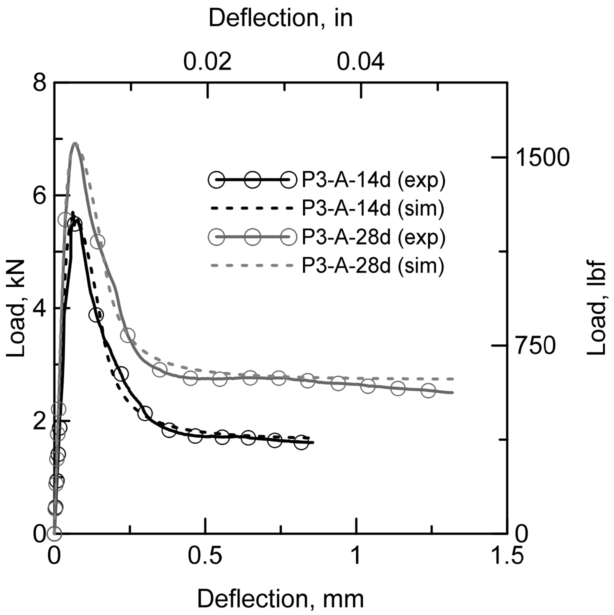

Figure 4.2.1b. Effect of curing time on experimental and simulated load deflection response for polymeric fibers.

Effect of fiber length on back calculated tensile stress-strain response and experimental and simulated load-deflection response for FRC with AR-Glass fibers are shown in Fig. 4.2.2. The tensile strength of the glass fiber campsites are not affected significantly by the length of fiber, as the tensile strength increases from about 2.81 to 3.28 MPa by increasing the length from 12mm to 25mm. The back-calculated tensile strength for glass fibers at 28 days is much more than polymeric fibers at 28 days (+300%). Furthermore, the residual tensile strength at the plateau zone for all different ages of glass fibers are the same and about 0.15 MPa. The simulated load-deflection responses show good agreements with the experimental data; however, the advanced part of load-deflection response is not fitted well with the assumed plateau response. This may be attributed to fracture of the glass fibers in this range and reduction of the bridging fiber contents at large scale crack opening.

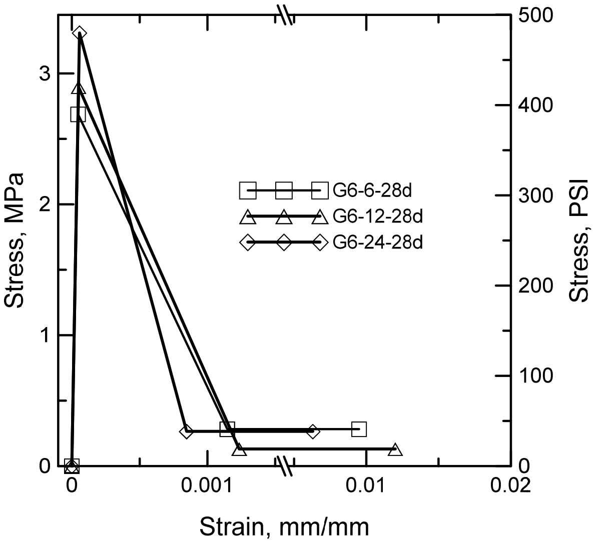

Figure 4.2.2a. Effect of curing time on back calculated tensile stress strain response

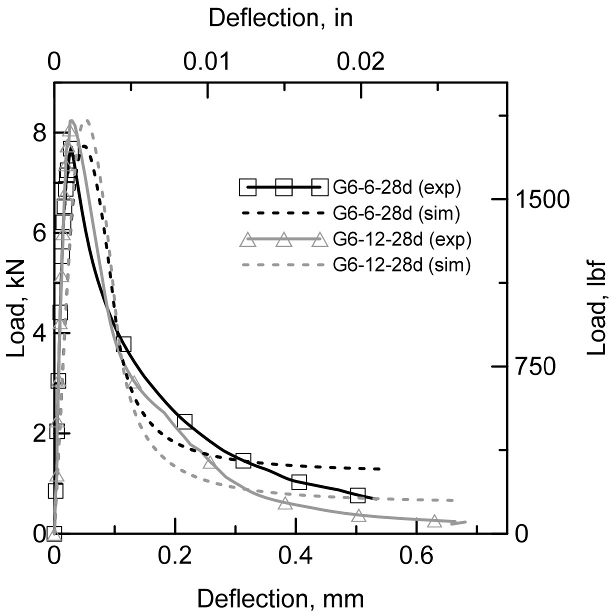

Figure 4.2.2b Effect of curing time on experimental and simulated load deflection response for glass fibers.

4.2.2 Effect of Fiber Type on Back-Calculated Tensile Stress-Strain Response

Two sets of steel fibers were evaluated. One set used dosages of 13, 26 and 39 kg/m^3 (H fiber deformation type) in high performance concrete (HPFRC) and fixed sample geometry (L). The another set had a fixed dosage of 79 kg/m^3 of two different steel deformation fiber types (H and T) and two different sample sizes (M and L) in ultra high performance concrete (UHPFRC).

At 28 days the HPFRC showed increases in flexural toughness as fiber dosage increased. This is evidenced by the back calculated stress strain response in Fig 4.2.3a. From 13 kg/m^3 to 26 kg/m^3 (+43%) then from 26 kg/m^3 to 39 kg/m^3 (+165%), the residual or plateau region stepping upwards with increasing fiber dosage. While this marked result is evidence in the measured toughness, first crack tensile strength is not largely affected by the varying fiber dosage with values of 1.89, 1.95 and 1.84 MPa for the 13, 26 and 39 kg/m^3 dosages respectively. The HPFRC simulation is a reasonable fit for the 13 and 26 kg/m^3 dosage curves, but fails to capture the almost linear unloading in the post cracking region of the 39 kg/m^3. This may be attributed to uneven distribution of fibers in the mix or larger concentrations of steel in the tensile region, leading to the steel-like yielding behavior at deflections in excess of 2mm.

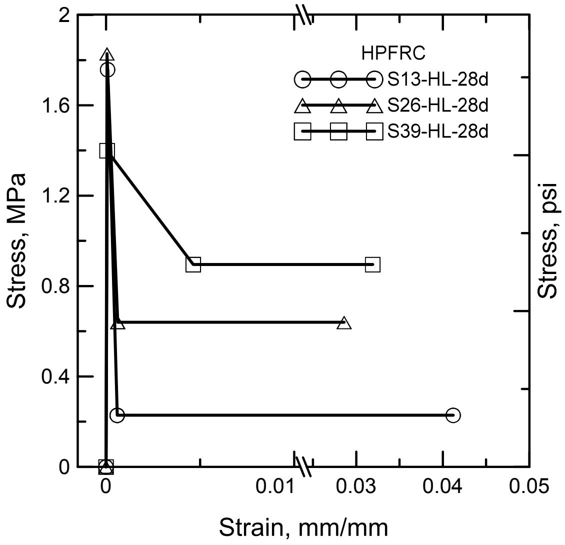

Figure 4.2.3a. Effect of steel fiber dosage on back calculated stress strain response

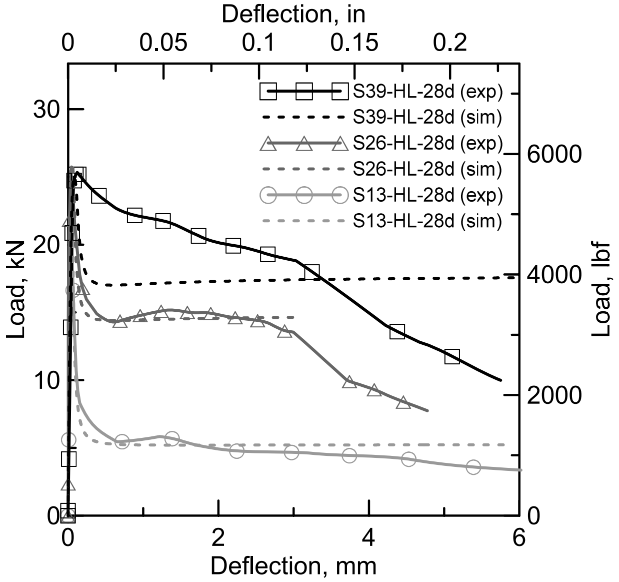

Figure 4.2.3b. Effect of steel fiber dosage on experimental and simulated load deflection response

At 28 days the UHPFRC showed very clear delineations between sample size (M or L) and fiber deformation type (H or T). The twisted fibers in both the M and L sample sizes showed increases in flexural toughness, (+116%) and hooked fibers (+190%). Peak flexural load also seems influenced by sample size and fiber deformation with 40, 57, 87 and 98 kN for the HM, TM, HL and TL samples respectively. The larger (L) samples show a slightly higher deflection capacity with 6mm compared to the medium (M) samples at 4mm. This additional ductility could be from the high volume fraction of steel, with the steel deforming and yielding as the load increases. This is also demonstrated in Fig 4.2.4b with the flexural simulation being an excellent fit for the experimental data through sample failure.

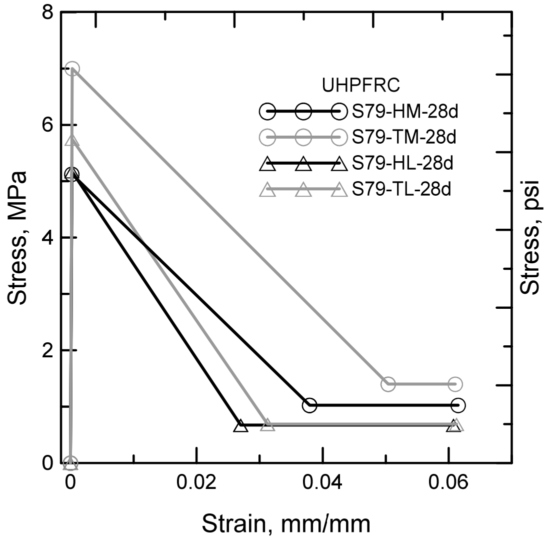

Figure 4.2.4a. Effect of sample size and steel fiber deformation on back calculated stress strain response

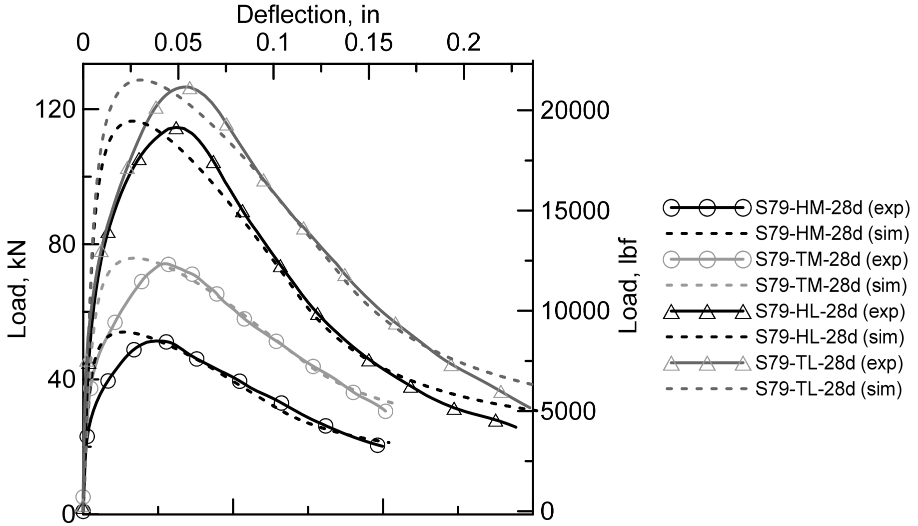

Figure 4.2.4b. Effect of sample size and steel fiber deformation on experimental and simulated load deflection response

4.3. Residual Strength in Comparison with Back-Calculated Residual Strength

4.3.1. Residual Strength by ASTM C 1609 ($\boldsymbol{f_{150}^{D}}$)

In this method, beam specimens having a square cross-section of fiber-reinforced concrete are tested in flexure using a third-point loading arrangement under a closed-loop, servo-controlled testing system. Load and net deflection are monitored and recorded to an end-point deflection of at least L/150.As shown in Fig. 4.3.1d, ASTM C 1609 method overestimates the residual uniaxial tensile strength defined under the present approach as $\mu E\varepsilon_{cr}$. A plot of corresponding values from two tests reflects a factor of almost three times. Therefore, it is imperative to note that the f_{150}^{D} parameter can be used as a tensile stress measure associated with the post crack tensile strength parameter σ_{cst} in Fig. 2.1.1b, so long as the Average Residual Strength (ARS) values are corrected by a scale factor of 1/(2.94).

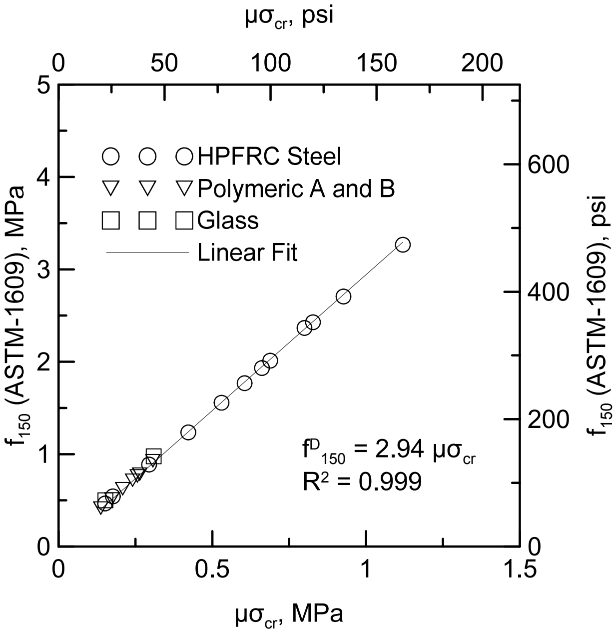

Figure 4.3.2. Comparison of residual strength ($\mu\sigma_{cr}$) with ASTM-1609 residual parameter

4.3.2 Residual Strength by JCI-SF4 ($\boldsymbol{\sigma_b}$)

Similar to ASTM C 1609, JCI-SF recommends testing fiber reinforced concrete by third-point loading and measuring the net deflection by Linear Variable Differential Transformers (LVDTs). As shown in Fig. 4.3.3, direct correlation of JCI residual strength and the present method indicate JCI-SF4 method overestimates the residual uniaxial tensile strength $\mu E\varepsilon_{cr}$ by as much as three times as well. The correction factor for the JCA method is 1/(3.22).

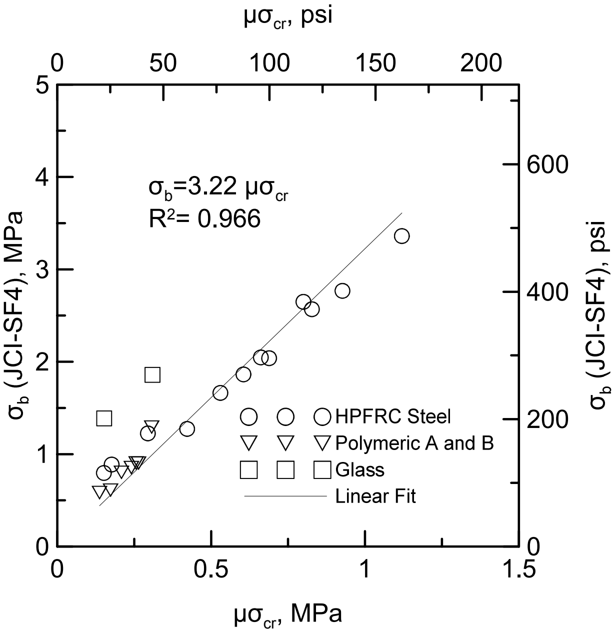

Figure 4.3.3.Comparison of residual strength ($\mu\sigma_{cr}$) with JCI-SF4 residual parameter

4.3.3. Residual Strength by RILEM TC 162-TDF ($f_{eq,3}$)

According to RILEM TC 162-TDF [4] bending test method can be used for the determination of residual flexural tensile strength. In the RILEM method, the tensile behavior of fiber reinforced concrete is obtained by the load-deflection curve when a simply supported notched beam of 150 x 150 mm cross section and 500 mm is loaded under three-point bending arrangement and the test is executed by means of CMOD (Crack Mouth Opening Displacement) control. It is noted that in the proposed methods for design by fib [41], a correction factor of 1/3 is used for scaling the parameter f_{R3} from flexural tests to obtain f_{Ftu} which represents the ultimate residual strength. This correction factor was obtained by calibration of various specimen sizes, and various fiber types and dosages. The proposed value and the present calculation therefore correlate quite well. The present approach can be used as theoretical justification for the empirical values obtained and used in the FIB model code.

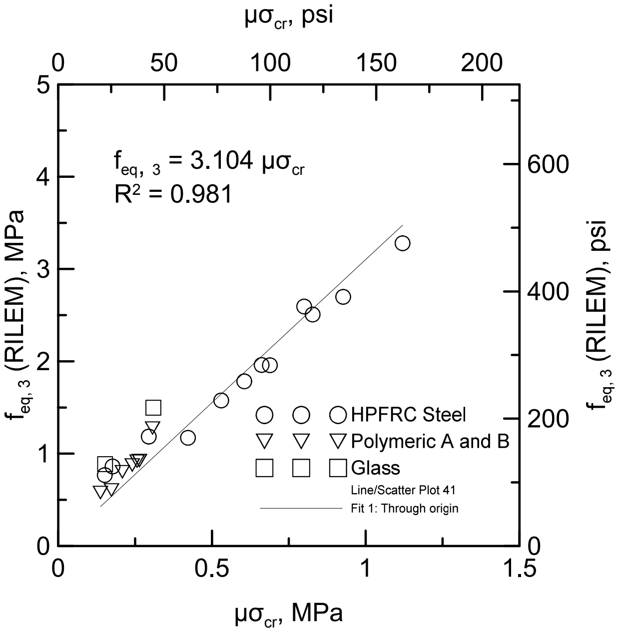

Figure 4.3.5 Comparison of residual strength ($\mu\sigma_{cr}$) with RILEM residual parameter for macro synthetic fibers.

Table 4.3.1 Residual strength parameter summary for the study.

	Residual Parameter	k_{bt}
ASTM C1609	f^D_{150}	2.94
RILEM TC 162-TDF	$f_{eq,3}$	3.10
JCI-SF4	σ_b	3.22

$$f_{150}^{D} = 2.94\mu\sigma_{cr} \tag{4.3.1}$$

$$f_{eq,3} = 3.10\mu\sigma_{cr} \tag{4.3.2}$$

$$\sigma_{b} = 3.22\mu\sigma_{cr} \tag{4.3.3}$$

Table 4.3.1 and equations 4.3.1, 4.3.2 and 4.3.3 summarize the residual strength relationship for the early age study with the linear coefficient k_{bt} for each case.

4.4 Conclusion

Characterization of tensile-flexural strain softening of fiber cement composites with alternative curing times shows that the presence of fiber significantly increases the ductility of the material. By applying the load deflection back-calculation technique one can generate strength data with a higher degree of accuracy than the current standard methods. Using a closed form set of governing parameters and variables applied through each stage of material response, the stress distribution that considers a shifting neutral axis can be simulated which provides a more accurate representation of the residual strength and toughness of FRC.

Since the inherent assumption of the available standard method assumes that the neutral axis is still at the centroid of the specimen, and the stress distribution is linear throughout. This leads to very high nominal flexural stress levels in tension fiber which are far more than tensile strength. Extreme caution must be exercised in application of the ASTM 1609, JCI-SF4 and RILEM TC 162-TDF methods in design and analysis of fiber reinforced concrete sections, as the results show overestimation of the residual parameter by as much as 2.95-3.11 times.

Chapter 5

POST CRACKING CHARACTERIZATION OF FABRIC AND STEEL FIBER REINFORCED CONCRETE USING STRAIN HARDENING MATERIAL MODEL

5.1. Analysis - Prediction of Load Deflection Response of Fabric Cement Composites

Two types of composites consisting of TRC composites and ECC materials were used. Three different TRC composites consisting of upper and lower bound AR-Glass with alternate 100lb or 200lb of confinement pressure and/or the addition of 40% fly ash were [42]. These composites were manufactured using a cement paste with a w/c=0.45, and 8 layers of AR-Glass manufactured by Nippon Electric Glass Co. In order to correlate the responses, experimental data from a set of specimens under uniaxial tension and three point bending tests were used. No attempt was made to obtain a best fit curve to the response. The textile reinforced composites had Tension specimens were approximately 10x25x200 mm. The flexural specimens for the three point bending test were 10x25x200 mm with a clear span of 152 mm. The material parameters for the tension model were determined by fitting the hardening model to the uniaxial tension test and flexural test. The result is shown by the simulated upper and lower bounds encompassing all the selected TRC's in Figures 5.1.1(a) &(b). Figure 5.1.1a shows the predicted flexural load deflection response of cement composites and Figure 5.1.1b shows the tensile stress strain responses used in the simulation compared with experimentally obtained results. Representative properties for the simulation of upper bound values obtained from the GNS200 samples were: α=50, μ=3.9, η=0.06, γ=5.0 and ω=10 the constants were ε_{cr} =0.0002,and E=20000 MPa, while the limits of the modeling were β_{tu} =135, and λ_{cu}=40. The representative material properties for the lower bound values from the GFA40 samples were: α=32, μ=2.0, η =0.032, γ =5.0 and ω =10 the constants were ε_{cr} =0.00018, and E = 20 GPa, while the limits of the modeling were β_{tu} = 150, and λ_{cu} = 40.Values shown are for a preliminary set of data and proper model optimization with upper and lower bound values for each variable are required.

Table 5.1.1 – Data from experimental analysis of representative TRC and ECC samples.

Sample ID	b (mm)	d (mm)	L (mm)	Elastic Flexural Stiffness (N/mm)	Defl @ Max Flex Load (mm)	Max Flex Load (N)	Bending Stress (MPa)	Flexural Toughness N.mm/mm^2
GNS200	30	9	152	801	5.84	520	49	7.91
GNS100	34	7	152	565	6.25	138	20	2.88
GFA40	24	8	152	510	5.38	226	26	4.64
ECC-PE2	76	102	305	60351	6.23	30114	12	26.36

Table 5.1.2 – Material properties and model parameters from back calculation model of representative TRC and ECC samples.

Sample ID	Young's Modulus (E) GPa	First Crack Tensile Strength (σ_{cr}) MPa	Normalized Post Crack Tensile Strength (μ)	Normalized Transition Tesnile Strain (α)	Transitional Tensile Strain (ε_{trn}), %	Ultimate Tensile Strain (ε_{tu}), %
GNS200	20	5	3.9	50	1.25	2.5
GNS100	20	3.6	2	32	0.576	2.7
GFA40	21	4.62	2.3	70	1.54	2.09
ECC-PE2	4.75	2.85	1.4	95	5.7	7.8

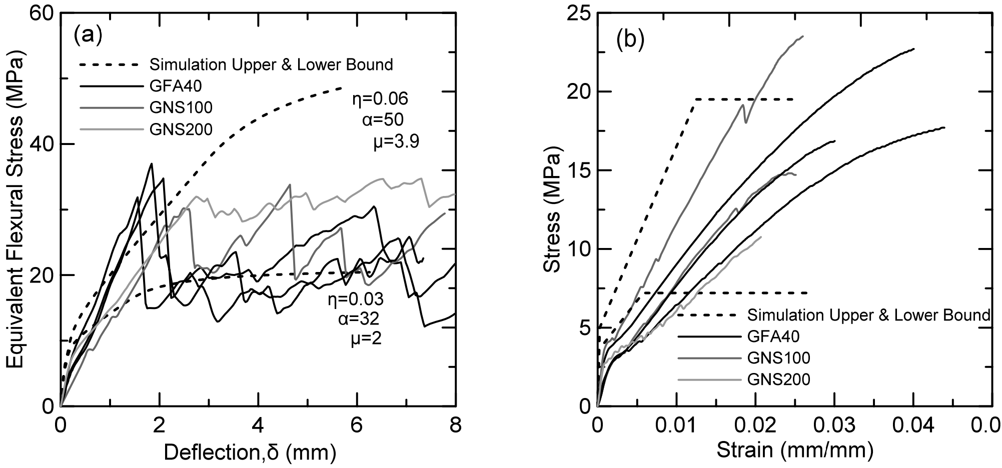

Figure 5.1.1– Strain hardening model of TRC (a) Equivalent Flexural Stress Deflection and corresponding (b) Stress Strain response.

An ECC mix that utilizes polyethylene (PE) fibers at volume fraction levels of 2.0% from the literature [43,44] was also modeled. The flexural specimens for the four point bending test were76.2 x 101.6 x 355.6 mm with a clear span of 304.8 mm [45]. Predicted load–deflection response is shown in Figures 5.1.2 (a) & (b).

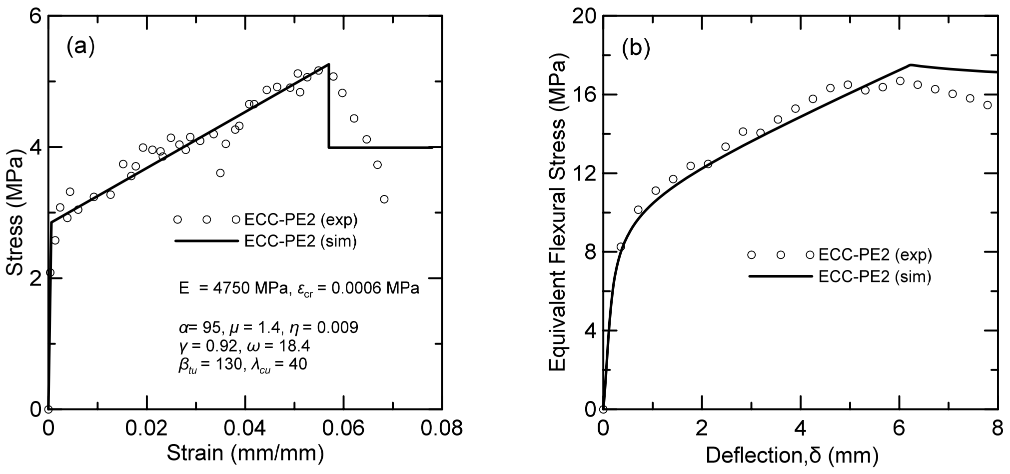

Figure 5.1.2 – Engineered Cementitious Composite *(a) Stress Strain response and (b) Equivalent Flexural Stress Deflection (Load Deflection).*

5.2. Analysis - Prediction of Load Deflection Response of Steel Fiber Reinforced Composite

There has been research work carried out by Naaman [46] that studies the response of two high strength steel fibers (hooked and twisted) with an identical volume fraction of fibers (1%) and three different sized cross sections (50x25mm, 100x100mm and 150x150mm) in an ultra high performance cement (UHPFRC). An experimental program was designed to correlate the tensile and bending response of fiber reinforced cement composites, tested under the same conditions. This experimental program also enables the observation of scale effects on bending behavior. The objective is to determine if the tensile stress-strain response of fiber reinforced cement composites can be predicted from their load deflection response.

The matrix mix composition and proportions are shown in Table 5.2.1, and the properties of fibers are shown in Table 5.2.2. A VMA (Viscosity Modifying Agent) was added to the matrix to increase viscosity and ensure uniform fiber distribution in the matrix. The compressive strength of the matrix was measured from 100x200 mm cylinders and this matrix was a self-consolidating mixture developed earlier.

Table 5.2.1. Fiber Properties used in the study [46]

Fiber Type	Diameter (mm)	Length (mm)	Density (g/cc)	Tensile Strength (MPa)	Elastic Modulus (GPa)
Hooked	0.38	30	7.9	2206	200
Twisted	0.3	30	7.9	2100	200

Table 5.2.2. Matrix composition by weight ratio and compressive strength.

Cement (Type III)	0.8
Fly Ash	0.2
Sand (Flint)	1
Silica Fume	0.07
Super-Pasticizer	0.04
VMA	0.012
Water	0.26
f'c (Mpa)	84

5.2.1 Experimental Results

By performing back-calculation of the material properties, a comparison can be shown with the data obtained from a tensile test. This comparison validates the accuracy of the material model and clearly shows how the effect of sample size is correlated to accuracy of experimental versus simulated data.

Experimental deflections were taken to 6mm, but simulations were conducted at deflections of 2mm and were based on design criteria of approximately L/150 for most beam conditions. Experimental equivalent bending strength versus deflection responses for small (50x25x300mm), medium (100x100x300mm) and large (150x150x450mm) sample geometries are shown in Fig 5.2.1 (a-c). This removes any normal effects that are induced by the size of the sample, but even with this taken into account there is variation in the flexural capacity when sample sizes are increased. The small size sample size exhibit traditional strain hardening behavior with a marked increase in flexural strength from the onset of cracking to 2mm of deflection (+52%). There is little difference in the effect of fiber type at this size geometry, with both samples behaving similarly up to 2mm of deflection. With a large volume fraction of steel fibers the behavior of the sample is being dominated by the steel as yielding is the primary failure mechanism once cracking occurs. Both medium and large size sample geometries show a marked increase in the equivalent flexural strength in comparison with the small size (+500%). This is due to a change in the primary failure mechanism for the larger geometry samples to fiber pullout over yielding. Medium sized sample geometry shows a larger difference (+30%) in equivalent flexural capacity between hooked and twisted fiber types. The larger sample shows a smaller difference, but this could all be attributed to variability in the data for either medium or large sample sizes. Experimental load deflection curves are shown in figure 5.2.2 (a-c). Direct tension tests were also conducted by Naaman, the digitized average stress strain responses for both hooked and twisted fibers are shown in figure 5.2.3 and will be compared in the section with the simulated stress strain results. Table 5.2.1 summarizes the experimental analysis for all samples.

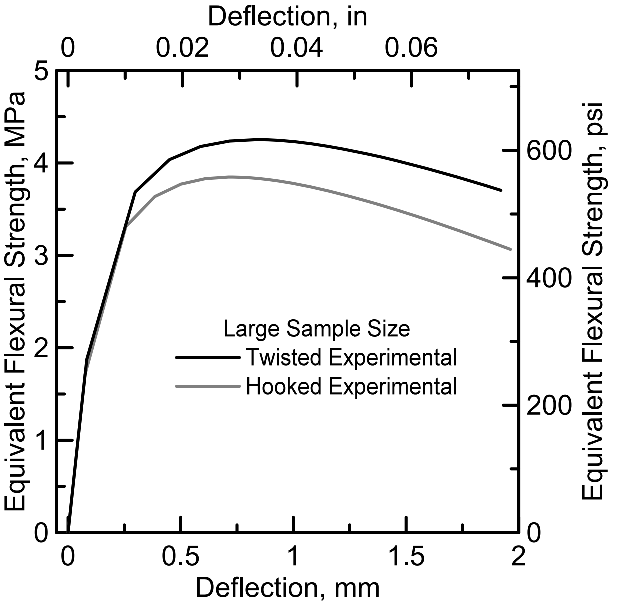
Deflection, in
0
0.02
0.04
0.06
5
4
3
2
1
0
600
400
200
0
Equivalent Flexural Strength, MPa
Equivalent Flexural Strength, psi
Large Sample Size
Twisted Experimental
Hooked Experimental
0
0.5
1
1.5
2
Deflection, mm

(a)

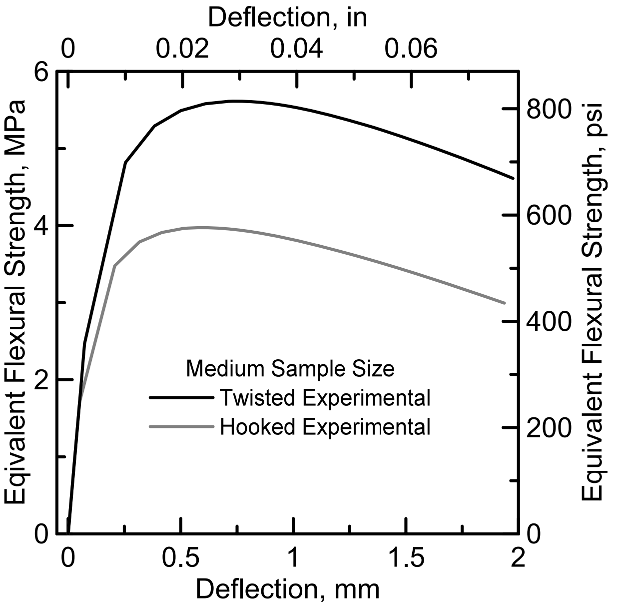
Deflection, in
0
0.02
0.04
0.06
6
4
2
0
800
600
400
200
0
Eqivalent Flexural Strength, MPa
Equivalent Flexural Strength, psi
Medium Sample Size
Twisted Experimental
Hooked Experimental
0
0.5
1
1.5
2
Deflection, mm

(b)

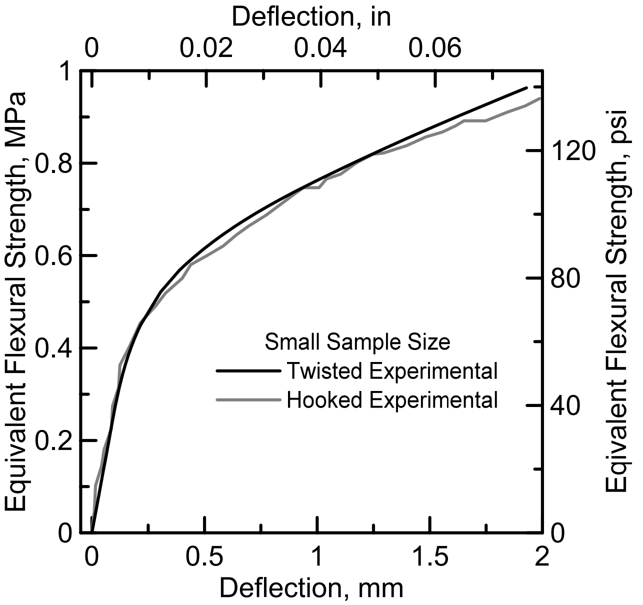

(c)

Figure 5.2.1 Equivalent bending strength for (a) large, (b) medium and (c) small sample geometries.

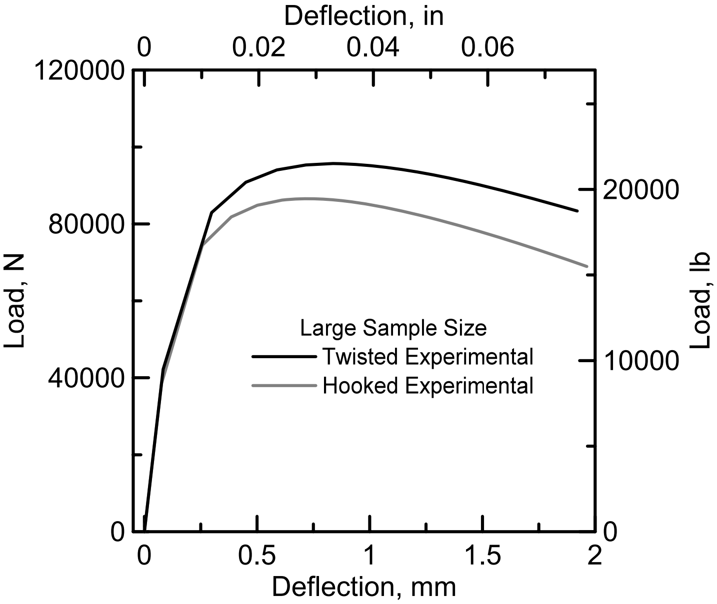

(a)

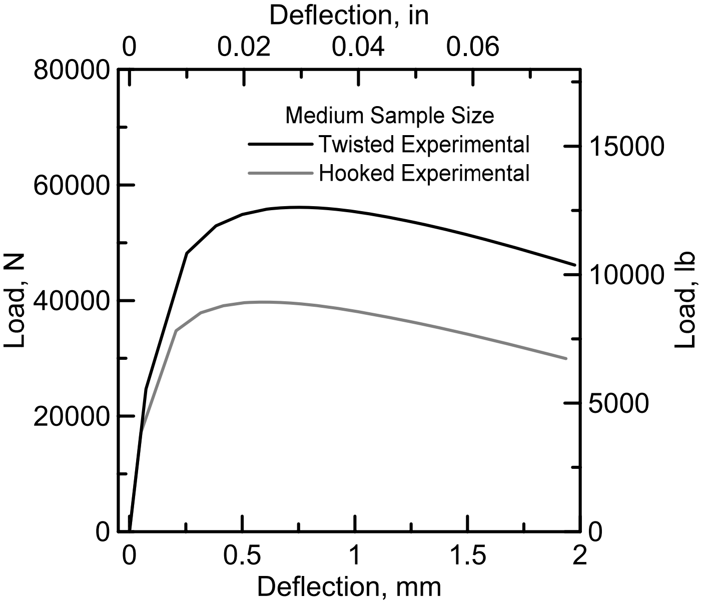

(b)

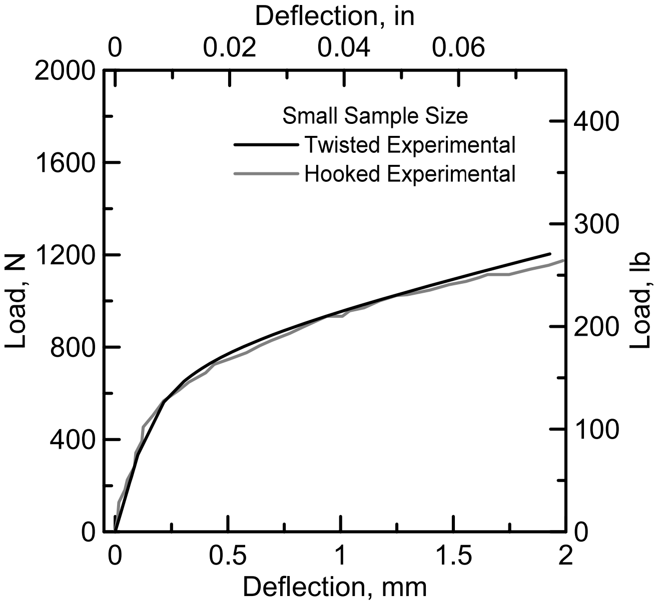

(c)

Figure 5.2.2 Experimental load deflection response for (a) large, (b) medium and (c) small sample geometries.

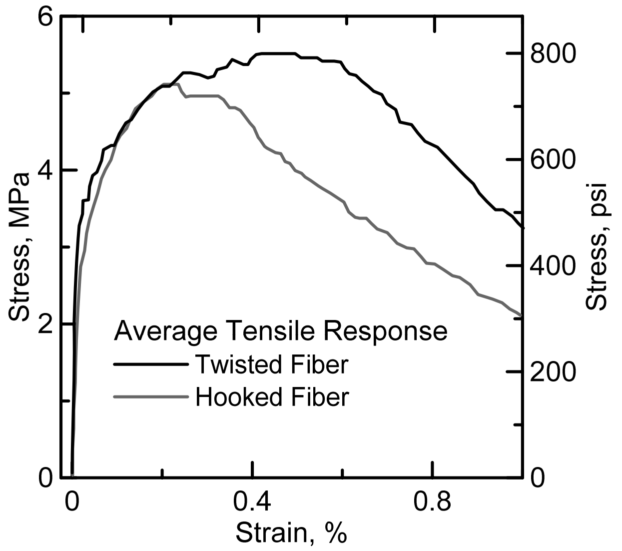

Figure 5.2.3 Average stress strain response for all sample geometries.

Table 5.2.3 Summary of experimental analysis for all samples

Sample Size (mm)	Fiber Type	Bending Strength (MOR), Mpa	Flexural Stiffness, kN/mm	Load @ 1st Crack, kN	Defl @ 1st Crack, mm	Max Flex Load, kN	Defl. @ Max Load, mm	Deflection Capacity, mm	Stress @ Max Load, Mpa	Flexural Toughness (GF), kN.mm
50x25x300	T	14	3.3	0.5	0.15	1.5	1.84	4.5	130	5.7
100x100x300	T	15	406.8	15.8	0.0388	51.2	0.498	1.53	134	63.55
150x150x450	T	14	584.7	34.1	0.0582	105.3	0.72	1.19	124	103.75
50x25x300	H	13	2.6	0.5	0.171	1.3	1.33	4.03	66	4.313
100x100x300	H	11	355.9	13.8	0.0388	36.8	0.295	1.05	63	34.351
150x150x450	H	12	559.3	32.6	0.0582	90.5	0.513	1.21	79	89.673

5.2.2 Simulation Results and Discussion

The results of the simulation are presented based on the digitization of the flexural and tensile data presented by Naaman [46]. The results are presented to display how sample size affects the tensile strength and accuracy of the bending model to predict tensile parameters. Results include individual experimental and simulation comparisons of load deflection responses for each fiber type and geometry. The simulated tensile stress strain output is also compared with the average experimental stress strain response for all sample geometries.

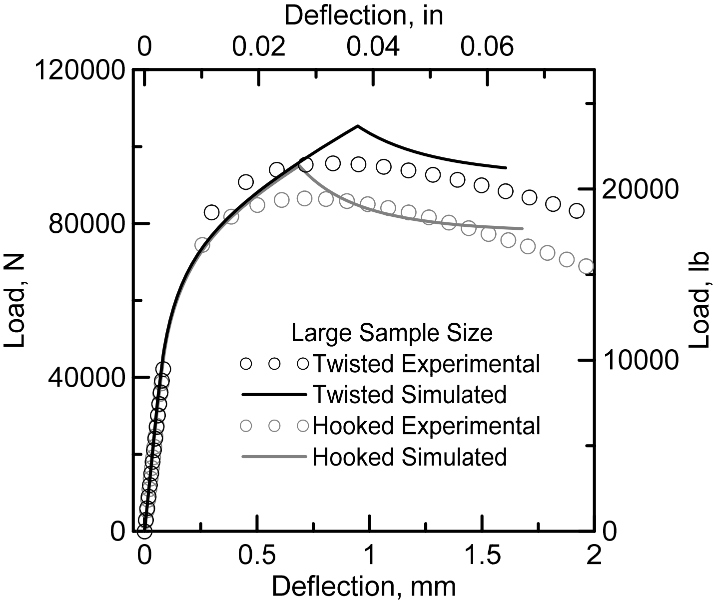

(a)

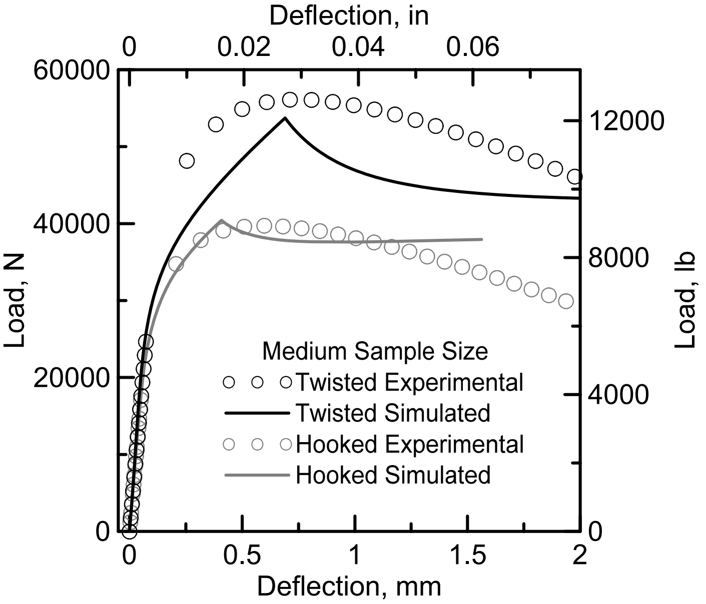

(b)

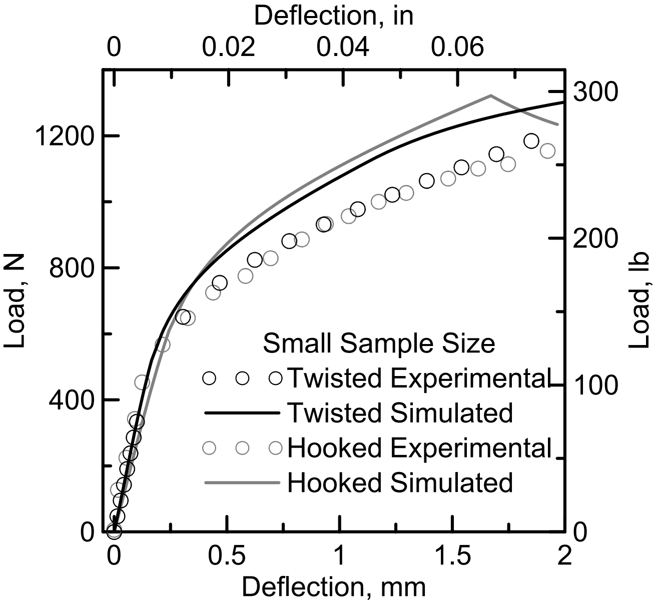

(c)

Figure 5.2.4 Simulated and experimental load deflection curves for hooked and twisted fiber types for (a) large, (b) medium and (c) small sample geometries.

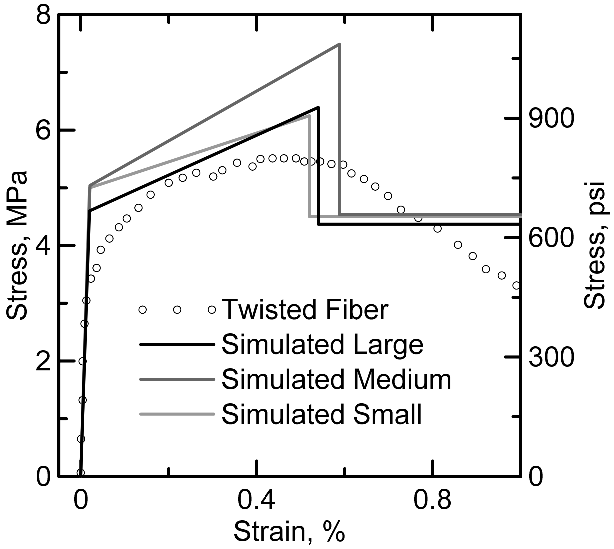

(a)

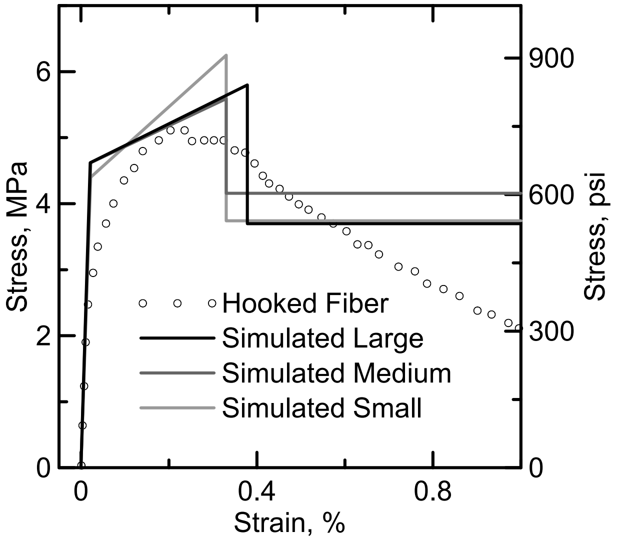

(b)

Figure 5.2.4 Averaged experimental tension response compared with simulated flexural tensile response for (a) twisted and (b) hooked fibers.

Table 5.2.2 Summary of back calculated parameters and material properties.

Sample Size (mm)	Fiber Type	Young's Modulus (E) Mpa	First Crack Tensile Strength (σcr) MPa	Post Crack Tensile Strength (μ)	Transition Tesnile Strain (α)	Transitional Tensile Strain (εtrn), μstr	Ultimate Tensile Strain (εtu), mm/mm	Residual Strength (μσcr), MPa	Tensile Toughness (Gf), MPa
50x25x300	T	25000	5	0.9	26	5200	15000	4.5	0.0683
100x100x300	T	24000	4.8	0.9	28	5600	21000	4.32	0.0916
150x150x450	T	23000	4.6	0.95	27	5400	10000	4.37	0.0439
50x25x300	H	20000	4.4	0.85	15	3300	13200	3.74	0.05
100x100x300	H	21000	4.2	0.9	15	3000	14000	3.78	0.0532
150x150x450	H	22000	4.4	0.8	18	3600	10400	3.52	0.0378

The given material model is effective in simulating strain hardening materials such as fabrics and ultra high strength fiber reinforced cement composites with high volume fractions of steel fibers. Material properties between the hooked and twisted (E and εcr) varied between 20% and 10% respectively for the small, medium and large specimen geometries. The values for the residual parameter μ were above the threshold of 0.34 characterizing strain hardening behavior in the material model [30]. The residual strength, characterized by μσcr, was higher for the twisted fiber types by (+17%) for the small, (+13%) for the medium and (+19%) for the large sample geometries. This indicates that the twisted fiber type has superior residual strength qualities; resisting both fiber pullout and yielding for each geometry.

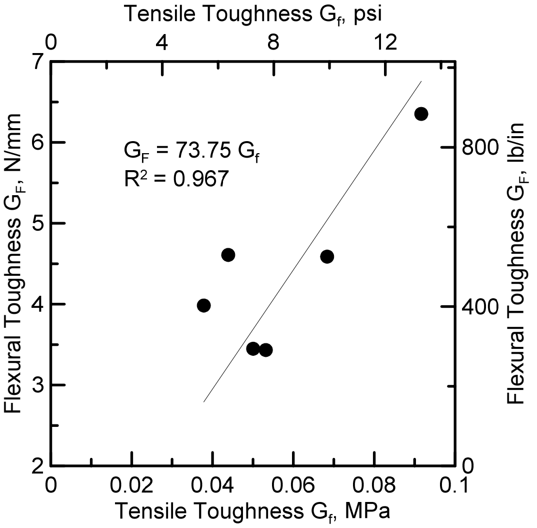

Figure 5.2.5 Flexural toughness as a function of tensile toughness

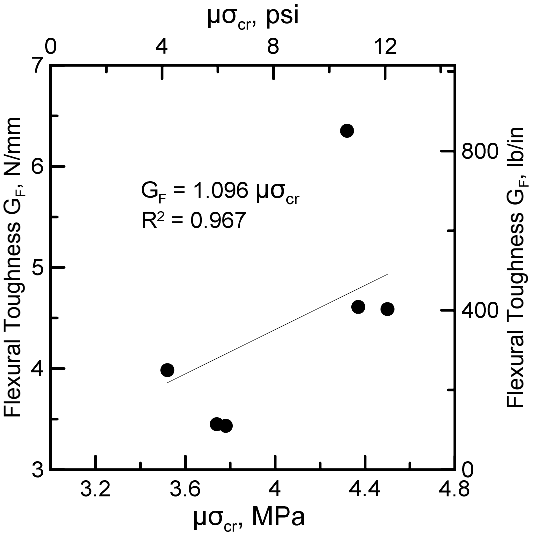

Figure 5.2.6 Flexural toughness as a function of the residual strength parameter.

5.3 Conclusions

The presentation of two independent studies where strain hardening behavior dominates the material behavior under loading conditions validates the given material model to effectively simulate these types of materials. In effectively simulating and characterizing the residual strength of strain hardening materials, we have a basis for comparison and implementation of design procedures. In characterizing the residual strength we were able to establish that twisted fibers in small medium and large geometry sizes had larger residual strength in UHPFRC.

Chapter 6

FINITE ELEMENT MODELS FOR ROUND DETERMINATE PANELS (ASTM C1550) AND FLEXURAL TESTING

6.1 Introduction to Limit Analysis Approach (ASTM C-1550)

Understanding the fundamental mechanics of material behavior is essential to the development of more advanced models. Before finite element models can be introduced the overall behavior of the round discrete panel (RDP) must be explored. The limit analysis approach is an upper bound method that assumes rigid segment rotations and uniform crack width along yield lines. This gives way to a more accurate method, where integration of the moments as functions of the radius is done along the cracks. This more accurately captures the actual sample behavior throughout the test.

From Figure 6.1.1. (a), we can determine that crack segment 1 rigidly rotates around the axis AB and the relationship between central deflection and deflection at the edge is shown by equation (6.1.1).

$$\frac{\delta_C}{\delta} = \frac{BC}{AO} = \frac{R\sin(30)}{R} = \frac{1}{2}$$

$$\delta_C = \frac{\delta}{2} \tag{6.1.1}$$

Thus, the deflection at the edge (point C) is half of the central deflection. We assume each crack segment is rigid and it rotates around the crack axis represented by vectors v_{OC}, v_{OD} and v_{OE} as shown in Figure 6.1.1. (b).

$$v_{OC} = \begin{Bmatrix} R \\ 0 \\ \dfrac{\delta}{2} \end{Bmatrix} \quad v_{OD} = \begin{Bmatrix} -R\sin(30) \\ -R\cos(30) \\ \dfrac{\delta}{2} \end{Bmatrix} \quad v_{OE} = \begin{Bmatrix} -R\sin(30) \\ R\cos(30) \\ \dfrac{\delta}{2} \end{Bmatrix} \tag{6.1.2}$$

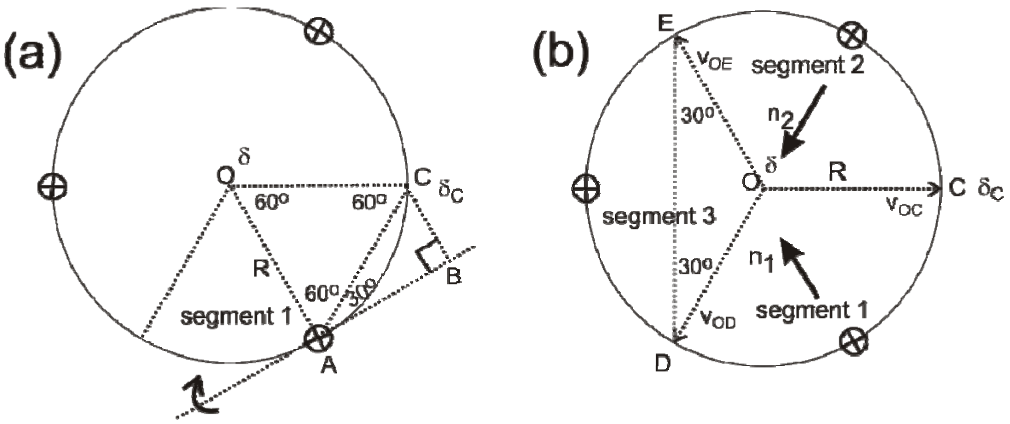

Figure 6.1.1 - Round determinate panel test (a) relationship between deflection at the edge and at the center; (b) rigid crack rotation between segment 1 and 2.

The vectors normal to crack segment 1 and 2 can be found by cross product of the two adjacent vectors.

$$n_1 = v_{OD} \times v_{OC} = \begin{Bmatrix} -\dfrac{\sqrt{3}}{4}R\delta \\ \dfrac{3}{4}R\delta \\ \dfrac{\sqrt{3}}{2}R^2 \end{Bmatrix} \quad n_2 = v_{OC} \times v_{OE} = \begin{Bmatrix} -\dfrac{\sqrt{3}}{4}R\delta \\ -\dfrac{3}{4}R\delta \\ \dfrac{\sqrt{3}}{2}R^2 \end{Bmatrix} \tag{6.1.3}$$

The rotation θ between segment 1 and 2 is the angle between these two normal vectors, determined by the dot product.

$$\theta = \cos^{-1}\left\{ \frac{n_1 \bullet n_2}{|n_1||n_2|} \right\}$$

$$\theta = \cos^{-1}\left\{ \frac{-\delta^2 + 2R^2}{2\left(\delta^2 + R^2\right)} \right\} \tag{6.1.4}$$

The central deflection of the panel δ is incrementally imposed and the rotation of the yield line *θ* can be determined by implementing equation (6.1.4). Once the rotation of the yield line is known, the moment per unit width *m* can be determined implementing yield line theory. In summary, yield line theory is an approach that uses work energy for analysis and assumes that the internal energy expended (E) is equal to the energy dissipated (D) during the failure mechanism of an RDP as shown by Equation (6.1.5a). The external energy expended (E) is calculated by taking the resultant of the applied load acting on a region and multiplying it by its vertical displacement, measured as a proportion of the maximum deflection implied by the proposed yield line pattern. The total energy expended for the whole sample is the sum of the expended energies for all the regions, and is represented by the left side of Equation (6.1.5b). For the RDP samples, the expended energy was calculated at the center of the sample, to coincide with collected experimental load deflection data. The internal energy dissipated (D) is calculated by taking the projected length of each yield line around a region onto the axis of rotation of that region, multiplying it by the moment acting and by the angle of rotation attributed to that specific region. The total energy dissipated for the whole sample is the sum of the dissipated energies for all the regions; see the right side of Equation (6.1.5b). The RDP models should experience three yield lines at approximately 120 degrees apart, with three independent rigid segments rotating about three different axes of rotation that pass through each support, tangential to the sample edge. Equation (6.1.5c) gives the incremental summation of the energy balance as it applies to the RDP test.

$$E = D \tag{6.1.5a}$$

$$\sum (P \times \delta) = \sum (m \times R \times \theta) \tag{6.1.5b}$$

$$P_i \delta_i = 3Rm_i \theta_i \tag{6.1.5c}$$

$$m_i = \frac{P_i \delta_i}{3R\theta_i} \tag{6.1.6}$$

Where *P* is the applied load, *δ* is the edge deflection, *m* is the moment per unit width, *R* is the sample radius and *θ* is the rotation of the three yield lines. By obtaining *θ* from Equation (6.1.4) and experimentally gathering *P, δ* and *R*, we can solve Equation (6.1.5c) for the incremental moment per unit length, *m*, as shown by Equation (6.1.6). This approach however does not consider that the rotation along each crack changes as a function of the radius of the panel. The rotation of the crack at the outer edge is much larger than closer to the center, for this reason we must integrate the moment as a function of rotation along the radius for each of the three cracks. By assuming a linear relationship between rotation and radius Equation 6.1.7can be assumed (as shown from Figures 6.1.2 and 6.1.3) and Equation 6.1.8 can be derived as the relationship of $\theta_{\max}$ and the radius are substituted into Equation 6.1.9, where n is the number of cracks, M is the moment, θ is the rotation, α is the slope of the rotation – radius plot and R is the radius.

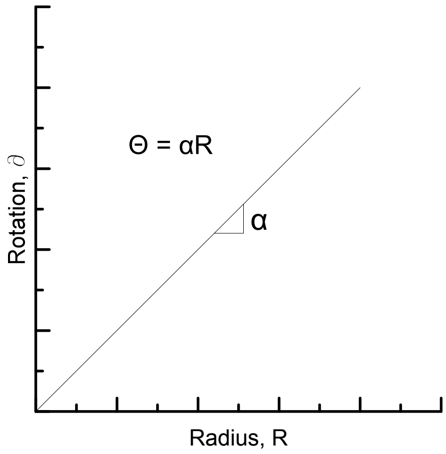

Figure 6.1.2 Rotation as a function of Radius, assuming linear relationship.

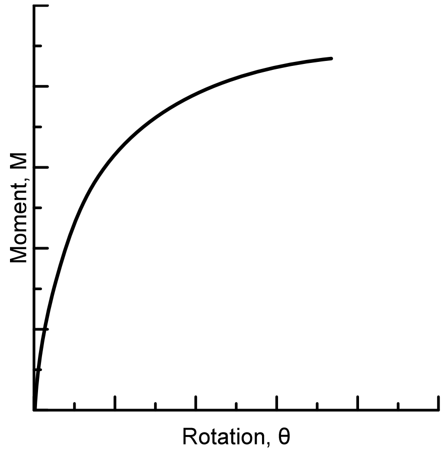

Figure 6.1.3 Moment as a function of rotation

$$\theta = \alpha R \tag{6.1.7}$$

$$P\delta_i = n \int_0^{\theta \max} M(R,\theta)d\theta \tag{6.1.8}$$

$$P\delta_i = n \int_0^{\alpha R \max} M(\theta)\alpha dR \tag{6.1.9}$$

Equation 6.1.9 is a much more comprehensive interpretation of the fundamental mechanics approach, which only assumes rigid rotation and constant rotation along the cracks.

6.2 Finite Element Model of ASTM C-1550

A round determinate panel (RDP) test on three equally spaced simple supports is a convenient method to determine the flexural capacity of fiber reinforced concrete slabs (ASTM C-1550). In comparison to other panel tests that come in different shapes, sizes and support conditions, the round panel test yields only the load deflection response, which is used for material characterization purposes. The load deflection response from this test can then be used to back-calculate the shotcrete material properties using the finite element method in terms of the Young's modulus, Poisson's ratio and tensile stress crack width relationship. With a proper set of material parameters, the numerical models can simulate the experimental load deflection responses and estimate the moment capacities of the round panels. The geometry of the numerical model was taken from approximate measured values from the RDP test specimens with a diameter of 800mm and a 76mm thickness. The domain was them discretized into 156 first order shell elements with reduced integration (S4R) and 21 Simpson points were used to calculate the shell thickness stiffness for a nonlinear stress strain distribution.

The static load test was modeled as a quasi-static problem using an explicit dynamic analysis. The use on an explicit scheme was used over implicit to avoid the numerical challenges encountered in the nonlinear analysis of the softening post peak response. The time scale required to simulate a very slow static load test (with the explicit algorithm) is very large, so the quasi-static analysis must conducted at a much faster rate of loading. When dynamic analysis is used, the rate of loading introduces undesirable inertial effects, which add to the applied load on the specimen. A previous study has revealed at a loading rate of 30mm/2 seconds, the explicit analysis can simulate an actual static load speed of 1mm/min. The reaction force at the center of the panel was then calculated to represent the applied load at each incremental displacement.

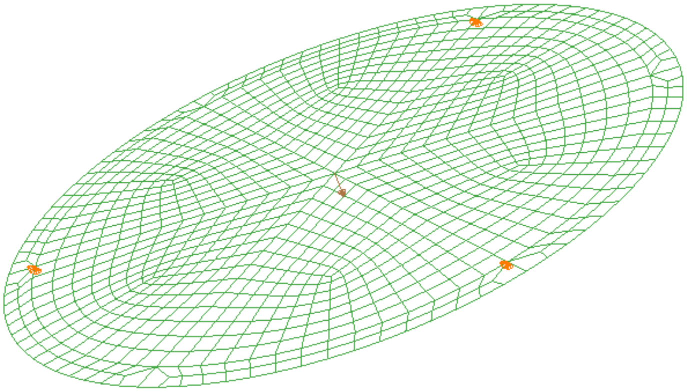

Figure 6.2.1 Mesh rendering of RDP with support conditions and central loading.

The ASTM C-1550 test method covers the determination of flexural toughness of fiber-reinforced concrete expressed as energy absorption in the post-crack range using a round panel supported on three symmetrically arranged pivots and subjected to a central point load. The performance of specimens tested by this method is quantified in terms of the energy absorbed between the onset of loading and selected values of central deflection.

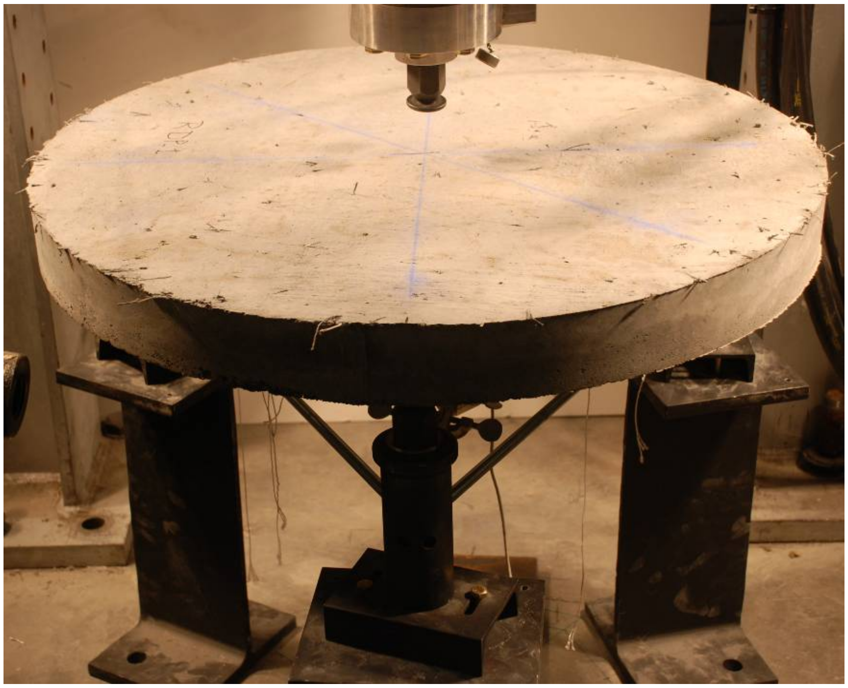

Figure 6.2.2 Typical round discrete panel (RDP) test, three symmetric supports with load applied at center.

Figure 6.2.3 RDP showing three symmetrical supports, load cell and LVDT.

Figure 6.2.4 RDP with three concentric radial cracks at approximately 120 degrees.

The visualization of the model as it undergoes a constant rate of central incremental displacement in the U3 direction is shown in Figure 6.2.5. while

Figure 6.2.6 clearly shows the location of the symmetric points of failure of the RDP as the localization of strain energy.

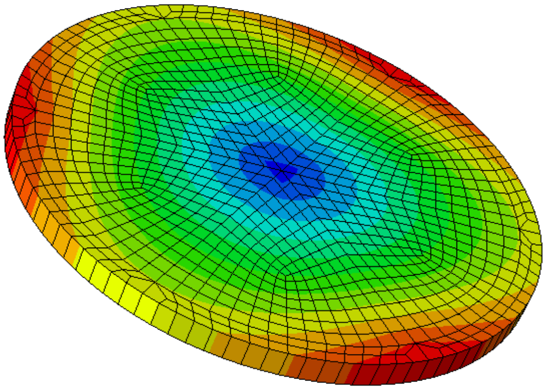

(a)

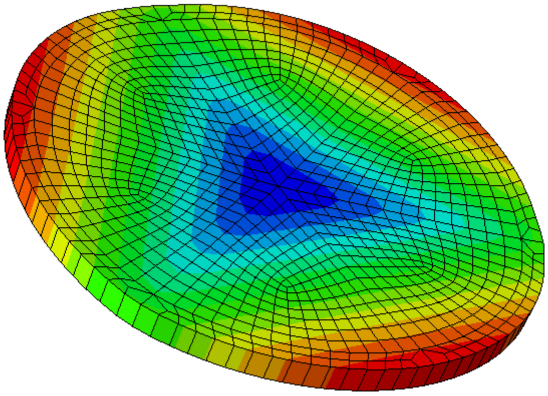

(b)

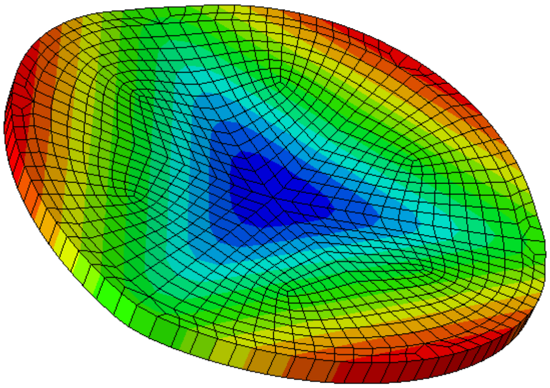

(c)

Figure 6.2.5 (a-c) Finite element simulation of a round determinate panel test subjected to a point load at the center (by constant rate of displacement) at progressive stages of deformation

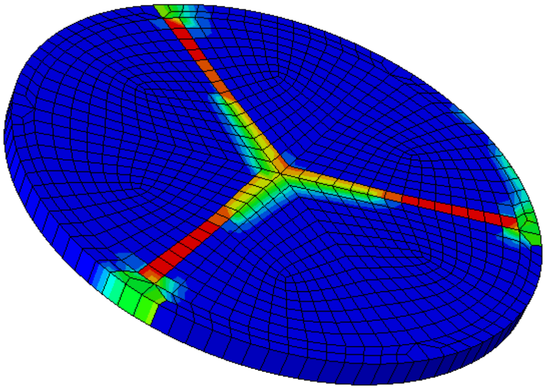

(a)

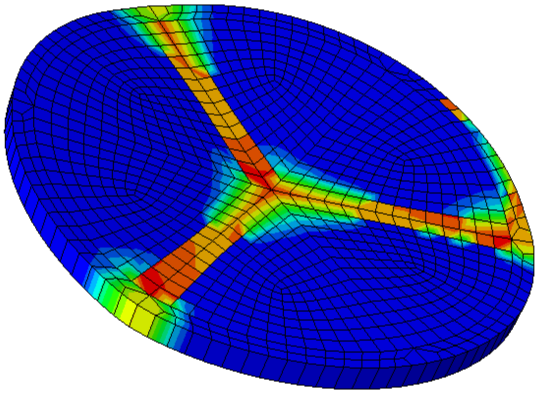

(b)

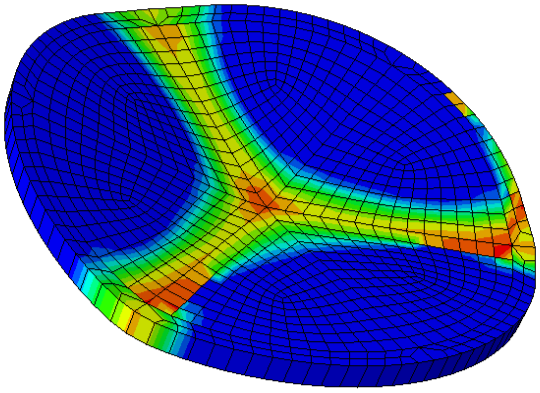

(c)

Figure 6.2.6 (a-c) Finite element simulation of a round determinate panel showing strain energy density along radial crack locations at progressive stages of deformation.

6.3 Finite Element Model of ASTM C-1609

In order to predict the load deflection response of a round panel test with the rigid crack model, moment curvature relationship of a panel and the size of a crack band width must be provided as an input. This information can be obtained directly from the yield line of a round panel test on 3 supports. Another possible source is to obtain the fundamental moment curvature response from the four point bending test, which is a simpler and more economical test method. If moment curvature response and crack band width can be estimated from the four point bending test and successfully predict the load deflection response of a round panel test, there is no need to conduct expensive round panel tests at all.

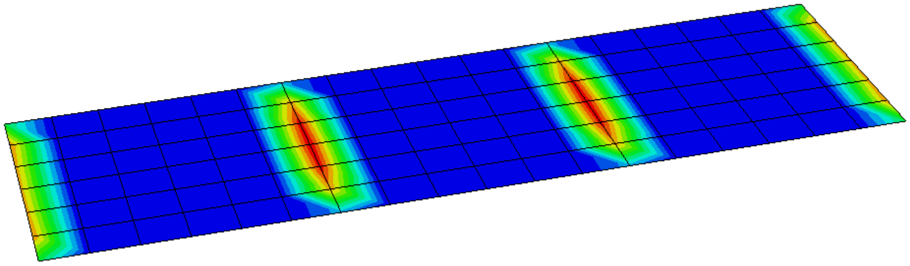

Figure 6.3.1 Finite element model for four-point bend test.

Fig. 6.3.1 shows the simplified finite element model of a four point bending test, which uses the same configurations as the round panel model: material parameters, rate of loading, mesh size, element types. The numerical specimen has a thickness of 150 mm, width of 150 mm and clear span of 450 mm. The boundary conditions at the left support are U1=U3=0; additional U2=0 at the mid support is imposed to prevent the movement in direction-2. The boundary condition at the right end is U3=0 with additional U2=0 imposed at the mid support. At third points of the beam, U3 is forced to move downward for a distance of 40 mm in 4 seconds, which is the same rate of loading as done in a round panel test.

6.4 ABAQUS Material Model

The finite element software ABAQUS with a concrete damaged plasticity model was utilized to capture flexural behavior of the round panel and four-point bending tests , which exhibit a nonlinear ascending curve followed by a softening post peak response. In the analysis of brittle materials, the traditional tensile stress strain model can lead to mesh sensitivity in which the finer mesh yields narrow crack bands and more abrupt failure while the coarse mesh yields a stronger system with a much higher ductility. In order to overcome mesh dependence of the model, the tensile stress crack width approach which employs fracture mechanics to limit the amount of energy released is used instead. For brittle materials, the load deflection response is primarily controlled by Young’s modulus, Poisson’s ratio and the tensile crack width parameters. The compressive and shear stresses developed in the sample are assumed to behave in the elastic range and assumed to be low. With these assumptions, the shotcrete model in ABAQUS is greatly simplified and can be described as shown in Figure 6.4.1.

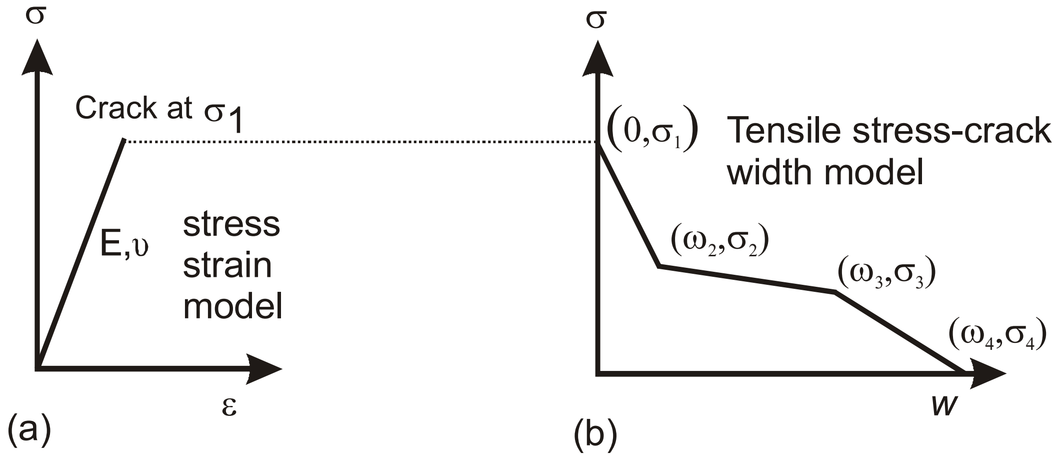

Figure 6.4.1 – Simplified concrete model: (a) before cracking; and (b) after cracking

Tension is assumed to behave elastically until it cracks and obeys the tensile-stress crack width relationship afterward. With this simplified model, only eight parameters (E, υ, σ_1, ω_2 σ_2, ω_3, σ_3, ω_4) needed to be resolved in the inverse analysis algorithm.

6.5 Inverse Analysis Procedure

In the simplified concrete model, different aspects of the load deflection curve are controlled by the various parameters used. By adjusting the parameters manually in ABAQUS, the predicted load-deflection response can be directly compared to the experimental results. The Young's modulus is responsible for the elastic ascending portion of the load deflection curve. The curve showed less sensitivity to Poisson's ratio (υ) so the typical value of 0.30 was used in all tests. The tensile parameter σ_1 corresponds to the point where the load deflection curve deviates from its elastic behavior. Both σ_1 and the first softening slope of the tensile stress-crack width model control the maximum load. Lastly, the remaining post peak tensile stress-crack width parameters (ω_2 σ_2, ω_3, σ_3, ω_4) are responsible for the shape and magnitude of the post peak load deflection response. This method of inverse analysis from a finite element model works equally for round panel and flexural beam models.

Chapter 7

ANALYSIS OF ROUND DETERMINATE PANELS FOR ASTM C1550 TEST SAMPLES

7.1 Introduction

The post-crack behavior of plate-like, fiber-reinforced concrete structural members is well represented by a centrally loaded round panel test specimen that is simply supported on three pivots symmetrically arranged around its circumference. Such a test panel experiences bi-axial bending in response to a central point load and exhibits a mode of failure related to the in situ behavior of structures. The post-crack performance of round panels subject to a central point load can be represented by the energy absorbed by the panel up to a specified central deflection. In this test method, the energy absorbed up to a specified central deflection is taken to represent the ability of a fiber-reinforced concrete to redistribute stress following cracking.

The use of three pivoted point supports in the test configuration results in determinate out-of-plane reactions prior to cracking; however the support reactions are indeterminate after cracking due to the unknown distribution of flexural resistance along each crack. There is also a change in the load resistance mechanism in the specimen as the test proceeds, starting with predominantly flexural resistance and progressing to tensile membrane action around the center as the imposed deflection is increased. The energy absorbed up to a specified central deflection is related to the toughness of the material but is specific to this specimen configuration because it is also determined by the support conditions and size of the specimen. Selection of the most appropriate central deflection to specify depends on the intended application for the material. The energy absorbed up to 5 mm central deflection is applicable to situations in which the material is required to hold cracks tightly closed at low levels of deformation. Examples include final linings in underground civil structures such as railway tunnels that may be required to remain water-tight. The energy absorbed up to 40 mm is more applicable to situations in that the material is expected to suffer severe deformation in situ (for example, shotcrete linings in mine tunnels and temporary linings in swelling ground). Energy absorption up to intermediate values of central deflection can be specified in situations requiring performance at intermediate levels of deformation.

The motivation for use of a round panel with three supports is based on the within-batch repeatability found in laboratory and field experience. The consistency of the failure mode that arises through the use of three symmetrically arranged support pivots results in low within-batch variability in the energy absorbed by a set of panels up to a specified central deflection. The use of round panels also eliminates the sawing that is required to prepare shotcrete beam specimens.

The nominal dimensions of the panel are 75 mm in thickness and 800 mm in diameter. Thickness has been shown to strongly influence panel performance in this test, while variations in diameter have been shown to exert a minor influence on performance. Correction factors are provided to account for actual measured dimensions.

The target dimensions of the panel specimen used in this test are held constant regardless of the characteristics of aggregate and fibers used in the concrete comprising the specimen. Post-crack performance may be influenced by size and boundary effects if large aggregate particles or long fibers are used in the concrete. These influences are acknowledged and accepted in this test method because issues of size effect and fiber alignment arise in actual structures and no single test specimen can suitably model structures of all sizes. Differences in post-crack behavior exhibited in this test method can be expected relative to cast fiber-reinforced concrete members thicker than 100 mm. Because fiber alignment is pronounced in structures produced by shotcreting, and the maximum aggregate size in shotcrete mixtures is typically 10 mm [47], post-crack behavior in specimens tested by this method are more representative of in situ behavior when they are produced by spraying rather than casting concrete.

7.2 Results of FEM and Discussion

In order to compare the finite element model (FEM) to the experimental results the reaction force and displacement at the center of the panel were obtained. The experimental results for select RDP's are shown in Figure 7.2.1. The results show a significant increase in residual capacity with ages from 8 to 11 hours, with less distinctive gains seen in 14 to 17 hour samples. The change in residual load capacity from 24 to 193 hours is not significantly different, with the load-deflection curves being almost identical in the post peak region. However, the maximum load in the 193 hour sample is (+30%), much higher than the 24 hour sample.

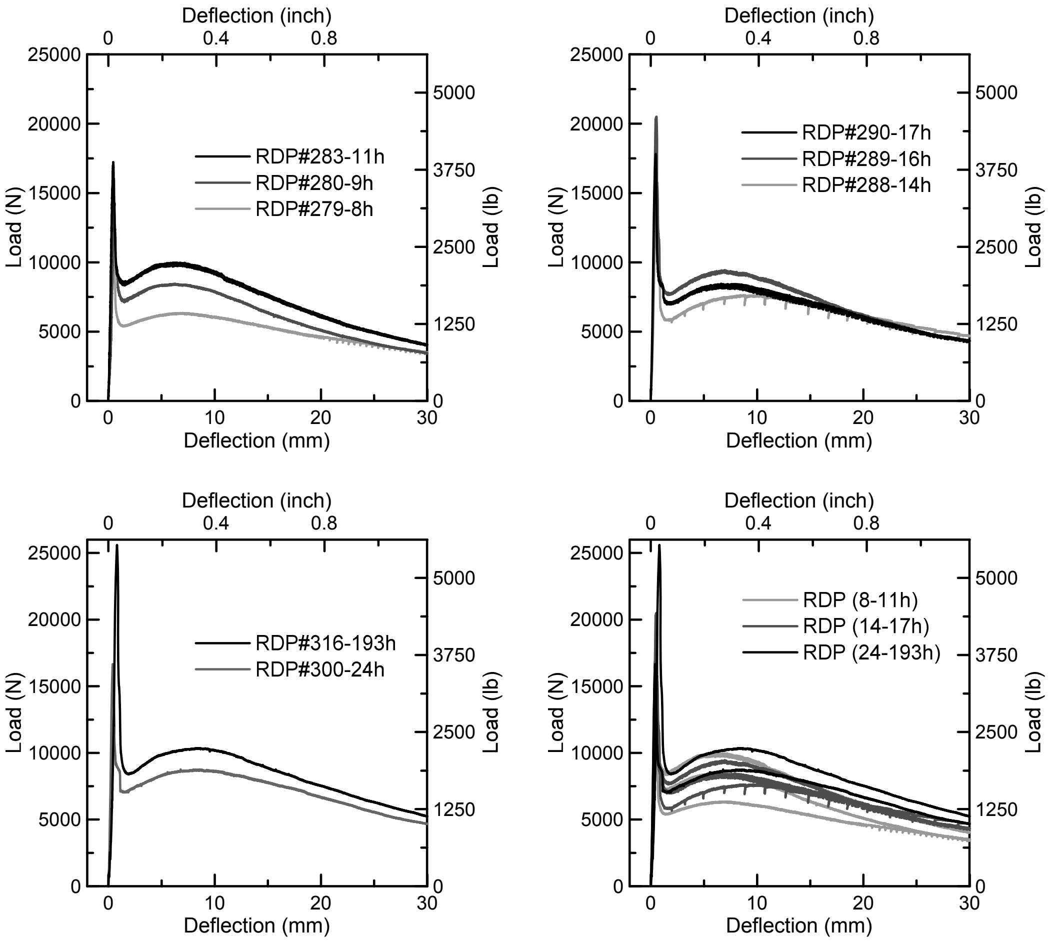

Figure 7.2.1 – Experimental load deflection response for RDP samples as a function of age (8 through 193 hours).

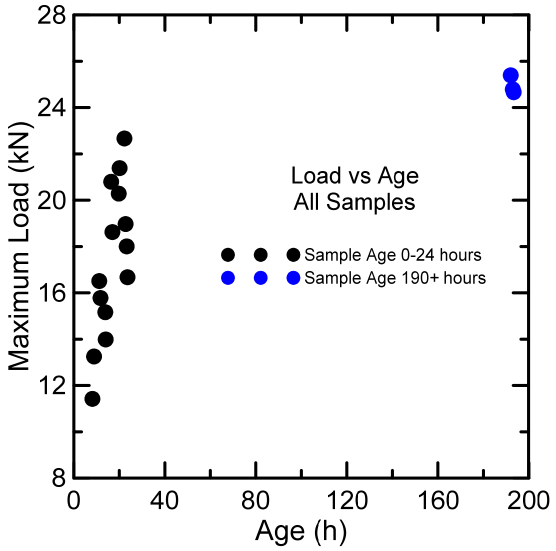

Figure 7.2.2 - FEM load versus age of all samples including outliers at greater than 190 hours.

The input parameters that were used to simulate the load deflection response in the RDP FEM are located in Table 7.2.1 and show an average modulus of elasticity of 19582 MPa with the average peak load for all the samples being 18736 N. Table 7.2.2 displays a direct comparison between the experimental peak load, the FE model peak load and the calculated peak load from yield line theory equation (6.1.6) solved for load (P) as a basic check for model validity. As expected the yield line theory predicts a result that does not consider the pre-stresses due to the self weight of the concrete.

Table 7.2.1 – Summarization of FEM input data and material properties

RDP ID	Age (hr)	Modulus of Elasticity (MPa)	Peak Load (kN)	Defl. @ Peak Load (mm)	ω1 mm	σ1 MPa	ω2 mm	σ2 MPa	ω3 mm	σ3 MPa	ω4 mm	σ4 MPa
279	8.18	23559	11.4	0.27	0	0.79	0.084	0.10	1.80	0.08	2.54	0.069
280	8.9	23559	13.2	0.27	0	0.93	0.094	0.17	1.96	0.12	2.03	0.076
283	11.19	23559	16.5	0.35	0	1.21	0.089	0.24	1.93	0.17	2.29	0.069
284	11.73	22063	15.8	0.35	0	1.14	0.089	0.28	1.91	0.22	2.29	0.083
287	13.84	21546	15.1	0.35	0	1.14	0.086	0.15	1.83	0.10	2.24	0.021
288	14.02	19305	13.9	0.27	0	1.07	0.076	0.17	1.78	0.12	2.54	0.021
289	16.43	19305	20.8	0.35	0	1.72	0.076	0.23	1.78	0.17	2.54	0.021
290	16.96	19305	18.6	0.44	0	1.41	0.102	0.23	1.52	0.17	2.59	0.021
293	19.75	19305	20.2	0.44	0	1.55	0.102	0.23	1.52	0.17	2.59	0.021
294	20.13	19305	21.3	0.44	0	1.66	0.102	0.23	1.52	0.17	2.59	0.021
297	22.25	19305	22.7	0.44	0	1.76	0.114	0.26	1.65	0.19	2.03	0.021
298	22.78	17926	18.9	0.35	0	1.55	0.081	0.19	1.27	0.12	1.78	0.014
299	23.25	17926	18.0	0.35	0	1.45	0.081	0.16	1.27	0.12	1.78	0.014
300	23.6	17823	16.7	0.44	0	1.28	0.089	0.29	1.42	0.21	2.03	0.021
314	192	17823	25.4	0.54	0	2.07	0.102	0.29	1.52	0.24	1.78	0.021
315	192.9	17823	24.8	0.54	0	2.07	0.102	0.21	1.78	0.17	2.03	0.021
316	193.3	13445	24.7	0.54	0	2.28	0.076	0.31	1.52	0.24	2.03	0.034

Table 7.2.2 – Comparison between Experimental, FE Simulation and Yield Line methods of determining peak load for an RDP.

RDP ID	Experimental (kN)	FE Simulation (kN)	Difference (%)	Yield Line (kN)	Difference (%)
279	11.01	11.43	3.82	11.97	8.72
280	13.61	13.26	-2.56	13.89	2.04
283	16.55	16.52	-0.18	17.30	4.53
284	14.75	15.79	7.03	16.53	12.07
287	14.95	15.17	1.49	15.89	6.28
288	13.89	14.00	0.77	14.66	5.52
289	19.62	20.81	6.04	21.79	11.04
290	17.17	18.63	8.52	19.51	13.65
293	19.45	20.29	4.33	21.25	9.26
294	21.47	21.40	-0.35	22.41	4.35
297	21.58	22.68	5.07	23.75	10.03
298	16.70	18.98	13.65	19.88	19.01
299	16.07	18.02	12.10	18.87	17.39
300	15.70	16.68	6.27	17.74	13.00
314	23.70	25.40	7.18	26.60	12.24
315	22.15	24.80	11.95	25.97	17.23
316	23.23	24.67	6.20	25.84	11.22

Figure 7.2.3 shows the simulated versus experimental load deflection curves for select RDP samples. The simulated load deflection response was generated and used to back-calculate the material properties from the experimental data. By manipulating the material properties for each sample, the FEM generated load deflection data can be directly compared and adjusted for best fit responsiveness (see Table 7.2.2). Tensile stress versus crack width results are shown in Figure 7.2.4 which shows the increase in first crack tensile strength (σ_1) with increasing sample age. But as Figure 7.2.2 clearly displays, the majority of the first crack

strength is realized within the first 24 hours. Even when the sample age is in excess of 190 hours only a marginal (+8%) increase in strength is exhibited.

The comparison of the maximum load handling capability of the RDP samples for the three obtained results is summarized in Table 7.2.2. The experimental maximum load was compared to the maximum load obtained from the finite element model, with the average percent difference across all the samples documented as approximately 5 percent. The RDP samples were also analyzed using yield line theory to determine the maximum load and then compared to the experimental values. The average percent difference was approximately 10 percent. This could be expected from yield line theory as this method does not account for the self weight of the sample, irregularities in the material and testing procedure.

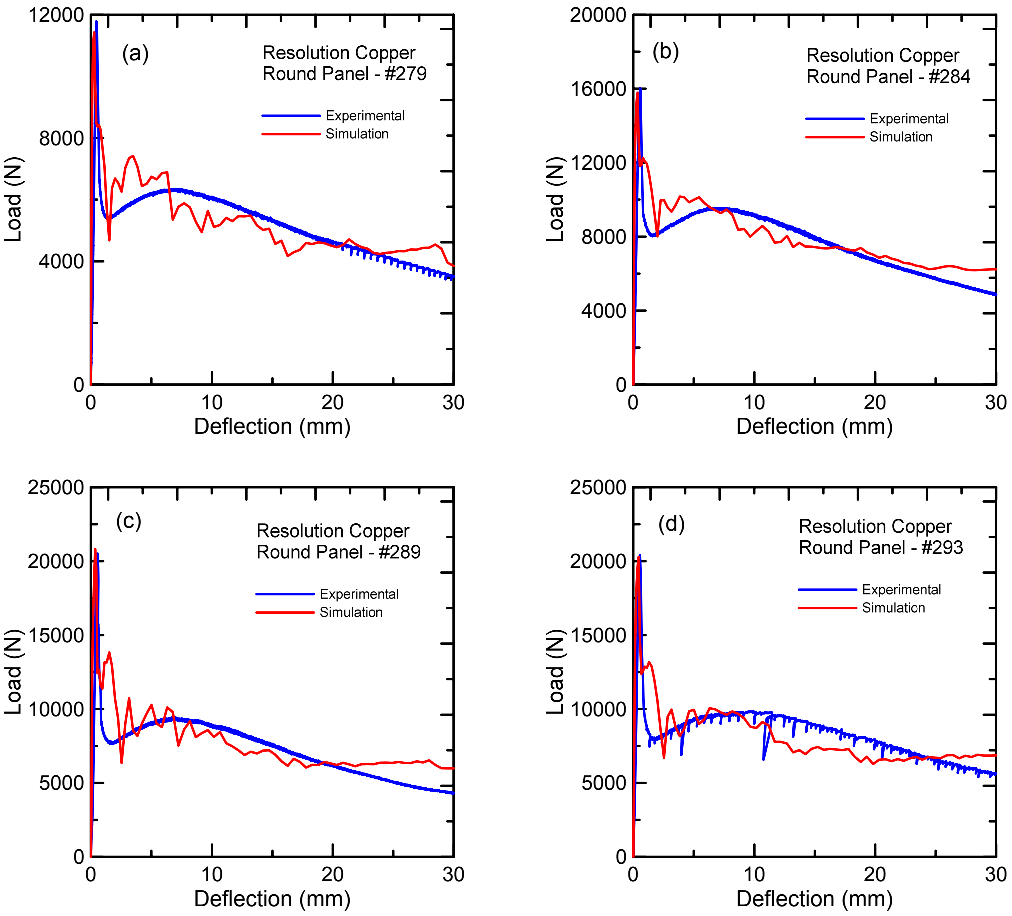

Figure 7.2.3 – Experimental and FEM generated load deflection responses for selected RDP samples.

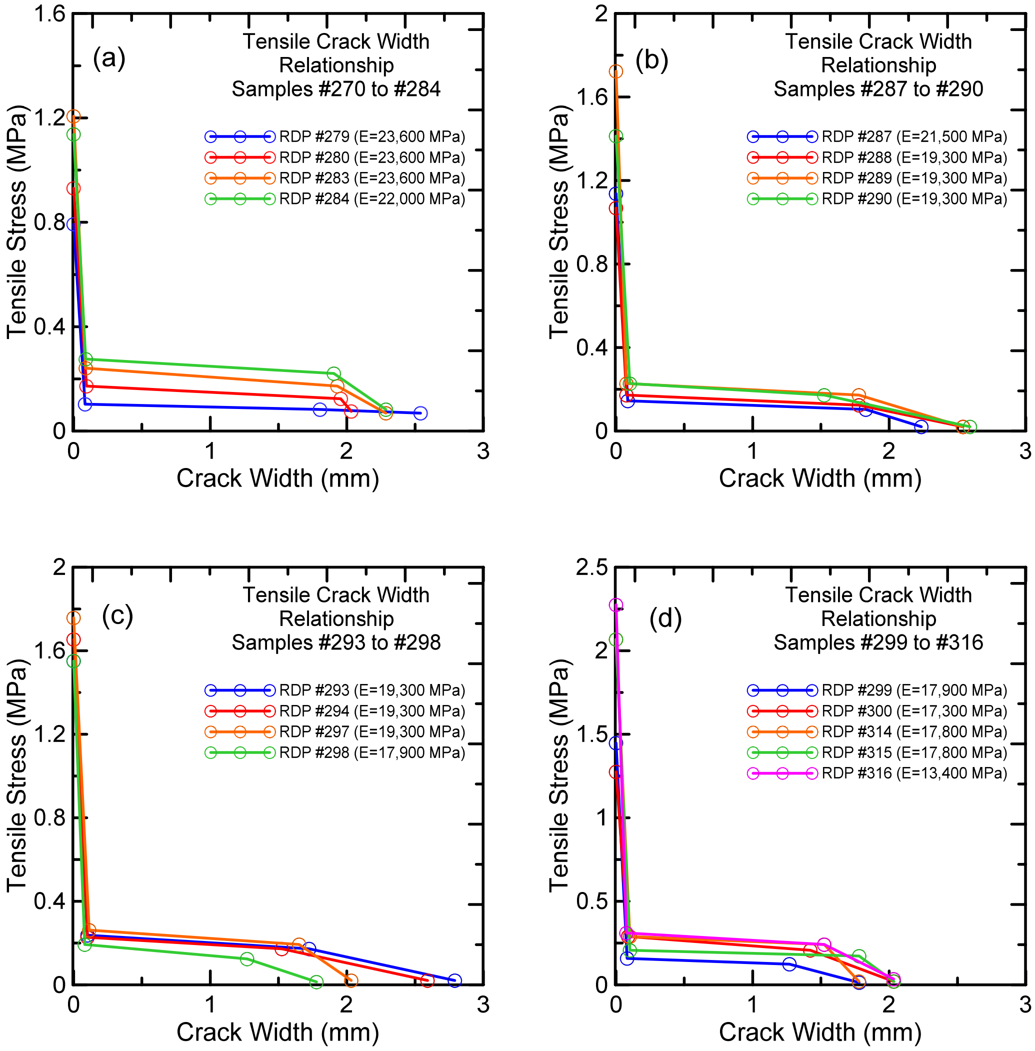

Figure 7.2.4 – The obtained Young's modulus and tensile stress crack width relationship.

By plotting the post peak residual strength as a function of sample age the trend of increasing strength after cracking is demonstrated as expected. This further demonstrates the bridging action of the fibers in the shotcrete matrix as the strain energy is transferred into fiber pullout as opposed to crack propagation. The FEM simulation produced results that closely correlated to the experimental values with an average error of less than one percent. Table 7.2.3 presents this data correlation and includes the percent difference between experimental and FEM simulation.

Table 7.2.3 - Experimental and FEM comparison data for total and post peak residual strength.

Experimental				FEM			
RDP ID	Age (hr)	Total Flexural Toughness (kN.mm)	Residual Flexural Toughness (kN.mm)	Total Flexural Toughness (kN.mm)	Percent Difference (%)	Residual Flexural Toughness (kN.mm)	Percent Difference (%)
279	8.18	226	222	225	-0.44	223	-1.33
280	8.9	198	196	186	-6.06	185	-6.57
283	11.19	267	163	277	3.75	274	2.62
284	11.73	285	180	286	0.35	284	-0.35
287	13.84	220	216	217	-1.36	214	-2.73
288	14.02	251	247	209	-16.73	207	-17.53
289	16.43	269	264	280	4.09	276	2.60
290	16.96	255	250	280	9.80	275	7.84
293	19.75	300	293	293	-2.33	289	-3.67
294	20.13	300	294	303	1.00	299	-0.33
297	22.25	289	284	327	13.15	322	11.42
298	22.78	241	237	239	-0.83	236	-2.07
299	23.25	211	207	215	1.90	212	0.47
300	23.6	259	256	267	3.09	265	2.32
314	192	303	295	310	2.31	303	0.00
315	192.9	289	283	293	1.38	286	-1.04
316	193.3	292	283	296	1.37	289	-1.03

7.3 Moment Distribution in Round Panel Tests (ASTM C-1550)

Understanding the effects of moment distribution in round determinate panels (RDP) allows for a better prediction of the behavior of the FRC under different loading and support conditions, while providing a basis for moment comparisons between alternative testing methods such as three and four point flexural tests.

From finite element models we can analyze the moments as a function of radius along each of the yield lines. In this case, a three symmetrically supported RDP FEM was analyzed in Abaqus. Radial moments (SM2) were taken at specific nodes along each proposed radial yield line to represent the moment as loading progresses. To capture the moment distribution, analysis points (see Figure 7.3.1) were selected to capture the pre-peak, peak and post peak (unloading) material behavior (points A, B and C respectively). The residual strength was captured at points D and E. The moments along each of the three yield lines were averaged to determine a generalized radial moment. Figure 7.3.2 shows the progressive moment distribution as an idealized linear fit through the radius for a selected RDP (RDP #288).

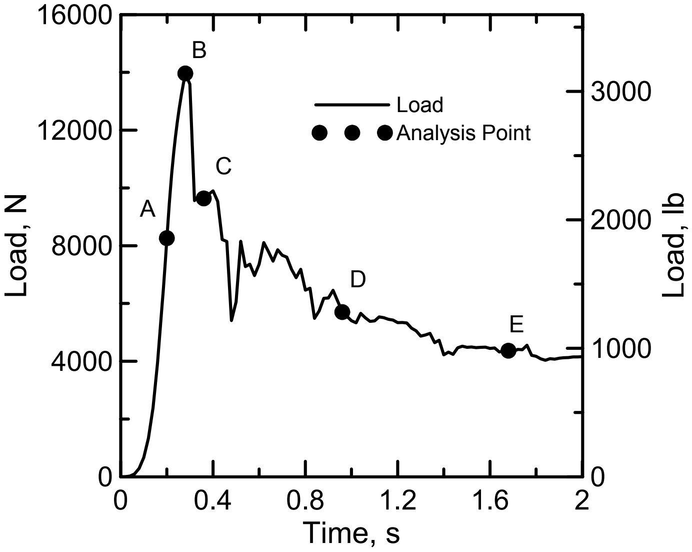

Figure 7.3.1 – Load versus time showing the five analysis points A-E.

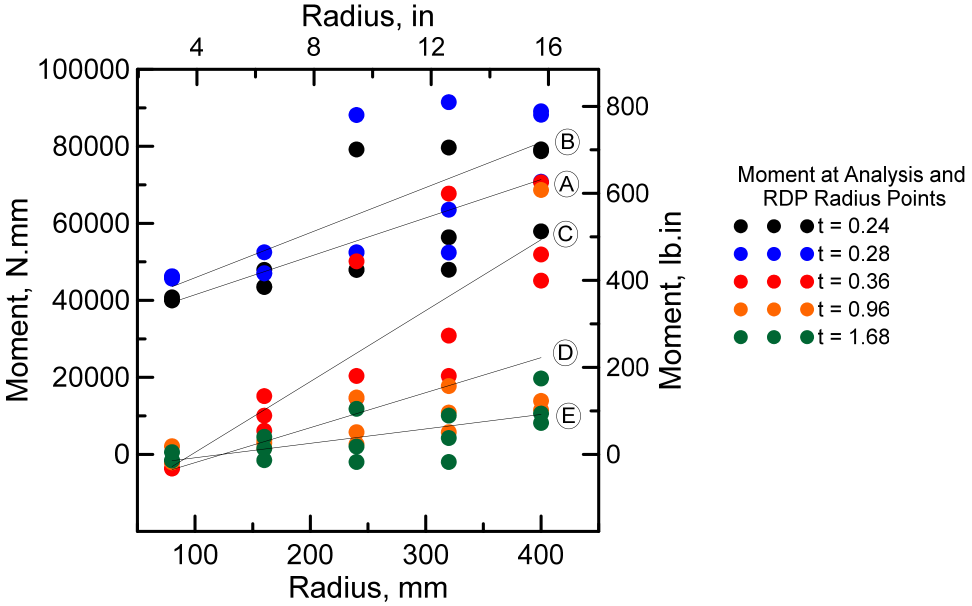

Figure 7.3.2 – Moment distribution as a function of RDP radius at loading points A-E.

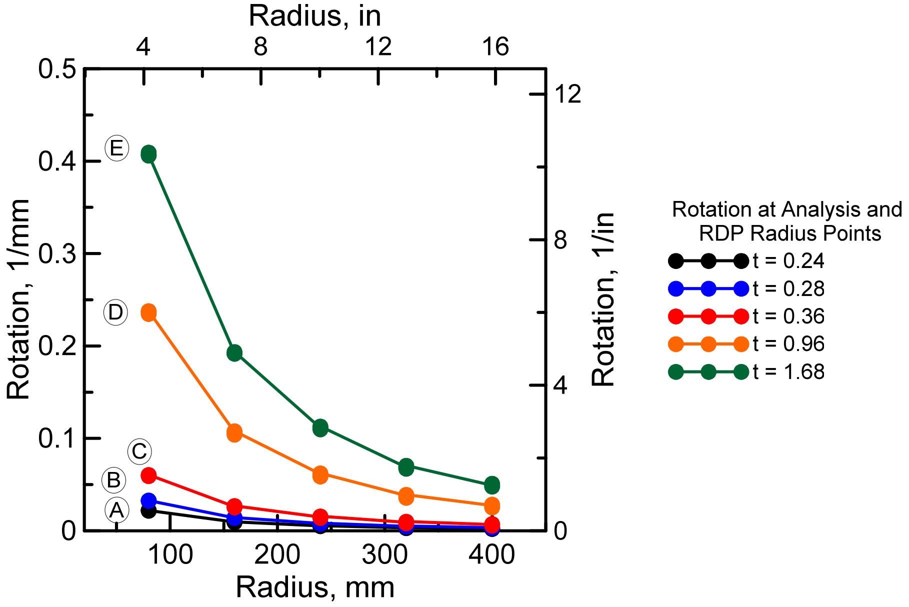

Figure 7.3.3 - Rotation distribution as a function of RDP radius at loading points A-E.

The Figure 7.3.2 clearly shows the increasing moment capacity from pre-cracking (point A) to the maximum load (point B). Once cracking has occurred (point C) there is decrease in the moment capacity, this decrease continues in the residual region as the sample fails (points D and E).

Radial yield lines ideally form symmetrically between the supports as strain energy in the sample increases with loading. Analysis of the geometry of RDP's and the behavior of cracks as the sample fails shows that radial moments at the outer edge of the sample is larger than at the center. Taking the radial moment (SM2) at points along the radius we see that as a function of time the moments are largest at the outer most radius points. Figure 7.3.3 (a-c) shows the moment distribution as a function of time at specific points along each yield line. Radius point one (RP1) corresponds to the point 100 mm from the center of the panel and radius point five (RP5) corresponds to the point at the out edge of the sample at radius of 400mm. Yield line one (figure 7.3.3a) provides a clear picture of how the moment is behaving through loading, including pre, post cracking and residual behavior. Yield line two is exhibiting a large deviation from the expected moment at the RP5, with the moment at RP4 behaving more closely with outer edge behavior. This could be due to excessive deformations in the S4R elements or the un-symmetric nature of where the yield line is forming in the FE model. Yield line three shows typical moment distribution, but a secondary peak is occurring at 0.6 seconds in three of the internal radius points (RP2, 3 and 4). Again, inconsistencies in location of yield line formation could be the cause.

It is interesting to note that this secondary spike in load capacity type behavior is typical during fiber pull-out of fabrics. Once a crack has formed, strain energy goes into de-bonding the fabric from the cement matrix, once the fabric yields we see a period of unloading, then re-loading as the next set of exposed fibers in the fabric pull out.

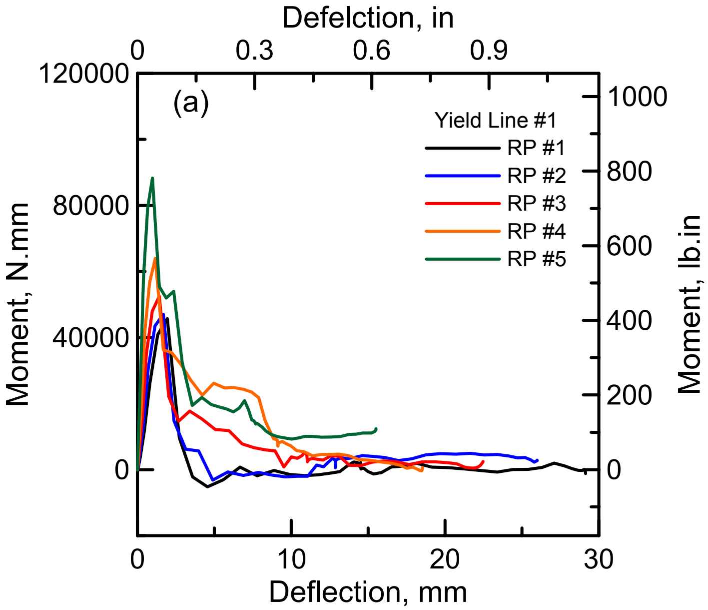
Defelction, in
0
0.3
0.6
0.9
120000
80000
40000
0
1000
800
600
400
200
0
(a)
Yield Line #1
RP #1
RP #2
RP #3
RP #4
RP #5
Moment, N.mm
Moment, lb.in
0
10
20
30
Deflection, mm

(a)

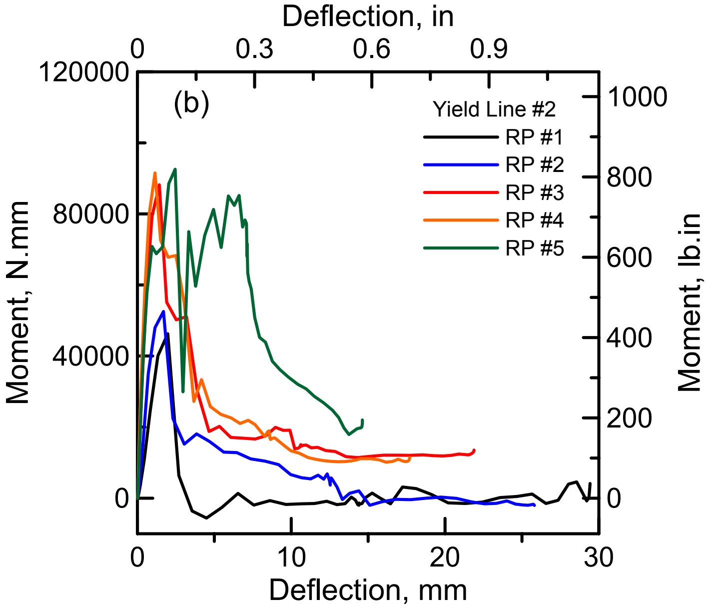
Deflection, in
0
0.3
0.6
0.9
120000
80000
40000
0
1000
800
600
400
200
0
(b)
Yield Line #2
RP #1
RP #2
RP #3
RP #4
RP #5
Moment, N.mm
Moment, lb.in
0
10
20
30
Deflection, mm

(b)

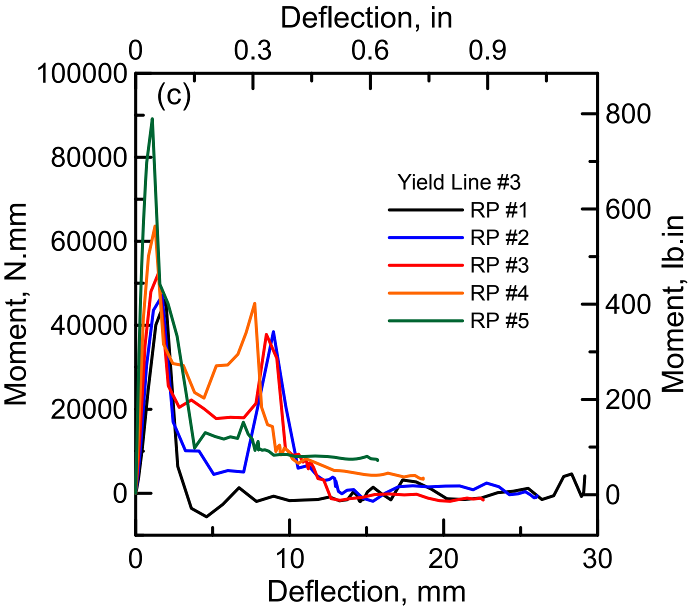

(c)

Figure 7.3.3 (a-c) – Moment distributions at 5 radius points (RP) for three yield lines.

To ascertain further validity that the moment distributions along the yield lines are reasonable, a check for equilibrium must be done. By taking a segment of the round panel as shown in Figure 7.3.4 the sum of the incremental moments at each radius point along each of the yield lines must equal (or approximate) one third the reaction force captured at the center of the panel. By taking the incremental moment at each radius point and dividing the moment by the length of each radius point, the incremental load is summed for each yield line per equation (7.3.1)

$$\frac{P_{center}}{3} = \sum \frac{M_{i,YL1}}{RP_{i,YL1}} + \sum \frac{M_{i,YL2}}{RP_{i,YL2}} \tag{7.3.1}$$

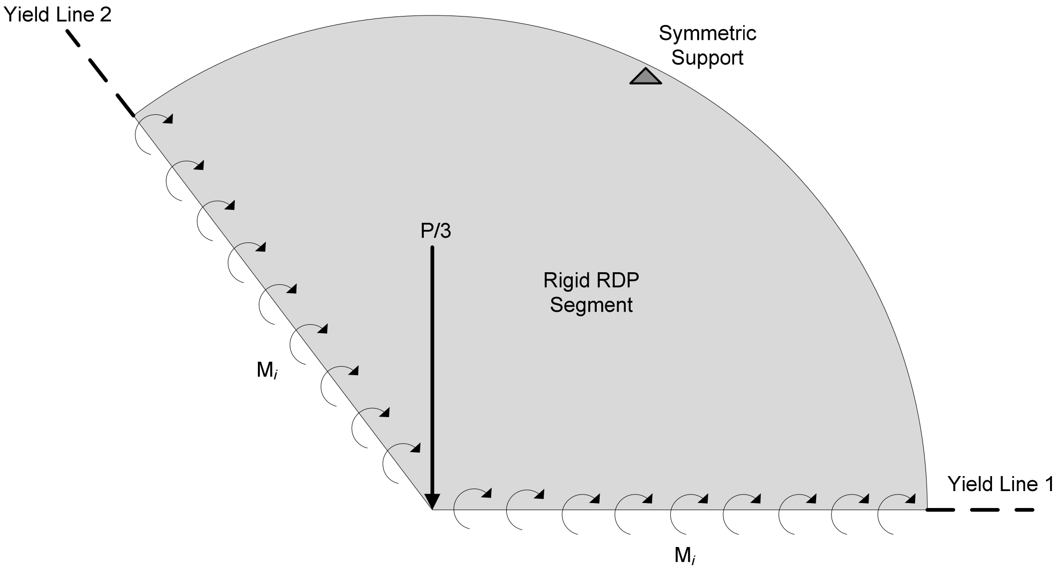

Figure 7.3.4 – One third section for determining equilibrium.

Table 7.3.1 shows the comparison with the maximum moment derived force with the maximum reaction force at the center for each of the three rigid segments.

Table 7.3.1 – Comparison of maximum moment derived loads with maximum reaction force.

	Seg 1	Seg 2	Seg 3	RF/3
Max (N)	4377	4387	4082	4656

The derived loads are within 5-12% of the reaction force captured at the center of the panel. This is within tolerable bounds for a two dimensional finite element model. Accuracy could be increased with a variety of measures including finer meshes, smaller time steps of incremental displacement or full three dimensional analyses.

7.4 ASTM C-1609 and ASTM C-1550 Correlation

In order to predict the load deflection response of a round panel test, moment curvature relationship of a panel and the size of a crack band width must be provided as an input. This information can be obtained directly from the yield line of a round panel test on 3 supports through experimental or finite element model. Another possible source is to compare the normalized toughness of a round panel with a four point bending sample. If the normalized toughness response from the four point bending test can be used to successfully predict the absorbed energy of a round panel test, there is no need to conduct an expensive round panel tests at all.

Toughness is described as the area under the load defection response curve and for a round determinate panel test (ASTM C-1550) toughness is expressed as energy absorbed at 5mm, 10mm, 20mm and 40mm in Joules (N.m). When a material sample is under loading conditions strain energy builds locally at the surface until cracking occurs. Once cracking occurs this strain energy is released in form of new surfaces (cracks) and in fiber reinforced composites, fiber pull-out. In comparing four and three point bending samples is it common to normalize the flexural toughness with respect to the cross-sectional area of the samples. A sample with a larger cross section will ultimately absorb more energy before cracking occurs and normalizing this property yields a way of comparing baseline material behavior without the effect of sample geometry. This idea of normalized toughness can be applied to round panels in effort to draw a correlation between the ASTM C-1609 and C-1550.

Table 7.4.1 shows the experimental four-point bending results including the total flexural toughness at 3mm of deflection for 75 C-1609 results. The toughness is divided by cross section dimensions and a normalized toughness (G'F) expressed in units of N/mm is achieved.

Table 7.4.1 – Comparison of toughness, cross section dimensions and normalized toughness.

Beam ID	Flexural Toughness @ 3mm, (GF) N-mm	b, mm	d, mm	Normalized Toughness, G'F N/mm
155	30846	150	150	1.371
156	31407	150	150	1.396
157	38714	150	150	1.721
158	41318	150	150	1.836
160	43674	150	150	1.941
161	38848	150	150	1.727
162	35553	150	150	1.580
164	46487	150	150	2.066
168	46351	150	150	2.060
169	61247	150	150	2.722
170	55813	150	150	2.481
171	54752	150	150	2.433
192	19526	150	150	0.868
194	28575	150	150	1.270
195	28575	150	150	1.270
196	34741	150	150	1.544
198	66200	150	150	2.942
199	58643	150	150	2.606
200	62929	150	150	2.797
201	27067	150	150	1.203
202	27454	150	150	1.220
203	30728	150	150	1.366
204	42933	150	150	1.908

205	37163	150	150	1.652
207	26222	150	150	1.165
208	31071	150	150	1.381
209	32605	150	150	1.449
210	28796	150	150	1.280
211	35195	150	150	1.564
212	20086	150	150	0.893
213	38919	150	150	1.730
214	26944	150	150	1.198
216	35461	150	150	1.576
217	29145	150	150	1.295
218	32222	150	150	1.432
219	36296	150	150	1.613
220	39083	150	150	1.737
221	42540	150	150	1.891
222	43308	150	150	1.925
225	33477	150	150	1.488
226	37552	150	150	1.669
227	29254	150	150	1.300
228	32960	150	150	1.465
230	31251	150	150	1.389
231	36626	150	150	1.628
232	23786	150	150	1.057
233	24949	150	150	1.109
234	47277	150	150	2.101
235	45936	150	150	2.042
236	40072	150	150	1.781
262	44178	150	150	1.963
263	23083	150	150	1.026
264	26506	150	150	1.178
265	30468	150	150	1.354
267	35706	150	150	1.587
269	38119	150	150	1.694
270	34309	150	150	1.525
271	32724	150	150	1.454
272	35049	150	150	1.558
273	61119	150	150	2.716
274	58165	150	150	2.585
275	47877	150	150	2.128
276	35943	150	150	1.597
277	40810	150	150	1.814
278	56890	150	150	2.528
301	26029	150	150	1.157

302	35691	150	150	1.586
304	32857	150	150	1.460
306	54267	150	150	2.412
308	40770	150	150	1.812
309	41444	150	150	1.842
310	11240	150	150	0.500

Round determinate panels results can be used to provide an RDP’s normalized toughness up through a maximum deflection of 40mm. ASTM C-1550 has the toughness (energy absorbed) reported as work (W) at deflections of 5mm, 10mm, 20mm and 40mm. It is important to note that RDP’s can experience more or less that the assumed 3 crack failure pattern, with 2 or 4 cracks occurring under un-ideal conditions where strain energy is not uniformly distributed. To determine if a crack is contributing to the dissipation of strain energy it must be functioning as a plastic hinge. In some cases 3 cracks form, but it is observed that 2 are major cracks and 1 is a minor crack (<0.5mm), in this case only two cracks are functioning as plastic hinges through loading. In these cases it is noted that total toughness values are smaller than when 3 fully functioning cracks are observed. Normalized toughness in round panels is determined from the experimental absorbed energy data. Table 7.4.2 shows the dimensions and number of cracks that were observed in the RDP’s at failure. The normalized toughness is determined by equation (7.1)

$$W' = \frac{W}{R.t.\xi} \qquad (7.4.1)$$

Where *W* is the energy absorbed at a specific RDP deflection, *R* is the radius, *t* is the sample thickness and ξ is the number of radial cracks.

Table 7.4.2 – RDP geometric and normalized toughness data at deflections of 5mm, 10mm, 20mm and 40mm

RDP ID	Radius (mm)	Thickness (mm)	Radial Cracks	W’ (5 mm)	W’ (10 mm)	W’ (20 mm)	W’ (40 mm)
279	406	77	3	0.350	0.712	1.325	2.146
280	407	76	3	0.449	0.920	1.664	2.452
283	408	76	4	0.536	1.084	1.949	2.890
284	408	77	4	0.525	1.073	2.003	3.153
287	408	76	4	0.383	0.766	1.456	2.354
288	408	76	4	0.394	0.821	1.609	2.682
289	405	76	3	0.504	1.029	1.894	2.890
290	402	76	3	0.449	0.920	1.719	2.704
293	407	76	3	0.525	1.095	2.102	3.404
294	411	76	3	0.580	1.149	2.102	3.251
297	407	78	3	0.668	1.346	2.408	3.569
298	408	76	3	0.449	0.898	1.708	2.813
299	408	76	3	0.416	0.821	1.554	2.485
300	407	77	3	0.460	0.963	1.861	2.967
314	407	78	3	0.690	1.357	2.354	3.404
315	406	80	3	0.569	1.117	2.091	3.306
316	406	78	3	0.591	1.215	2.255	3.525

Because the ASTM standard for round panel testing uses the energy absorbed at the given deflections as a measure of the performance of the fiber reinforced composite, it is critical that the four-point bend data be a good predictor of energy absorbed at each stage of RDP deflection. By comparing the four-point bending normalized toughness (G’F) with the W’ values at each RDP deflection stage a correlation begins to emerge. These results were plotted and linear best fit equations applied, see Figure 7.4.1.

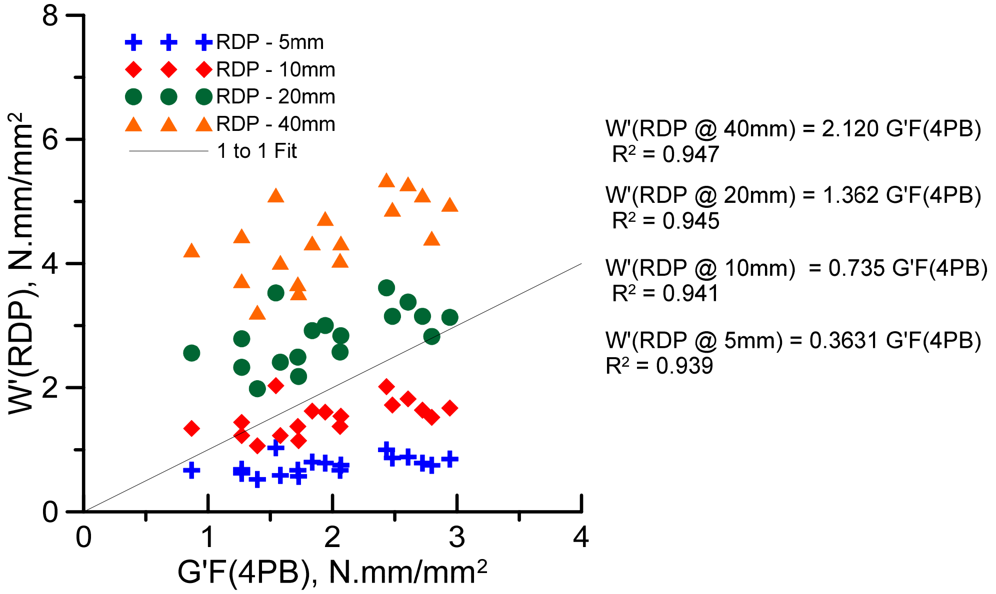

Figure 7.4.1 – Normalized absorbed energy correlation between four point bending and RDP tests.

Now that a correlation is established, the normalized toughness (G’F) from the four point bend test can be located on the x-axis of Figure 7.4.1. If a vertical line is drawn, the intersection with each RDP deflection-energy equation is the equivalent normalized RDP energy absorbed for that specific deflection. The best fit equations are given in Figure 7.4.1, which numerically equates the RDP W’ values to the four point bending values of G’F.

7.5 Conclusion

While this technique doesn’t completely replace the need for round determinate panel tests, it does present a way of test correlation. Once an energy absorption trend is established by a number of C-1550 tests, they can be given way in lieu of

C1609 tests which can be used to represent the RDP energy absorbed. If mix design changes in way to affect the behavior of the FRC under loading conditions, a new batch of RDP's with the new mix design would need to be completed to establish the absorbed energy template and new fit equations produced. In this case, 15 RDP's were used to develop the correlation. The coefficient of correlation (R^2) produced values above 0.90, providing a strong experimental relationship.

Chapter 8

DEVELOPMENT OF TOUGHNESS BASED DESIGN GUIDELINES FOR FIBER REINFORCED CONCRETE

8.1 Introduction

Fiber reinforced concrete (FRC) is a composite material consisting of cementitious matrix and discrete fibers such as steel, glass, or other synthetic materials. The fibers that are randomly distributed in the matrix act as crack arrestors. The deboning and pulling of fibers at crack surface requires energy dissipation, leading to a substantial increase in toughness and resistance to cyclic and dynamic load [48]. Since the introduction of fibers to the concrete market in late 1960's, the demand for FRC has been steadily increased. The main areas of applications are slab on grade, tunnel lining, precast, and pre-stressed concrete products. Flat slabs made solely of SFRC has been successfully practiced in France and other European countries, however their applications in the United States have been limited [49,50]. It is expected that more FRC applications in new structural areas are forthcoming.

Using the tools, models and simulations in previous sections the implementation of model parameters into design procedures can be realized. Specifically the development of the ultimate design moment equation based on geometry, compressive strength, residual strength parameters for each of the design standards (ASTM, JCI and RILEM) and the residual strength correction factor from the described tri-linear material model. The design procedures are primarily based on the work of Soranakom and Mobasher [51], ACI 318-05 [52] and RILEM TC 162-TDF [53].

8.2 Development of Design Equations

The design equations are presented with a minimum number of independent variables and dimensionless parameters. Cracking tensile strength and Young's modulus can be estimated according to ACI-318 [52] Sec. 11.2 and Sec. 8.5.1, respectively.

$$\sigma_{cr} = E\varepsilon_{cr} = 6.7\sqrt{f_c^{'}} \quad \text{(psi)} \quad (\text{or} = 0.56\sqrt{f_c^{'}} \quad \text{(MPa)}) \tag{8.1}$$

$$E = 57,000\sqrt{f_c^{'}} \quad \text{(psi)} \quad (\text{or} = 4,733\sqrt{f_c^{'}} \quad \text{(MPa)}) \tag{8.2}$$

Cracking tensile strain for FRC members can be calculated from Hooke's law as:

$$\varepsilon_{cr} = \frac{\sigma_{cr}}{E} = \frac{6.7\sqrt{f_c^{'}}}{57000\sqrt{f_c^{'}}} = \frac{0.56\sqrt{f_c^{'}}}{4733\sqrt{f_c^{'}}} = 118\ \mu str \tag{8.3}$$

Tensile stress-strain model can also be obtained directly from uniaxial tension test. However, the test procedure is difficult to control and normally under-predicts the flexural strength due to the size effect between uniform stress in direct tension test and gradient stress in bending test [51,54,55,56]. To predict flexural behaviors, the back calculation of tensile properties from load-deflection curve of the four point bending test is an option which indirectly incorporates the size effect in material properties.

The yield compressive strength parameters $\sigma_{cy} = 0.85f_c'$ from RILEM [53] is adopted here, where f_c' is the ultimate uniaxial cylinder compressive strength. By applying a typical value for yield compressive strain $\omega=0.85(f_c')^{0.5}/6.7$, the cracking moment $M_{cr}=\sigma_{cr}bh^2/6$ and $M=M'M_{cr}$ as described in Equation (2.5) from Chapter 2, the expression for nominal moment capacity as a function of its post crack tensile strength, μ and ultimate compressive strength, f_c', is obtained as:

$$M_{ult}=\left[\frac{\mu\sqrt{f_c'}}{15.8\mu+2\sqrt{f_c'}}\right]bd^2E\varepsilon_{cr} \tag{8.4}$$

As outlined in a previous chapter ASTM, JCI-SF4 and RILEM TC 162-TDF over estimate the residual strength which has a direct effect in design applications. The correction factors given in section 3.9.1, 3.9.2 and 3.9.3 are incorporated into equation (17) and standard specific design equations are established.

$$M_{ult}=\left[\frac{\xi\sqrt{f_c'}}{15.8\xi+2k_{bt}\sqrt{f_c'}}\right]bd^2E\varepsilon_{cr} \tag{8.5}$$

Where ξ is the standard residual parameter (ARS, σ_b, $f_{eq,3}$) for ASTM, JCI or RILEM standards respectively and k_{bt} is the correction factor given as $(1/k_{bt})$ in section 3.9. for each respective standard.

8.3 Design Example for Slab on Grade

The design procedure for strain softening fiber reinforced concrete is best suited for thin structural applications such as slab systems that the size effect is minimal and the internal forces are relatively low compared to its moment capacity. An example of slab on grade is presented to demonstrate the design calculations. Typically, slabs on grade are designed based on minimum shrinkage and temperature steel. The loads on slab are not critical and normally transferred directly to stiff compacted base materials. These slabs are allowed to cracks but not disintegrate. Other types of slab on grade and pavement that are designed based on applied load and sub grade modulus are not considered here.

8.3.1 Design Problem

Consider a concrete slab five inches thick, reinforced at mid depth with steel rebar #4@18” (12.7 mm @ 457 mm). The materials used are: concrete compressive strength f_c' of 3,000 psi (20.7 MPa) and steel yield strength f_y of 60 ksi (414 MPa). Replace this existing design with SFRC that has compressive strength f_c' of 4000 psi (27.6 MPa). The slab is designed based on 1 foot strip (254 mm) and the amount of reinforcement A_s is calculated by:

$$A_s = \frac{\pi d^2}{4}\frac{12}{spacing} = \frac{\pi 0.5^2}{4}\frac{12}{18} = 0.131\ \frac{\text{in}^2}{\text{ft}}\ \text{(or 277 mm}^2\text{/m)}$$

Calculate the plastic compressive zone according to ACI stress block concept

$$a = \frac{A_s f_y}{0.85 f_c' b} = \frac{0.131 \times 60}{0.85 \times 3 \times 12} = 0.257$$

The factored ultimate moment M_u is equal to the reduced nominal moment capacity $\phi_b M_n$

$$M_u = \phi_b M_n = \phi_b A_s f_y \left(d - \frac{a}{2} \right)$$

$$= 0.9 \times 0.131 \times 60(2.5 - \frac{0.257}{2})\frac{1}{12} = 1.40 \text{ kips-ft/ft (or 6.23 kN-m/m)}$$

8.3.2 Equivalent Moment Capacity

Equivalent moment capacity with SFRC, f_c' = 4000 psi (27.6 MPa).

Calculate the cracking tensile strength of SFRC according to Eq. (8.1)

$$\sigma_{cr} = 6.7\sqrt{f_c'} = 6.7\sqrt{4000} = 424 \text{ psi (2.92 MPa)}$$

Calculate the cracking moment according to Eq. (2.5)

$$M_{cr} = \frac{\sigma_{cr} b h^2}{6} = \frac{424 \times 12 \times 5^2}{6}\frac{1}{12000} = 1.77 \text{ kips-ft/ft (or 7.87 kN-m/m)}$$

The compressive – tensile strength ratio (ω) is taken from the model parameters. Here we will assume this value to be;

$$\omega = 8.02$$

It can be verified by Eq. (8.4) that the reduced nominal moment capacity $\phi_b M_n$ of the SFRC slab is equal to the ultimate moment M_u determined from the reinforced concrete slab.

$$M_{ult} = \left[\frac{\xi\sqrt{f_c'}}{15.8\xi + 2\psi\sqrt{f_c'}}\right] bd^2 E\varepsilon_{cr}$$

Using the residual strength correction factors we can use Table 8.3.1 to summarize the design parameters based on residual strength.

Table 8.3.1 Residual strength parameter summary for design.

Standard	Residual Parameter	Residual Strength Value	k_{bt}
ASTM C1609	f^D_{150}	216	2.94
RILEM TC 162-TDF	$f_{eq,3}$	218	3.10
JCI-SF4	σ_b	229	3.22

$$f^D_{150} = 2.94\mu\sigma_{cr} \tag{8.3.1}$$

$$f_{eq,3} = 3.10\mu\sigma_{cr} \tag{8.3.2}$$

$$\sigma_b = 3.22\mu\sigma_{cr} \tag{8.3.3}$$

For ASTM with an ARS (or f_{150}) value = 216 psi

$$= \left[\frac{216\sqrt{4000}}{15.8(216)+2(2.95)\sqrt{4000}}\right]0.7(424)(12)(5)^2\frac{1}{12000} = 26.77 \textit{ kips-ft/ft}$$

For JCI with a σ_b value = 218 psi

$$= \left[\frac{218\sqrt{4000}}{15.8(218)+2(3.08)\sqrt{4000}}\right]0.7(424)(12)(5)^2\frac{1}{12000} = 26.68 \textit{ kips-ft/ft}$$

For RILEM with an $f_{eq,3}$ value = 229 psi

$$= \left[\frac{229\sqrt{4000}}{15.8(229)+2(3.11)\sqrt{4000}}\right]0.7(424)(12)(5)^2\frac{1}{12000} = 26.79 \textit{ kips-ft/ft}$$

8.4 Conclusion

It is critical to recognize the use of residual strength in the design of structural members. The overestimation in residual strength by current standards causes an overestimation in ultimate moment capacity. Through the design example given in section 8.3 we can see the applicability of the residual strength correction factor as it applies to the design moment equation. By incorporating the correction factor, the equivalent design moment will not be overestimated allowing the design strength to be within the material's bearing capabilities.

REFERENCES

1 Henager, CH. New Developments in Steel Fibrous Shotcrete, Concrete Construction March 1980.

2 Goodfellow, RJF. Concrete for underground structures, Society for mining, metallurgy and exploration. Englewood, CO, 2011.

3 ASTM C1609-10, “Standard Test Method for Flexural Performance of Fiber-Reinforced Concrete (Using Beam With Third-Point Loading)”, ASTM Standard Book, V. 04.02, 2010.

4 RILEM TC 162-TDF, RILEM final recommendations on test and design methods for steel fibre reinforced concrete: bending test, Materials and Structures, 2002;35:579-582.

5 Japanese Concrete Institute, JCI-SF4, Methods of tests for flexural strength and flexural toughness of fiber reinforced concrete (using beam with third-point loading). 1984: 45–56.

6 di Prisco M, Plizzari G, Vandewalle L. Fibre reinforced concrete: new design perspectives. Mater Struct 2009;42(9):1261–81.

7 Walraven J. High performance fiber reinforced concrete: progress in knowledge and design codes. Mater Struct 2009;42(9):1247–60.

8 Mindess, S., Young, J.F., and Darwin, D. (2003), Concrete, Second Edition, Prentice-Hall, Upper Saddle River, NJ.

9 Bentur, A. and Mindess, S. (1990). “Fibre Reinforced Cementitious Composites.” Elsevier Applied Science, London.

10 Belletti B, Cerioni R, Meda A, Plizzari G. Design aspects on steel fiber-reinforced concrete pavements. J Mater Civ Eng 2008;20(9):599–607.

11 Sorelli LG, Meda A, Plizzari GA. Steel fiber concrete slabs on ground: a structural matter. ACI Struct J 2006;103(4):551–8.

12 Pelisser F, Santos Neto AB, La Rovere HL, Pinto RCA. Effect of the addition of synthetic fibers to concrete thin slabs on plastic shrinkage cracking. Construction and Building Materials 24 (2010) 2171–2176.

13 Mobasher B. Mechanics of fiber and textile reinforced cement composites. 1st ed. (2011) p. 420 CRC Press; Boca Raton, FL.

14 Mobasher, B. and Li, C. Y., "Mechanical Properties of Hybrid Cement Composites," ACI Materials Journal, Vol. 93, No.3, pp.284-293, 1996.

15 Ferrara L, Meda A. Relationships between fibre distribution, workability and the mechanical properties of SFRC applied to precast roof elements. Mater Struct/Mat et Constr 2006;39(288):411–20.

16 Gettu R, Barragán B, Garcia T, Ortiz J, Justa R. Fiber concrete tunnel lining. Concr Int 2006;28(8):63–9.

17 Bernard E. Correlations in the behaviour of fibre reinforced shotcrete beam and panel specimens. Mater Struct 2002;35(3):156–64.

18 Malhotra V M, Carette AGG, Bilodeau A. Mechanical Properties and durability of polypropylene fiber reinforced high-volume fly ash concrete for shotcrete applications. ACI Materials Journal, 91(5);478-486.

19 Armelin HS, Helene P. Physical and Mechanical Properties of Steel-Fiber Reinforced Dry-Mix Shotcrete. ACI Materials Journal. 92(3);258-267.

20 Morgan DR. Steel fiber reinforced shotcrete for support of underground openings in Canada. Concrete International, 13(11): 56-64.

21 Banthia N, Trottier JF, Wood D, Beaupre D. Influence of fiber geometry in steel fiber reinforced dry-mix shotcrete. Concrete International, 14(5):24-28.

22 American Concrete Institute. State of the art report on fiber reinforced shotcrete, 506.1R-98(1998). AC1 Committee 506, American Concrete Institute, Detroit, MI.

23 Glassfibre Reinforced Concrete: practical design and structural analysis / Publisher Beton-Verlag, Düsseldorf : 1995.

24 Sukontasukkul P, Pomchiengpin W, Songpiriyakij S. Post-crack (or post-peak) flexural response and toughness of fiber reinforced concrete after exposure to high temperature. Construction and Building Materials 24 (2010) 1967–1974.

25 Sueki S, Soranakom C, Mobasher B, Peled A, Pullout-Slip Response of Fabrics Embedded in a Cement Paste Matrix, ASCE Journal of Materials in Civil Engineering, Vol. 19, No. 9, September 1, 2007.

26 Li C Y, Mobasher B. Finite element simulations of fiber pullout toughening in fiber reinforced cement based composites. Advn Cem Bas Mat 1998;7:123–132.

27 Roesler, J. and Gaedicke, C. (2004), “Fiber reinforced concrete for airfield rigid pavements,” Technical Note 3 - Center of Excellence for Airport Technology (CEAT), Urbana, IL, October 2004, 11 pp.

28 Buratti N., Mazzotti C., Savoia M. Post-cracking behaviour of steel and macro-synthetic fibre-reinforced concretes. Construction and Building Materials 25 (2011) 2713–2722.

29 Soulioti DV, Barkoula NM, Paipetis A, Matikas TE. Effects of fibre geometry and volume fraction on the flexural behaviour of steel-fibre reinforced concrete. Strain (2011) 47, e535–e541.

30 Soranakom C, Mobasher B. Closed form solutions for flexural response of fiber reinforced concrete beams. Journal of Engineering Mechanics 2007;133(8):933-41.

31 Soranakom C, Mobasher B. Closed-form moment-curvature expressions for homogenized fiber-reinforced concrete. ACI Material Journal 2007; 104(4):351-9.

32 Soranakom C, Mobasher B, Bansal S. Effect of material non-linearity on the flexural response of fiber reinforced concrete. Proceeding of the Eighth International Symposium on Brittle Matrix Composites BMC8, Warsaw, Poland, 2006:85-98.

33 Soranakom C, Mobasher B. Correlation of tensile and flexural responses of strain softening and strain hardening cement composites. Cement & Concrete Composites Vol. 30, 2008, pp. 465–477.

34 Soranakom C, Mobasher B. Flexural Analysis and Design of Textile Reinforced Concrete. 4th Colloquium on Textile Reinforced Structures (CTRS4), Dresden, Germany, June 3-5 2009, pp. 273-288.

35 Koeberl B, Willam K. Question of Tension Softening versus Tension Stiffening in Plain and Reinforced Concrete. ASCE Journal of Enginering Mechanics, Vol. 134 (9), 804-804.

36 Bakhshi M, Barsby C, Mobasher B, "Comparative Evaluation of Early Age Toughness Parameters in Fiber Reinforced Concrete", Submitted to Materials and Structures, 2011.

37 Altoubat, S., Roesler, J., and Rieder, K.-A. (2004), "Flexural Capacity of Synthetic Fiber Reinforced Concrete Slabs on Ground Based on Beam Toughness Results", accepted to Sixth RILEM Symposium on Fiber Reinforced Concretes, Varenna-Lecco, Italy.

38 Barros, J. A. O., Cunha, V. M. C. F., Ribero, A. F., and Antunes, J. A. B. Postcracking behaviour of steel fibre reinforced concrete, Materials and Structures, Vol. 37, 2004.

39 fib (2010). "Model Code 2010 - First complete draft, Vol. 1", Bulletin 55, 220–231.

40 Altoubat, S., Roesler, J., and Rieder, K.-A. (2004), "Flexural Capacity of Synthetic Fiber Reinforced Concrete Slabs on Ground Based on Beam Toughness Results", accepted to Sixth RILEM Symposium on Fiber Reinforced Concretes, Varenna-Lecco, Italy.
41 fib (2010). "Model Code 2010 - First complete draft, Vol. 1", Bulletin 55, 220–231.

42 Soranakom C, Mobasher B, Bansal S. Effect of material non-linearity on the flexural response of fiber reinforced concrete. Proceeding of the Eighth International Symposium on Brittle Matrix Composites BMC8, Warsaw, Poland, 2006:85-98.

43 Maalej M, Li VC. Flexural/tensile-strength ratio in engineeredcementitious composites. J Mater Civil Eng 1994;6(4):513–28.

44 Li VC. From micromechanics to structural engineering- the design of cementitious composites for civil engineering applications.StructEng Earthquake Eng, 1994;10(2):1-34.

45 Maalej M. Fracture resistance of engineered fiber cementitiouscomposites and implications to structural behavior.PhD thesis2004, University of Michigan, at Ann Arbor, Michigan, USA.

46 Kim, D-J., Naaman, A.E. and El-Tawil, S. (2010), Correlation between Tensile and Bending Behavior of FRC Composites with Scale Effect,Proceedings of FraMCoS-7, 7th International Conference on Fracture Mechanics of Concrete and Concrete Structures, May 23-28, 2010, Jeju Island, South Korea

47 ASTM C1550 - 10a "Standard Test Method for Flexural Toughness of Fiber Reinforced Concrete (Using Centrally Loaded Round Panel)", ASTM Standard Book, V. 04.02, 2010.

48 American Concrete Institute, 'State-of–the-Art Report on Fiber Reinforced Concrete', ACI 544.1R-82, (1982).

49 Destrée, X.., 'Concrete free suspended elevated slabs reinforced with only steel Fibers: Full scale testing results and conclusions – design examples', RILEM Proceedings PRO49 (2006) 287-294.

50 Soranakom, C., Mobasher, B. and Destrée, X., 'Numerical simulation of FRC round panel tests and full-scale elevated slabs', ACI SP-248-3, (2007) 31-40.

51 Soranakom, C. and Mobasher, B., 'Closed-form solutions for flexural response of fiber-reinforced concrete beams', J. Eng. Mech., 133(8) (2007) 933-941.

52 ACI Committee 318, 'Building Code Requirements for Structural Concrete, ACI Manual of Concrete Practice', (American Concrete Institute, Detroit, 2005)

53 Vandewalle, L. et al., 'Test and design methods for steel fiber reinforced concrete – σ - ε design method – final recommendation', Mater. Struc., 36(262) (2003) 560 – 567.

54 Soranakom, C. and Mobasher, B., ‘Closed-form moment-curvature expressions for homogenized fiber reinforced concrete’, ACI Mater J., 104(4) (2007) 351-359.

55 Chuang T.-J. and Mai, Y.-W., ‘Flexural behavior of strain-softening solids’, Int. J. Solid Struct., 25(12) (1989) 1427-1443.

56 Wee, T.H. and Lu, H.R., and Swaddiwudhipong S., ‘Tensile strain capacity of concrete under various states of stress’, Mag. Concr. Res., 52(3) (2000) 185-193.

57 Arizona State University Faculty Website, http://enpub.fulton.asu.edu/cement/

APPENDIX A

A SPREADSHEET-BASED INVERSE ANALYSIS PROCEDURE FOR FLEXURAL SPECIMENS

-STRAIN SOFTENING OR HARDENING SAMPLES-

A.1.1 Application of Tri-Linear Model as an Excel Tool

The uniqueness of the spreadsheet format is that adjustments to the curve fitting parameters are updated in real time, reducing analysis time and allowing a more accurate simulation. Using the model outlined above, the parameters can be manipulated in a spreadsheet environment to model and best fit an experimental load deflection response. Units are not necessary as long as they are consistent. For English units ensure that all inputs are in inches, pounds force and psi. For SI units ensure all inputs are in millimeters, Newtons and MPa. This rule of consistent units applies to every entry (including the sample dimensions) in the spreadsheet. The sample values that are given in the examples are only related to this specific sample set, values for input parameters and material properties will vary with respect to the shape of the experimental load deflection curve.

A2.1 Four Point Bending – Strain Hardening

The four point bending test ASTM-1609 is carried out on standard beam dimensions with load applied at third points along the span. The load deflection curve will show an increase in load capacity after the linear elastic portion has ended. The hardening continues to increase as shown in Figure 3 or it can plateau as the sample continues to carry load.

Step 1:

Paste reduced load deflection data (up to 1000 data points) into the columns labeled “Load” and “Deflection”. This will populate the experimental load deflection curve we are trying to model as shown in Figure A2.1.1.

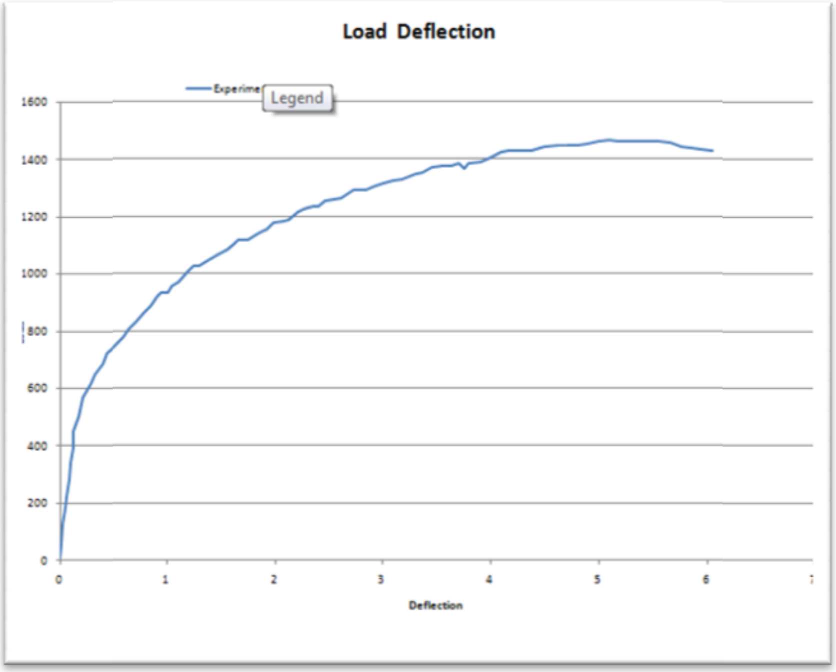

Figure A2.1.1 – Experimental load deflection response, showing deflection hardening characteristics.

Step 2:

Input the sample dimensions and test method. Table A.2.1.1 shows an example.

Table A.2.1.1 – Dimensions and test method definitions.

Input	Definition	Value
Test Method	Type of test	4
b	Width of sample	50
d	Depth of sample	25
L	Length of span	300

Table A2.1.2 Beam size and test method inputs

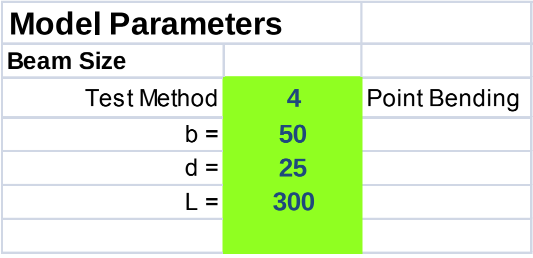

Model Parameters		
Beam Size		
Test Method	**4**	Point Bending
b =	**50**	
d =	**25**	
L =	**300**	

Step 3:

Determine the best fit for the Young's modulus for the linear elastic phase. This done by increasing or decreasing the value of the Elastic modulus (Young's modulus) *E*. Fiber reinforced cement (FRC) has a Young's modulus in the range of 3000000-5000000 psi (20000-35000 MPa)as shown in Figure 2.1.2

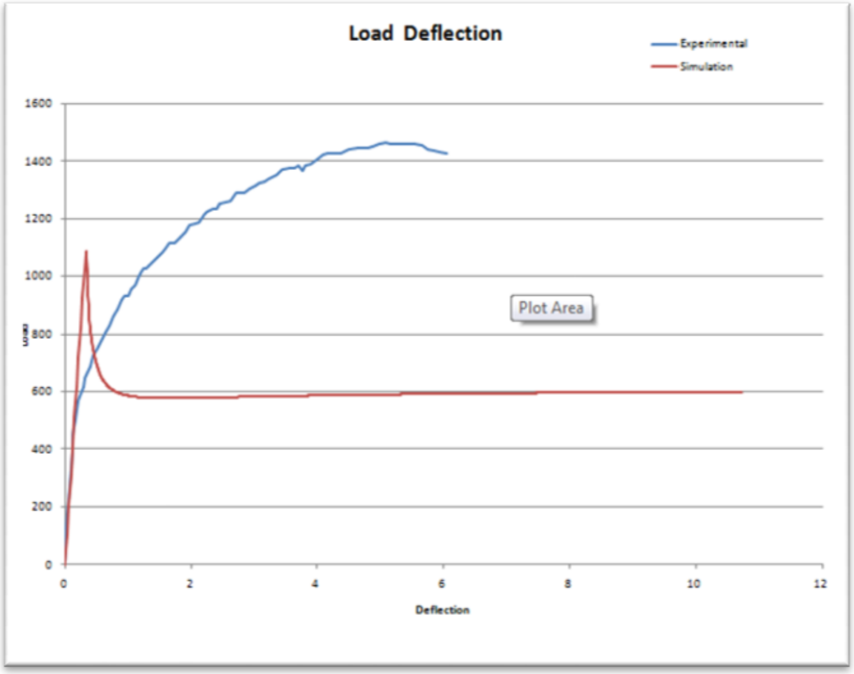

Figure A.2.1.2 – Linear section of load deflection clearly modeled by E=25000 MPa.

Step 4:

Now ε_{cr} will need to be fitted to the approximate point where the linear elastic behavior ceases and non-linear behavior begins. This parameter will depend on the type of FRC being tested; cement performance, fiber type and fiber dosage all contribute to the point where cracking is observed. In this case a value of 0.00013 was used. Figure A2.1.3 shows how the simulated curve has changed in response to the change in ε_{cr}.

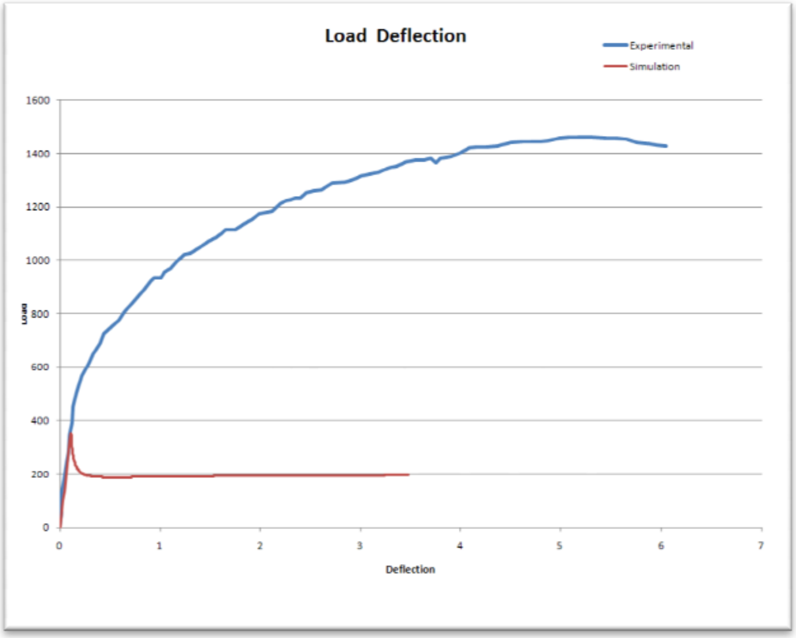

Figure A.2.1.3– Fitting of ε_{cr} *to load deflection curve*

Step 5:

The post cracking slope for strain hardening is represented by E_{cr} is related through the parameter η. This parameter is dependent on the values of α and μ. By manipulating α and μ the post cracking slope can be fitted to the load deflection curve. The parameter α adjusts the horizontal location of the transition point, while μ adjusts the vertical position of the transition point and the vertical position of the tail of the curve. Increasing μ will raise the post crack residual portion of the simulated curve. In this case the values of α and μ are given in Figure A.2.1.4. Figure A.2.1.5 shows the change in the simulated curve with respect to the parameter changes. The parameter η is automatically calculated and should reflect the post crack slope E_{cr} as negative in the softening case and positive in the hardening case (see Figure A.2.1.4).

The relationship between the parameters α and μ has other effects on the shape of the simulated curve. It should be noted that changes made in ε_{cr} will also require changes to the parameters α and μ to realign the simulation curve. The value of L_p automatically populates based on units, crack localization rules and the type of test method chosen.

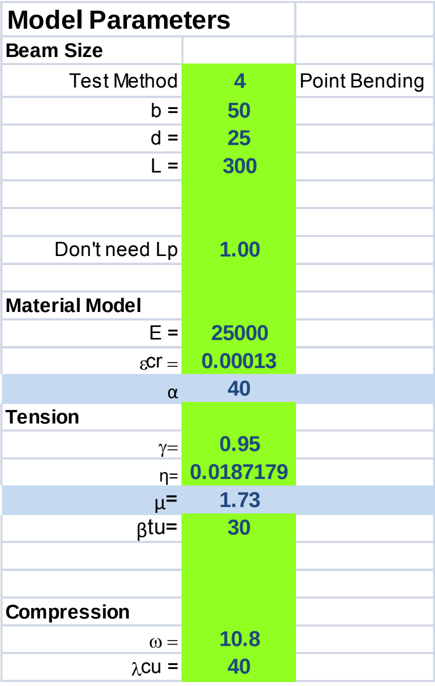

Model Parameters		
Beam Size		
Test Method	4	Point Bending
b =	50	
d =	25	
L =	300	
Don't need Lp	1.00	
Material Model		
E =	25000	
εcr =	0.00013	
α	40	
Tension		
γ=	0.95	
η=	0.0187179	
μ=	1.73	
βtu=	30	
Compression		
ω =	10.8	
λcu =	40	

Figure A.2.1.4 – Parameters α and μ are highlighted

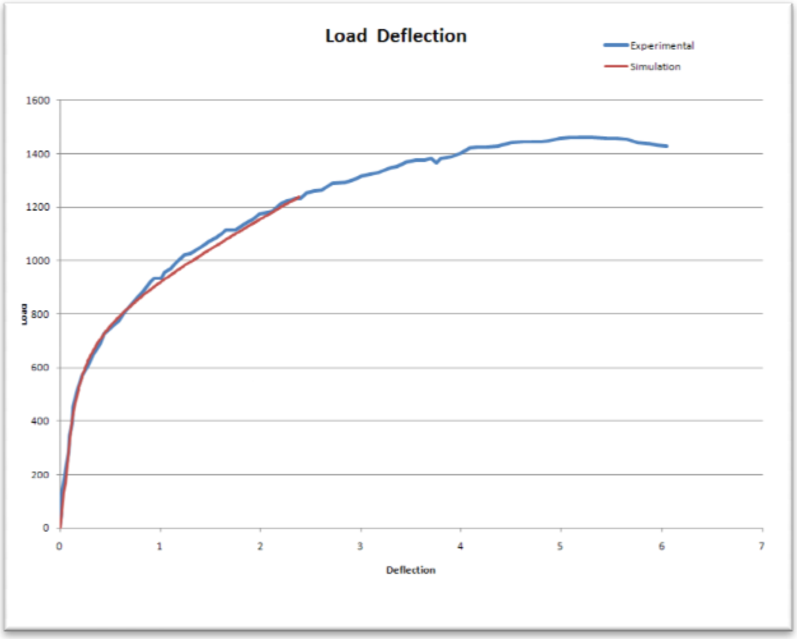

Figure A.2.1.5 – Change in simulated curve with respect to α and μ.

Step 6:

Now that most of the curve has been fitted we need to determine the ending point to the simulated curve, β_{tu} is used as the normalized ending point parameter.

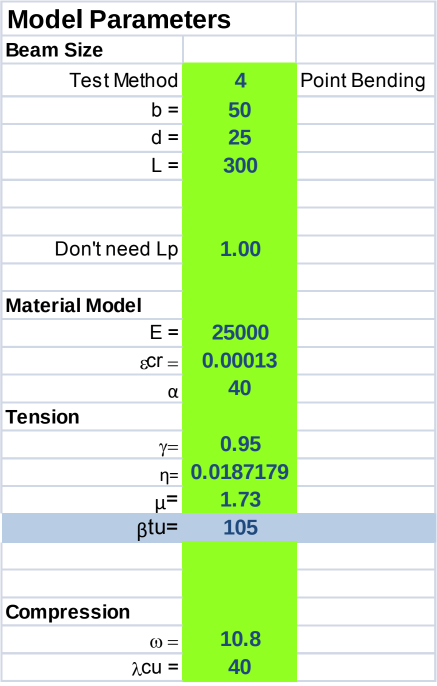

Model Parameters		
Beam Size		
Test Method	4	Point Bending
b =	50	
d =	25	
L =	300	
Don't need Lp	1.00	
Material Model		
E =	25000	
εcr =	0.00013	
α	40	
Tension		
γ=	0.95	
η=	0.0187179	
μ=	1.73	
βtu=	105	
Compression		
ω =	10.8	
λcu =	40	

Figure A.2.1.6 – Parameter inputs with β_{tu} updated to reflect end point.

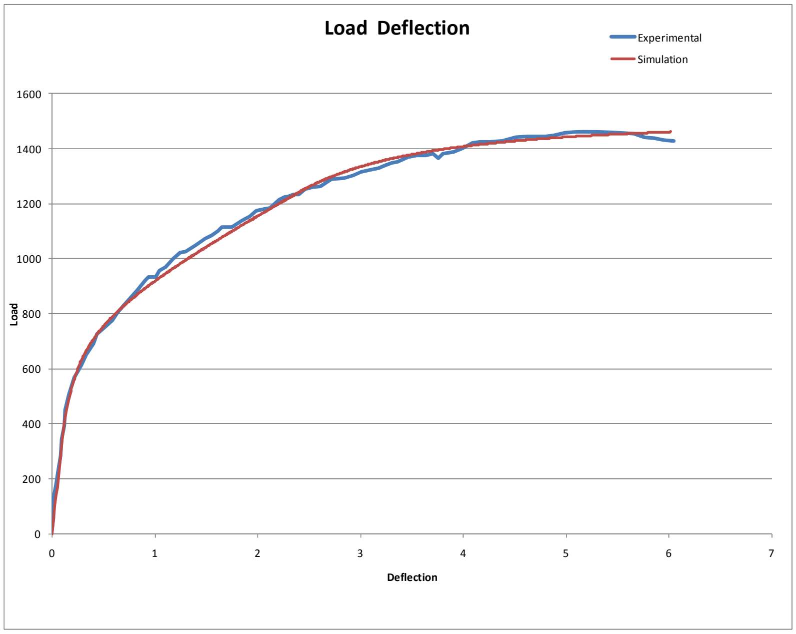

Figure A.2.1.7- Load deflection curve response to change in β_{tu}.

The parameter β_{tu} is dependent on the user's preference on when the ending point of the simulation curve needs to be. In some cases the entire deflection curve is not necessary, through this parameter adjustments can be made.

Step 7:

The determination of softening or hardening deflection behavior is determined by the parameter μ_{crit} which is the normalized post peak tensile strength; see equation (A.2.1). The parameter ω determines the cross over point from deflection softening to hardening. In this case;

$$\mu_{crit} = \frac{(10.8)}{(3(10.8)-1)} = 0.344 \qquad \text{(A.2.1)}$$

Since μ=1.73>μ_{crit} we see deflection hardening behavior in the simulated curve. Again, we see the interaction of the normalized parameters. By adjusting the value of ω (normalized compressive yield strain), we adjust the value of μ_{crit} which effects which deflection equation is used.

A2.2 Other Generated Data

There is a lot of data being modeled in this spreadsheet, with the simulated load deflection curve being the product of other useful processes. The spreadsheet generates a simulated tensile and compressive stress strain response under the *stress strain* worksheet; see Figure A.2.2.1 and A.2.2.2. The spreadsheet also generates the simulated moment curvature response and the stand alone simulated load deflection response under the *moment curvature* worksheet; see Figure (A.2.2.3) and (A.2.2.4).

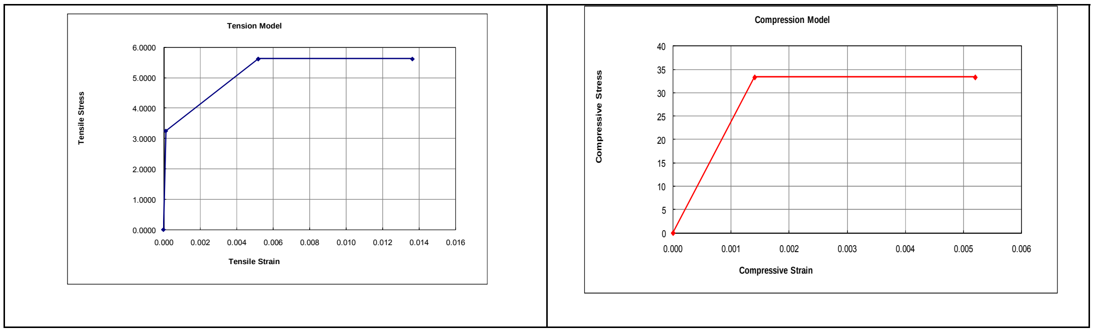

Figure A.2.2.1 – Simulated tensile and compressive stress strain response for deflection hardening case.

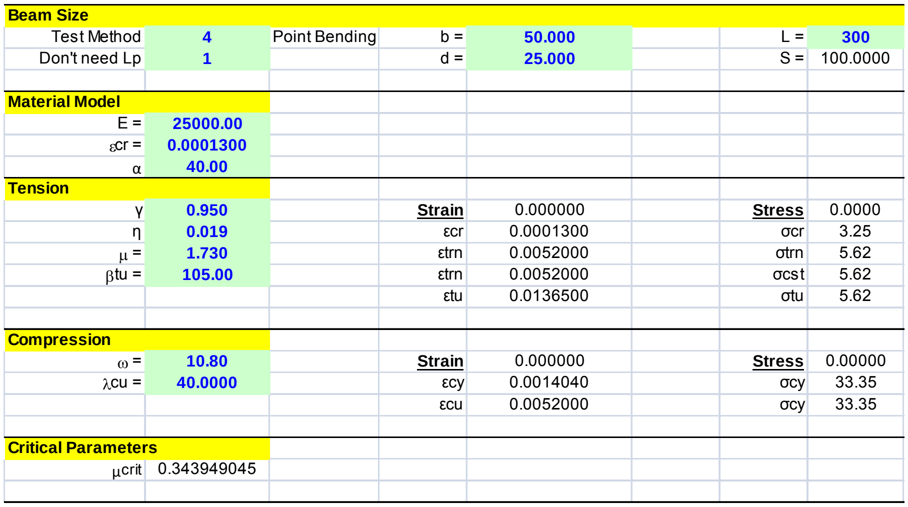

Beam Size							
Test Method	**4**	Point Bending	b =	**50.000**		L =	**300**
Don't need Lp	**1**		d =	**25.000**		S =	100.0000
Material Model							
E =	**25000.00**						
εcr =	**0.0001300**						
α	**40.00**						
Tension							
γ	**0.950**		**Strain**	0.000000		**Stress**	0.0000
η	**0.019**		εcr	0.0001300		σcr	3.25
μ =	**1.730**		εtrn	0.0052000		σtrn	5.62
βtu =	**105.00**		εtrn	0.0052000		σcst	5.62
			εtu	0.0136500		σtu	5.62
Compression							
ω =	**10.80**		**Strain**	0.000000		**Stress**	0.00000
λcu =	**40.0000**		εcy	0.0014040		σcy	33.35
			εcu	0.0052000		σcy	33.35
Critical Parameters							
μcrit	0.343949045						

Figure A.2.2.2 – Stress strain screenshot of computed parameter values for hardening case.

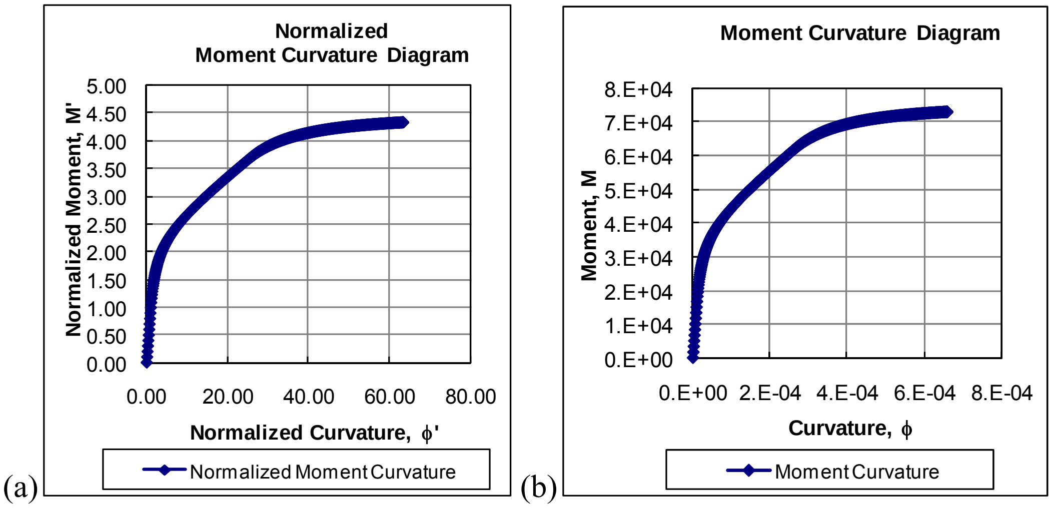

Figure A.2.2.3 – Strain hardening (a) normalized moment curvature and (b) moment curvature.

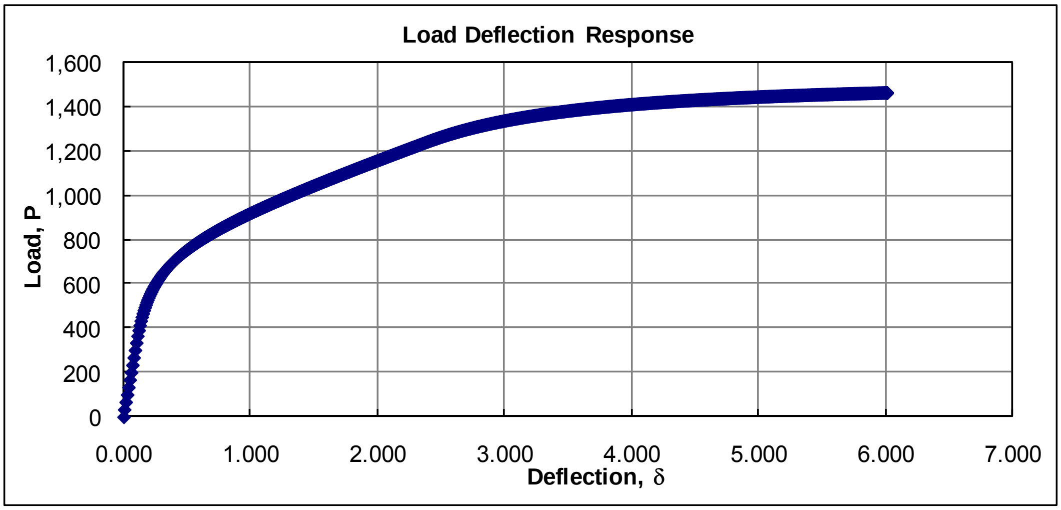

Figure A.2.2.4 – Simulated load deflection response

A.3.1 Four Point Bending – Strain Softening

The four point bending test ASTM-1609 is carried out on standard beam dimensions with load applied at third points along the span. The load deflection curve will show a decrease in load capacity after the linear elastic portion has ended. The softening continues as shown in Figure A.3.1.1 or it can plateau as the sample continues to sustain load as deflection continues.

STEP 1:

Paste reduced load deflection data (up to 1000 points) into the columns labeled "Load" and "Deflection". This will populate the experimental load deflection curve we are trying to model as shown in Figure A.3.1.1.

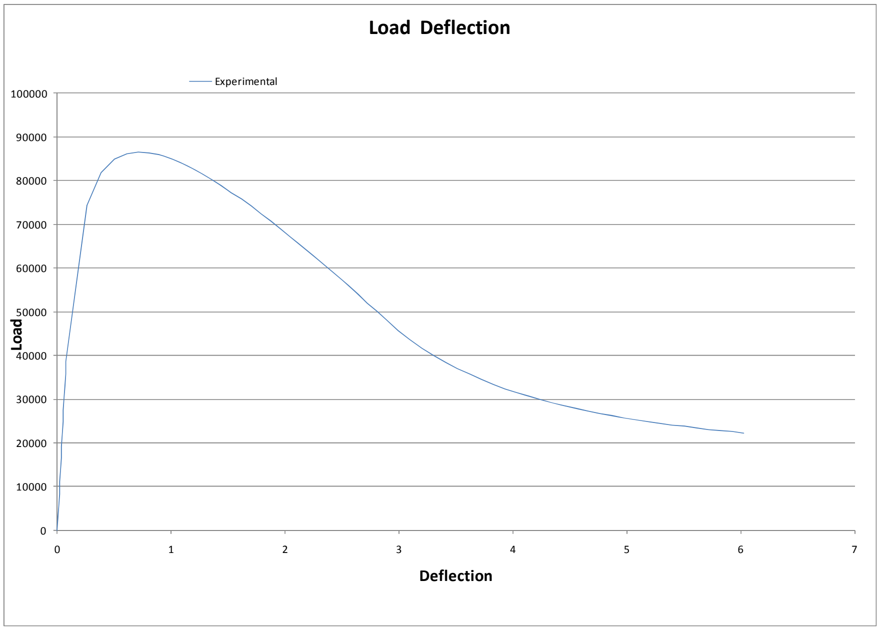

Figure A.3.1.1 - Experimental load deflection response, showing deflection softening characteristics.

Step 2:

Input the sample dimensions and test method. Table A.3.1.1 shows an example.

Table A.3.1.1 – Dimensions and test method definitions.

Input	Definition	Value
Test Method	Type of Test	4
b	Width of sample	150
d	Depth of sample	150
L	Length of span	450

Figure A.3.1.2 – Beam size and test method inputs.

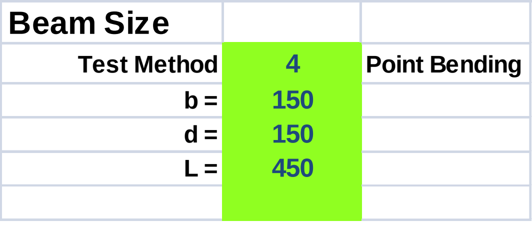

Beam Size		
Test Method	**4**	**Point Bending**
b =	**150**	
d =	**150**	
L =	**450**	

Step 3:

Determine the best fit for the Young's modulus for the linear elastic phase. This done by increasing or decreasing the value of the Elastic modulus (Young's modulus) *E*. Fiber reinforced cement (FRC) has a Young's modulus in the range of 3000000-5000000 psi (20000-35000 MPa).

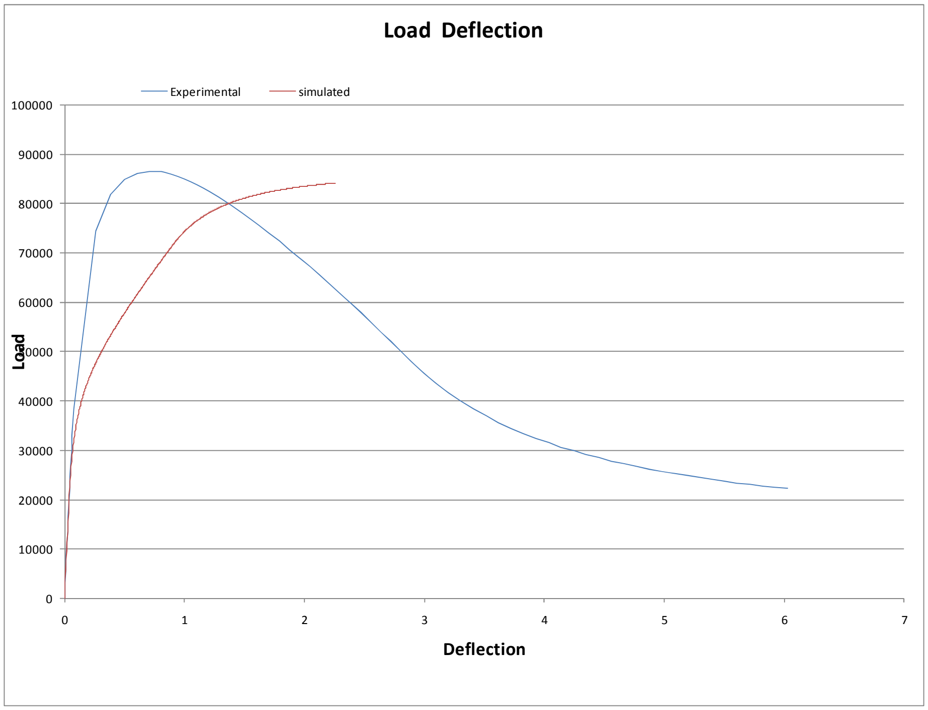

Figure A.3.1.2 – Linear section of load deflection clearly modeled by E=20000 MPa.

Step 4:

Now ε_{cr} will need to be fitted to the approximate point where the linear elastic behavior ceases and non-linear behavior begins. This parameter will depend on the type of FRC being tested; cement performance, fiber type and fiber dosage all contribute to the point where cracking is observed. In this case a value of 0.00013 was used. Figure A.3.1.3 shows how the simulated curve has changed in response to the change in ε_{cr}.

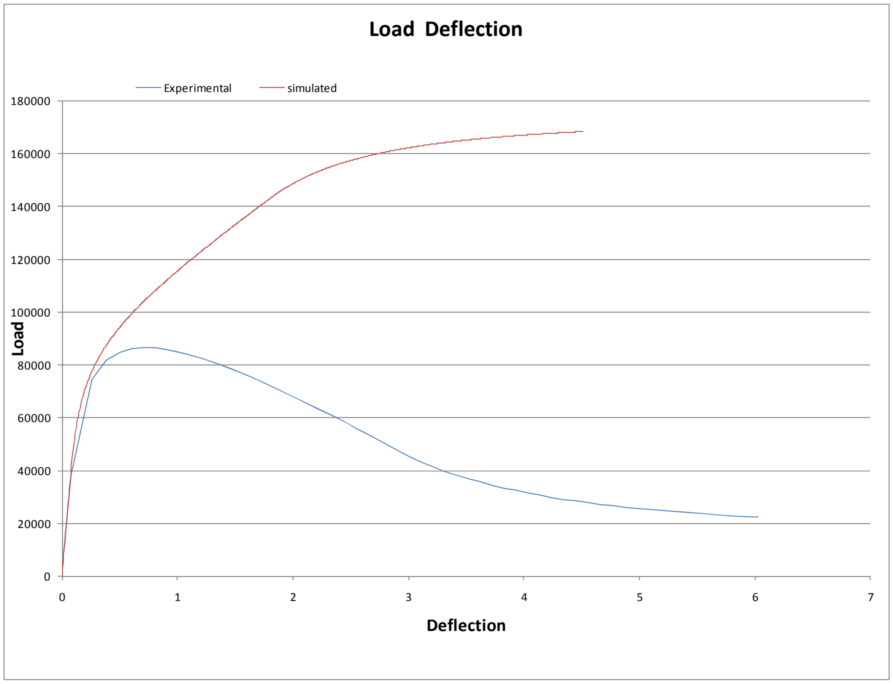

Figure A.3.1.3– Fitting of ε_{cr} to load deflection curve.

Step 5:

The post cracking slope for strain hardening is represented by E_{cr} is related through the parameter η. This parameter is dependent on the values of α and μ. By manipulating α and μ the post cracking slope can be fitted to the load deflection curve. The parameter α adjusts the horizontal location of the transition point, while μ adjusts the vertical position of the transition point and the vertical position of the tail of the curve. Increasing μ will raise the post crack residual portion of the simulated curve. In this case the values of α and μ are given in Figure A.3.1.4. Figure 19 shows the change in the simulated curve with respect to the parameter changes. The parameter η is automatically calculated and should reflect the post crack slope E_{cr} of a negative value in the softening case (see Figure A.3.1.4).

The relationship between the parameters α and μ has other effects on the shape of the simulated curve. It should be noted that changes made in ε_{cr} will also require changes to the parameters α and μ to realign the simulation curve. The value of L_p automatically populates based on units, crack localization rules and the type of test method chosen.

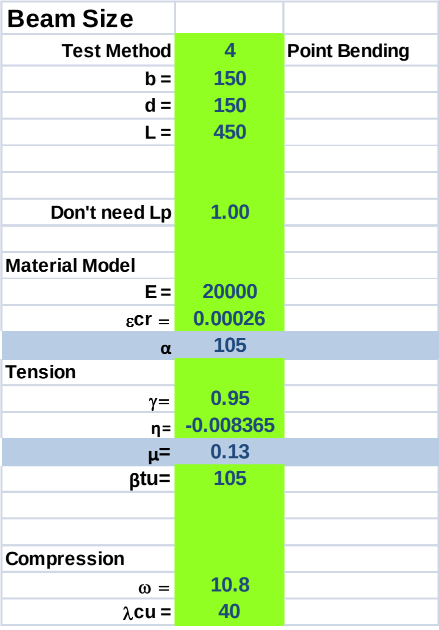

Beam Size		
Test Method	4	Point Bending
b =	150	
d =	150	
L =	450	
Don't need Lp	1.00	
Material Model		
E =	20000	
εcr =	0.00026	
α	105	
Tension		
γ=	0.95	
η=	-0.008365	
μ=	0.13	
βtu=	105	
Compression		
ω =	10.8	
λcu =	40	

Figure A.3.1.4 – Parameters α and μ are highlighted

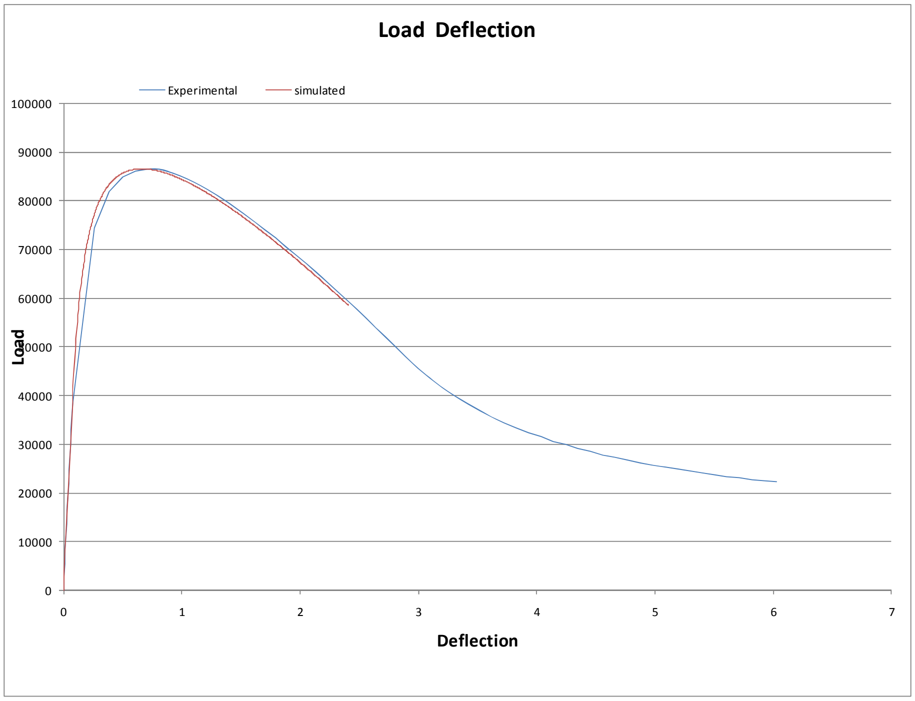

Figure A.3.1.5 – Change in simulated curve with respect to α and μ.

Step 6:

Now that most of the curve has been fitted we need to determine the ending point to the simulated curve, β_{tu} is used as the normalized ending point parameter.

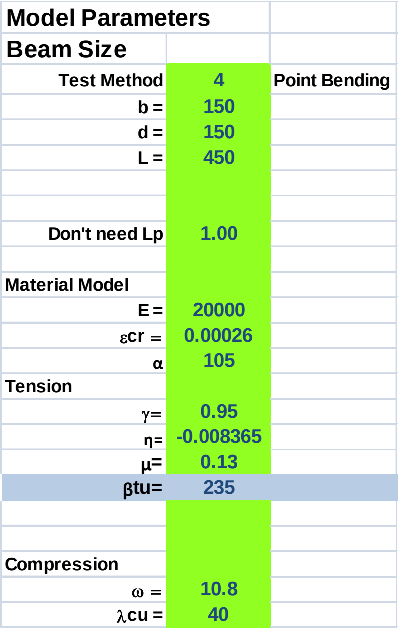

Model Parameters		
Beam Size		
Test Method	4	**Point Bending**
b =	150	
d =	150	
L =	450	
Don't need Lp	1.00	
Material Model		
E =	20000	
εcr =	0.00026	
α	105	
Tension		
γ=	0.95	
η=	-0.008365	
μ=	0.13	
βtu=	235	
Compression		
ω =	10.8	
λcu =	40	

Figure A.3.1.6 – Parameter inputs with β_{tu} updated to reflect end point.

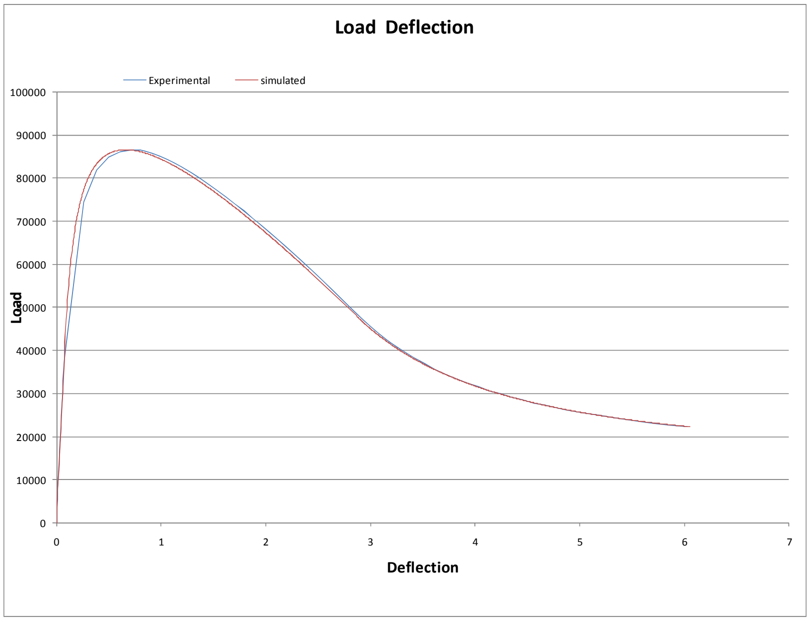

Figure A.3.1.7 – Load deflection curve response to change in β_{tu}.

The parameter β_{tu} is dependent on the user's preference on when the ending point of the simulation curve needs to be. In some cases the entire deflection curve is not necessary, through this parameter adjustments can be made.

Step 7:

The determination of softening or hardening deflection behavior is determined by the parameter μ_{crit} which is the normalized post peak tensile strength; see equation (3.1). The parameter ω determines the cross over point from deflection softening to hardening. In this case;

$$\mu_{crit} = \frac{(10.8)}{(3(10.8)-1)} = 0.344 \tag{3.1}$$

Since μ=0.13<μ_{crit} we see deflection softening behavior in the simulated curve. Again, we see the interaction of the normalized parameters. By adjusting the value of ω (normalized compressive yield strain), we adjust the value of μ_{crit} which effects which deflection equation is used

A.3.2 Other Generated Data

There is a lot of data being modeled in this spreadsheet, with the simulated load deflection curve being the product of other useful processes. The spreadsheet generates a simulated tensile and compressive stress strain response under the *stress strain* worksheet; see Figure (A.3.2.1) and (A.3.2.2). The spreadsheet also generates the simulated moment curvature response and the stand alone simulated load deflection response under the *moment curvature* worksheet; see Figure (A.3.2.3) and (A.3.2.4).

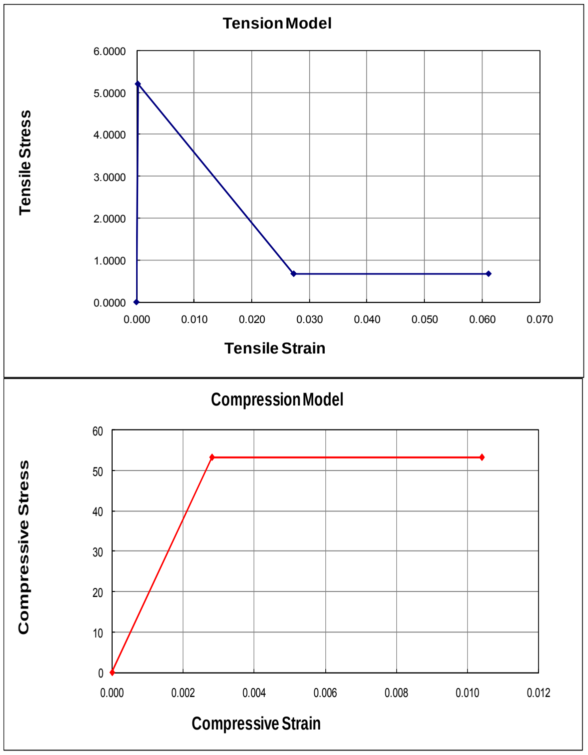

Figure A.3.2.1 – Simulated tensile and compressive stress strain response for deflection softening case.

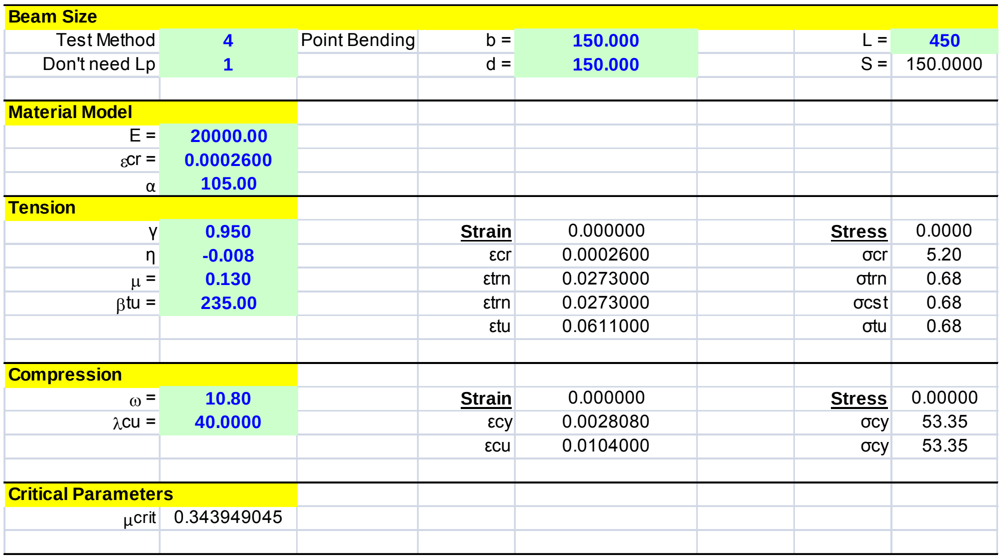

Beam Size							
Test Method	**4**	Point Bending	b =	**150.000**		L =	**450**
Don't need Lp	**1**		d =	**150.000**		S =	150.0000
Material Model							
E =	**20000.00**						
εcr =	**0.0002600**						
α	**105.00**						
Tension							
γ	**0.950**		**Strain**	0.000000		**Stress**	0.0000
η	**-0.008**		εcr	0.0002600		σcr	5.20
μ =	**0.130**		εtrn	0.0273000		σtrn	0.68
βtu =	**235.00**		εtrn	0.0273000		σcst	0.68
			εtu	0.0611000		σtu	0.68
Compression							
ω =	**10.80**		**Strain**	0.000000		**Stress**	0.00000
λcu =	**40.0000**		εcy	0.0028080		σcy	53.35
			εcu	0.0104000		σcy	53.35
Critical Parameters							
μcrit	0.343949045						

Figure A.3.2.2 – Stress strain screenshot of computed parameter values for softening case.

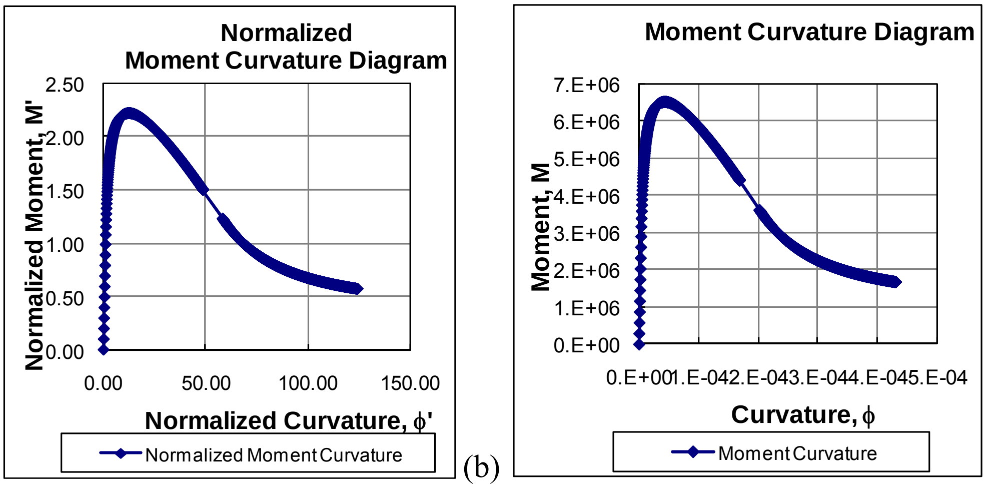

(a) (b)

Figure A.3.2.3– Strain softening (a) normalized moment curvature and (b) moment curvature.

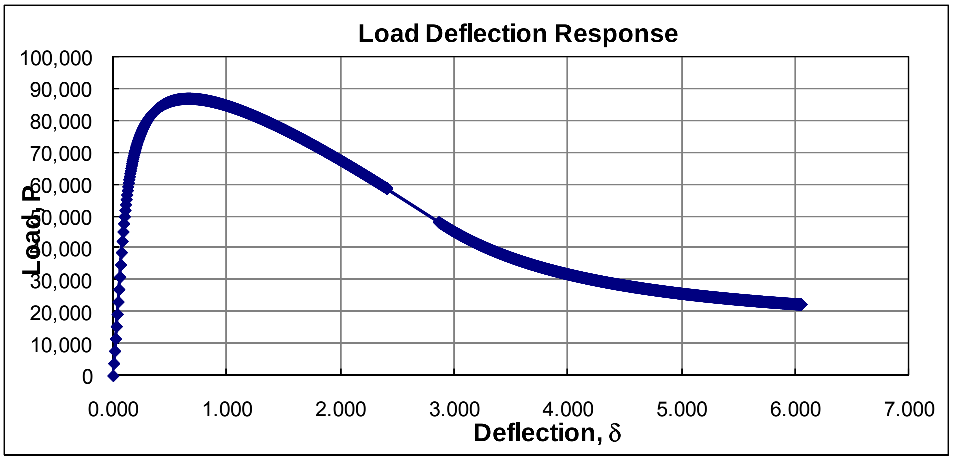

Figure A.3.2.4 – Simulated load deflection response